

# Preface

This thesis is submitted to The Faculty of Science, University of Aarhus, Denmark, in order to meet the requirements for obtaining the Ph.D. degree in physics. It covers the work I have carried out in the scanning tunneling microscopy laboratory at the Institute of Physics and Astronomy from spring 1993 until summer 1996. Throughout the period, a number of people have, directly or indirectly, been involved in my project, and their support with e.g. fund raising, equipment, and physics, is gratefully acknowledged. Without these people the project would have been impossible, and in this way the present thesis is a product of a great collaborative effort.

Among the people I am especially indebted to are my three supervisors, who have unified their individual expertise in a remarkable teamwork. My first introduction to the laboratory was given by Flemming Besenbacher and ever since has he followed, guided, and supported me during my project. His enthusiasm and tireless commitment has often been an inspiration to carry on. When it comes to the practical realization of the experiments, Erik Lægsgaard has been an invaluable person. He builds, maintains, and continuously develops not only the microscopes but also the controlling software. Modifications to the software have often been accomplished in accordance with my needs in a matter of hours. During the years, I have repeatedly been impressed by Erik's ability to solve difficult tasks in an easy way, and I am pleased, that I have had the chance to learn from him. Likewise, it has been a pleasure to gain from the experience of Ivan Stensgaard. He has always been able to give firm and well-considered answers to my questions, and his calm nature has often provided a nice contrast to otherwise hectic surroundings in the laboratory.

Since I started out doing experiments focused on the junction in the scanning tunneling microscope, the project has been characterized by a strong interplay between experiment and theory. This has been achieved

through a collaboration with the theoretical group at Technical University of Denmark headed by Jens K. Nørskov. I especially want to mention Mads Brandbyge, Mads R. Sørensen, and Jacob Schiøtz, who have performed the main part of the theoretical work connected to this project. However, I have also enjoyed many fruitful discussions with the seniors Karsten W. Jacobsen, Jens K. Nørskov, and Per Stoltze.

Even though it is extremely interesting and challenging to do scientific experiments, it is also often a matter of patience, determination, and hard work. While fighting these drawbacks, I have found that the importance of coffee breaks, informal conversations, and other non-professional incidents cannot be overestimated. Therefore, it has been a pleasure to be a member of a large experimental group including people with different backgrounds, nationalities, and opinions, and I would like to thank my colleagues in the group during the last five years as well as long-term guests: Flemming Jensen, Casper Klink, Lars Eierdal, Like Ruan, Adam R. H. Clarke, Allan Christensen, Morten Foss, Yuji Okawa, Svein Thors-haug, Philip Sprunger, Lars P. Nielsen, Paul Murray, Karina Morgenstern, Naoki Takehiro, Trolle Linderøth, Sebastian Horch, Ylva Bönicke, Morten Ø. Pedersen, Kim Hansen, Lars Petersen, and Stig Christensen. Also, I appreciate the practical support from Lone Niedziella and Randi Mosegaard along with linguistic help from Alice Grandjean in connection with the present thesis.

Finally, I acknowledge financial support from *CAMP*, the Center for Atomic-scale Materials Physics sponsored by the Danish National Research Foundation, and from the Danish Research Councils through the Center for Nano-Tribology.

Aarhus, August 1996  
Lars Olesen

In the present second edition I have corrected a number of misspelling and grammatical errors along with some typographical mistakes. Apart from a confusing nomenclature with both  $V_t$  and  $I_t$  on one hand and  $V_b$  and  $I$  on the other ( $V_b$  and  $I$  have survived) the typographical mistakes also include several occurrences of a wrong temperature (370 K is wrong, 390 K is right) and an interchange of two sections in the outline of chapter 6. Hopefully, there will be no third edition.

Aarhus, October 1996  
Lars Olesen

# Contents

<b>1</b>	<b>Introduction</b>	<b>9</b>
1.1	Background . . . . .	9
1.2	The Invention . . . . .	10
1.3	Performance of STM . . . . .	12
1.4	Outline . . . . .	15
1.5	Practical Remarks . . . . .	16
<b>2</b>	<b>Theory of Tunneling</b>	<b>19</b>
2.1	Introduction . . . . .	19
2.2	Matching Wave Functions . . . . .	19
2.3	Transmission through a Parabolic Barrier . . . . .	22
2.4	Barriers with Arbitrary Shapes . . . . .	23
2.5	The Perturbative Bardeen Approach . . . . .	24
2.6	STM Theory by Tersoff and Hamann . . . . .	26
	Image Potential and Barrier Height . . . . .	29
<b>3</b>	<b>Experimental Details</b>	<b>33</b>
3.1	Introduction . . . . .	33
3.2	The STM . . . . .	33
	The Scanner Tube . . . . .	34
	The Inchworm . . . . .	35
3.3	The Heating and Cooling Stage . . . . .	35
3.4	Electronics . . . . .	38
3.5	Methods of Measuring . . . . .	40
	Bias and Displacement: $z(V_b)$ . . . . .	40
	Current and Displacement: $z(I)$ . . . . .	40
	ABH Images . . . . .	41
	Error-Signal Images . . . . .	41

	Indentations . . . . .	41
3.6	The Surfaces . . . . .	43
3.7	The Tip: Stability and Wetting . . . . .	44
<b>4</b>	<b>Apparent Barrier Height</b>	<b>47</b>
4.1	Introduction . . . . .	47
4.2	Review . . . . .	48
4.3	Experimental Results . . . . .	52
4.4	Discussion . . . . .	56
4.5	Atom-Resolved Apparent Barrier Height . . . . .	62
4.6	Discussion of Atom-Resolved ABH . . . . .	67
4.7	Summary . . . . .	68
<b>5</b>	<b>Contact Formation</b>	<b>71</b>
5.1	Introduction . . . . .	71
5.2	Review . . . . .	72
5.3	Experimental Results . . . . .	77
5.4	Discussion . . . . .	84
5.5	Polarity Dependent Contact Formation . . . . .	86
5.6	Discussion of Polarity Effects . . . . .	92
5.7	Summary . . . . .	95
<b>6</b>	<b>Quantized Conductance</b>	<b>99</b>
6.1	Introduction . . . . .	99
6.2	Theoretical Background . . . . .	100
6.3	Review . . . . .	106
6.4	Experimental Results . . . . .	110
6.5	Discussion of the Ideal Case — Gold . . . . .	118
	Scattering . . . . .	123
	Simulation Results . . . . .	125
	Conclusion . . . . .	127
6.6	Further Discussion . . . . .	129
6.7	Summary . . . . .	132
<b>7</b>	<b>Summary</b>	<b>137</b>
<b>8</b>	<b>Dansk resumé</b>	<b>141</b>

<b>A Electronic Details</b>	<b>145</b>
A.1 Preamplifiers . . . . .	145
A.2 Current and Input Impedance . . . . .	147
A.3 Precision of Conductance Measurement . . . . .	147
A.4 Piezo Voltage Delay . . . . .	148
A.5 Time Calibration . . . . .	148
<b>B Data Analysis</b>	<b>153</b>
B.1 Thermo-voltages and Tip Resistances . . . . .	153
B.2 Conductance Calibration . . . . .	154
B.3 Continuous Histograms . . . . .	155



# List of Publications

## Publications Related to Thesis

- [I] Quantized Conductance in an Atom-Sized Point Contact,  
L. Olesen, E. Lægsgaard, I. Stensgaard, F. Besenbacher,  
J. Schiøtz, P. Stoltze, K. W. Jacobsen, and J. K. Nørskov,  
Physical Review Letters **72**, 2251 (1994).
- [II] Reply to Comment on  
“Quantized Conductance in an Atom-Sized Point Contact”  
L. Olesen, E. Lægsgaard, I. Stensgaard, F. Besenbacher,  
J. Schiøtz, P. Stoltze, K. W. Jacobsen, and J. K. Nørskov,  
Physical Review Letters **74**, 2147 (1995).
- [III] Quantized conductance in atom-sized wires between two metals,  
M. Brandbyge, J. Schiøtz, M. R. Sørensen,  
P. Stoltze, K. W. Jacobsen, J. K. Nørskov,  
L. Olesen, E. Lægsgaard, I. Stensgaard, and F. Besenbacher,  
Physical Review B **52**, 8499 (1995).
- [IV] Apparent Barrier Height in  
Scanning Tunneling Microscopy Revisited,  
L. Olesen, M. Brandbyge, M. R. Sørensen,  
K. W. Jacobsen, E. Lægsgaard, I. Stensgaard, and F. Besenbacher,  
Physical Review Letters **76**, 1485 (1996).
- [V] Experimental Studies of Tip-Surface Interactions,  
L. Olesen, K. Hansen,  
E. Lægsgaard, I. Stensgaard, and F. Besenbacher,  
To appear in Proceedings of the  
NATO Advanced Research Workshop on Nanowires, Madrid, 1996.

- [VI] Atom-Resolved Studies of the Apparent Barrier Height,  
L. Olesen, E. Lægsgaard, I. Stensgaard, and F. Besenbacher,  
In preparation.
- [VII] Novel Amplifier System for Conductance Measurements in STM,  
E. Lægsgaard, L. Olesen, I. Stensgaard, and F. Besenbacher,  
In preparation.

## Other Publications

- [VIII] Interaction of C with Ni(100):  
Atom-Resolved Studies of the “Clock” Reconstruction,  
C. Klink, L. Olesen, F. Besenbacher,  
I. Stensgaard, E. Lægsgaard, and N. D. Lang,  
*Physical Review Letters* **71**, 4350 (1993).
- [IX] Direct observations of changes in surface structures  
by scanning tunneling microscopy,  
F. Besenbacher, P. T. Sprunger, L. Ruan,  
L. Olesen, I. Stensgaard, and E. Lægsgaard,  
*Topics in Catalysis* **1**, 325 (1994).

# Chapter 1

## Introduction

### 1.1 Background

Classical physics puts strict rules as to where a particle can go. It is not allowed to penetrate or cross any part of space that requires a potential energy higher than the total energy of the particle (a football will never roll uphill by itself). The same rules do not apply to quantum mechanics, where matter is described by wave functions in accordance with the wave-particle duality [1]. In principle, a wave function extends over all space, and its value at a certain point in space gives the probability of detecting the particle at that specific spot. As a consequence of this, a quantum-mechanical particle may show up in a part of space that never could be reached by a classical particle (the football will never suddenly disappear from one side of the hill and pop up on the other side<sup>1</sup>). This phenomenon, which has no classical analogy, is called tunneling.

From a theoretical point of view, tunneling is a standard textbook problem that often, however in a highly idealized version, is used to introduce undergraduate students to the astonishing world of quantum mechanics. Already in 1928, when quantum theory still was a newborn discipline, were the first theoretical works on vacuum tunneling published. Oppenheimer [3] calculated the probability of ionization of a hydrogen atom in a homogeneous electric field, and Fowler and Nordheim [4] successfully explained the field emission from cold metals discovered a couple of years

---

<sup>1</sup>A football behaves according to classical physics. This is, however, not inconsistent with quantum mechanics, since the two physical descriptions are equivalent in the limit of large quantum numbers (Bohr's correspondence principle [2]).

earlier by Lilienfeld [5]. In both cases, the electron tunnels through a vacuum barrier and ends up in the vacuum (Fowler-Nordheim regime). A related and, in principle, simple extension of these processes is metal-vacuum-metal tunneling, where electrons tunnel from one metal through a vacuum barrier and into another metal. Nevertheless, many years passed by before that goal was realized experimentally. Metal-to-metal tunneling was indeed demonstrated, but the barrier always consisted of an insulating solid material like, e.g., oxide sandwiched between the metals [6]. These experiments have several disadvantages that makes vacuum tunneling an appealing alternative. First of all, the properties of the barrier material have to be taken into account, which is a complication, and a continuous change of the barrier width is not possible. Moreover, there is no free access to the electrodes, and an investigation of different atoms or molecules in the tunneling region is thus not possible.

The first successful experiment on metal-vacuum-metal tunneling was reported as late as 1971 by Young and co-workers [7] who came extremely close to the invention of the scanning tunneling microscope (STM). In fact, the resemblance between STM and their “Topografiner” [8] is so remarkable that their instrument may have worked as an STM. However, since Young *et al.* only used the scanning mode of the Topografiner in the Fowler-Nordheim regime, the invention of the STM was postponed another decade.

## 1.2 The Invention

In the late seventies, Binnig and Rohrer started out a new scientific project. Their initial intention was to investigate local tunneling behavior on areas less than 100 Å in diameter of thin oxide layers grown on metal surfaces [9,10]. Soon they realized that the appropriate tool for such experiments was lacking, and consequently, a new instrument had to be constructed. Before this work actually began, Binnig was puzzled by the intriguing and challenging prospects of vacuum tunneling, and after a couple of weeks, it became clear to Binnig and Rohrer that the combination of local tunneling *and* scanning could provide spectroscopic and topographic images of a surface. This was the birth of a new kind of microscope, the STM. Early in 1983, when Binnig *et al.* presented the first atom-resolved images of the (7×7) reconstruction of Si(111) [11], people began to appreciate the great potential of STM in surface science. The amazing ability to make real-space images of semiconductor and metal surfaces on the atomic scale was

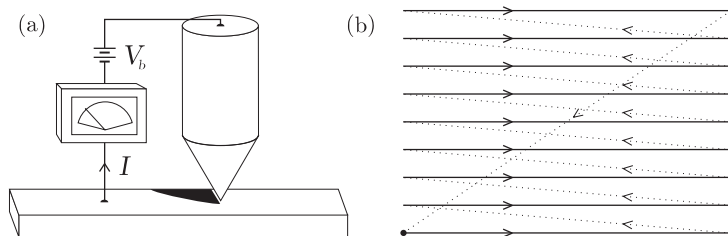


Figure 1.1: The tunnel current  $I$  is established by applying a bias voltage  $V_b$  when the tip is within a few atomic spacings of a conducting surface (a). Images are acquired by raster-scanning the tip laterally over the surface (b). Each line scan (solid lines) is followed by a tip flyback (dotted lines).

appealing to many people, and it induced an explosive growth in the field. Not only did many scientific groups take up STM as a surface science tool, a vast variety of related scanning probe microscopes (SPM) were also born. Among the most prominent SPM techniques can be mentioned atomic-force microscopy (AFM), friction-force microscopy (FFM), magnetic-force microscopy (MFM), and scanning near-field optical microscopy (SNOM). Today, the SPM techniques are invaluable tools in surface science, and the significance of the STM invention is also demonstrated by the fact that in 1986, Binnig and Rohrer were awarded the Nobel Prize in physics for their work.

The concept of a scanning tunneling microscope is surprisingly simple. By placing a sharp metal tip very close to a conducting surface (only a few atomic-lattice spacings away) the probability that an electron will tunnel from tip to surface, or *vice versa*, becomes appreciable. Furthermore, if a small bias voltage is applied (mV range), the electrons will preferentially tunnel towards the positively biased electrode due to the negative charge of the electron. In this way, a current (pA–nA range) can be driven through the circuit even though tip and surface do not touch each other<sup>2</sup> [see Fig. 1.1(a)]. Since an electronic wave function decays exponentially into the vacuum, the tunneling probability, and thereby the current, also decreases exponentially as a function of tip-surface separation. This fortunate relationship between tunnel current and gap width is the main reason why STM is capable of achieving atomic resolution (more details will be given in chapter 2). Having established a tunnel current, images can be

<sup>2</sup>Explicitly, this means that there is no metallic or covalent bonding between tip atoms and surface atoms.



Figure 1.2: (a) Atomically resolved  $18 \times 16 \text{ \AA}^2$  constant-current image of a clean Ni(111) surface recorded with the tunneling parameters  $I = 5.2 \text{ nA}$ ,  $V_b = 8.2 \text{ mV}$ . The insert shows the height contour given in ångströms measured along the line indicated in the image. (b) Logo for the *Center for Atomic-scale Materials Physics* written on a clean Cu(100) surface by indenting the tip into the surface in a well defined pattern. The area shown corresponds to  $740 \times 310 \text{ \AA}^2$ .

acquired by recording the current<sup>3</sup>, while the tip is raster-scanned laterally over the surface (Fig. 1.1(b)).

### 1.3 Performance of STM

In Fig. 1.2 are shown two constant-current topographic images that in several ways illustrate the performance of STM. The relative height of the tip excursion normal to the surface during scanning is indicated by a color-scale (bright colors meaning high, dark colors meaning low). A bright-colored spot is thus associated with a protrusion sticking out from the surface. Figure 1.2(a) is a  $18 \times 16 \text{ \AA}^2$  image of a clean Ni(111) surface. The resolution showing the atomic periodicity is immediately apparent from this image. However, there is no information in the image that indicates which element we are actually looking at. For a clean surface like the one shown in Fig. 1.2(a), this poses no problem, since the crystal under investigation usually is well known. On the other hand, if more than one kind of element is present on the surface, as is often the case in surface science, it can be a severe drawback. At the best circumstances, the difference between two elements  $A$  and  $B$  on the surface can be revealed from a contrast in the image. By comparing with a knowledge of, e.g., the coverage of  $A$  relative to  $B$ , it will often be possible to determine whether

<sup>3</sup>This is the so-called constant-height mode. Another mode of operation is the constant-current mode, where the height of the tip above the surface is varied to keep the tunnel current constant. Consult chapter 3 for further details.

an image feature is related to one element or the other. The combination of STM and other surface-science techniques can therefore be very powerful. Nevertheless, a more direct way to distinguish  $A$  from  $B$  is requested, as most other surface-science techniques measure an average property of a surface area which is many orders of magnitude larger than the atomic scale. A direct comparison with atomically resolved STM is therefore not always possible.

On semiconductor surfaces, scanning tunneling spectroscopy (STS) has been used with success to discriminate between sites and constituents with a difference in the local density of states (LDOS) — although a detailed understanding of the observed effects often is lacking [12]. Similar reproducible structures in STS spectra on metals have only been found in a very few cases due to the free-electron nature of most metals [13,14]. Other ways of achieving chemical specificity by manipulating the apex of the tip [15,16] or by tunneling into distorted image states [17] have also been reported. However, at the present stage, no method has proven to be generally applicable.

Since the tip constitutes one of the two electrodes in STM, the measurements reflect properties of the tip as well as surface characteristics. The tip geometry and composition are therefore of utmost importance. An example of a tip-induced effect is also present in Fig. 1.2(a). By careful inspection, it is revealed that the atoms are imaged asymmetrically; they do not possess the expected sixfold symmetry of the surface<sup>4</sup>. Since the origin of this “artifact” cannot be the surface, it is bound to be caused by the movement and/or the geometry of the tip. While the lateral movement of the tip is easily controlled by the operator, it is far more difficult to characterize or design a tip on the atomic scale. Field-ion microscopy may be used as a way to correlate STM measurements with the atomic structure of the tip [19]. However, the fact that the tip often undergoes structural and/or electronic changes during normal image acquisition makes it very hard to use this method on a routine basis.

Another interesting aspect of Fig. 1.2(a) is the magnitude of the corrugation. From the cross-sectional line scan superimposed on the image, it is seen that the height difference between on-top and hollow sites is measured to be as large as 0.6 Å. From first-order tunneling theories, it is expected

---

<sup>4</sup>In fact, the symmetry of the surface is only threefold, as there are two distinct types of hollow sites. This is in correspondence with the two different local minima seen in the height contour in Fig. 1.2(a). However, one has to be very careful when interpreting STM images [18], and in the present case it is much more likely that the different minima are caused by the asymmetrical tip mentioned above.

that such tip traces are representative as contours of constant LDOS of the surface (see chapter 2). However, the corrugation in the LDOS of the close-packed surface at the relevant tip-surface separation is at least an order of magnitude smaller. From an experimental point of view, this is a fortunate discrepancy, as atomic resolution is more easily obtained than expected — nevertheless, it also demonstrates the present lack of insight. Several possible explanations for the enhanced corrugation have been proposed, including tip-induced localized states [20] and electronic  $d$  states of the tip [21]. Furthermore, in one study, it was suggested that adhesive forces between tip and sample could be a plausible explanation for the observed corrugation [22], while another study concluded that the attractive interaction tends to decrease the corrugation at small gap widths [23].

The possible effects of tip-surface interaction in STM is a very subtle topic. When STM is used as an imaging tool, it is often implicitly assumed that the physical processes taking place at the surface are unaffected by the strong electrical field ( $1 \text{ mV}/\text{\AA}$ – $1 \text{ V}/\text{\AA}$ ) and the presence of the tip. For moderate tunneling parameters, this might be true for a number of systems, but counter-examples also exist [24], and care must be taken in each specific case. On the other hand, tip-surface interactions can also be used deliberately as a way to manipulate matter on the atomic scale, and a precise control of the interaction is then the ultimate goal.

Figure 1.2(b) shows an example where the logo for the *Center for Atomic-scale Materials Physics* has been written on a clean Cu(100) crystal. The area shown is  $740 \times 310 \text{ \AA}^2$ , and the writing was accomplished by repeatedly indenting the tip into the surface in a well defined pattern at room temperature (RT). More sophisticated manipulation, including single-atom control, is also possible, and several examples have been reported<sup>5</sup>. Such atomic manipulations open up an extremely interesting new field of science. By “hand-building” nano-structures, it is now possible to probe the atomic world in an unprecedented manner. Not only can the resulting quantum devices serve as test systems, the assembling is also of utmost importance as the nature of the interaction employed not always is known. Usually, a feasible way of manipulation is established empirically, and the underlying physical mechanism is frequently turned into a subject of debate. A review of methods and proposed explanations in the field has been given by Stroscio and Eigler [27].

---

<sup>5</sup>Apart from the ongoing competition in producing the smallest institute or company logo, more serious tasks like, e.g., information storage, have also been addressed (for a review, see Ref. [25] or chapter 8 in Ref. [26])

## 1.4 Outline

Today, STM is a well-established and widely used surface-science technique. Nevertheless, as apparent from the overview in the previous section, there are still many unanswered questions connected to the STM junction. In many ways, it can be compared to a black box — it works, and it is by now known how to use it, but the finer details are still lacking. Since tunneling is a standard textbook problem, this may seem surprising. However, the real problem is very complex for the following reasons:

- The symmetry of the junction, consisting of a flat on one side and a tip on the other, cannot in a reasonable way be approximated by any one- or two-dimensional system. Full three-dimensional calculations are necessary.
- It is not clear how to model the tip, as the exact composition and geometry are unknown in most experiments, and furthermore, it often changes during operation.
- Electronic effects, tip-surface interactions, and the strong electrical field cannot be neglected. Very little is known about the relative importance of these complications.

As a consequence, it is very hard to calculate absolute numbers for, e.g., tunneling conductances, gap widths, barrier heights, and corrugations. So even though STM images often, with success, are interpreted as topographic maps of the surface, it is far from clear what they really represent.

The work presented in the current thesis has been focused on the physical processes taking place in the junction of an STM. Apart from investigations of the tunneling mechanism, it also includes experiments on nanowires formed between tip and surface. Preferentially, the motivation has been to gain a better understanding of the fundamental mechanisms involved. However, on a longer time scale, it is expected that work in this field will have practical implications for the interpretation of STM measurements and atomic-scale manipulation. The conduction properties of metallic nanowires may also be of importance for the development of VLSI circuits<sup>6</sup>.

Chapter 2 contains an introduction to the theory of STM. Only relatively simple models which are used in forthcoming chapters, will be covered. A description of the experimental setup follows in chapter 3, while

---

<sup>6</sup>VLSI: very large scale integration.

some very specific details concerning the measurements carried out, can be found in appendix A. The main part of the thesis has been divided into three chapters which are concerned with the different conduction regimes encountered, when a metallic tip is driven into contact with a metallic surface and subsequently withdrawn. First, the tunneling regime is investigated in chapter 4. Here, the quantity of interest is the so-called apparent barrier height (to be defined in chapter 2). Then, the transition from the tunneling regime to metallic conduction is covered in chapter 5. It is a process which involves massive atomic rearrangements, leading to the formation of a point contact. During the withdrawal of the tip a nanowire is formed. Because of the small size, the conduction is ballistic. Just before the nanowire breaks, the minimum cross-sectional area consists of very few atoms, which facilitates the observation of quantized conductance. This is the topic of chapter 6. Finally, the thesis will be summarized in English (chapter 7) and in Danish (chapter 8). The Danish summary, which is addressed to people who do not feel very comfortable with the English language, will be a slightly extended version of the English summary. As already stated, appendix A describes some technical details which are very important for the experiments but not crucial for the understanding of the thesis. Likewise, appendix B will in detail describe the statistical analysis employed.

## 1.5 Practical Remarks

For convenience and clarity, each chapter has its own list of references, and some references may therefore occur more than once. Journal names in references are abbreviated according to the standard listed in “Physical Review Style and Notation Guide” and the usual practice in Physical Review. In cases, where no standard abbreviation has been found, journal names are spelled out.

In accordance with the normal standard in STM related literature, the abbreviation STM will be used interchangeably for both *scanning tunneling microscope* and *scanning tunneling microscopy* throughout the present thesis. This should not cause any confusion, as the meaning will be clear from the context.

## References

- [1] L. de Broglie, Nature **112**, 540 (1923).

- [2] N. Bohr, *Fysisk Tidsskrift* **12**, 97 (1914).
- [3] J. R. Oppenheimer, *Phys. Rev.* **31**, 66 (1928).
- [4] R. H. Fowler and L. Nordheim, *Proc. R. Soc. London, Ser. A* **119**, 173 (1928).
- [5] J. E. Lilienfeld, *Z. Phys.* **15**, 46 (1923).
- [6] J. C. Fisher and I. Giaever, *J. Appl. Phys.* **32**, 172 (1961).
- [7] R. Young, J. Ward, and F. Scire, *Phys. Rev. Lett.* **27**, 922 (1971).
- [8] R. Young, J. Ward, and F. Scire, *Rev. Sci. Instrum.* **43**, 999 (1972).
- [9] G. Binnig and H. Rohrer, *Rev. Mod. Phys.* **59**, 615 (1987).
- [10] G. Binnig and H. Rohrer, *IBM J. Res. Dev.* **30**, 355 (1986).
- [11] G. Binnig, H. Rohrer, C. Gerber, and E. Weibel, *Phys. Rev. Lett.* **50**, 120 (1983).
- [12] R. M. Tromp, *J. Phys: Condensed Matter* **1**, 10211 (1989).
- [13] Y. Kuk and P. J. Silverman, *J. Vac. Sci. Technol. A* **8**, 289 (1990).
- [14] J. A. Stroscio *et al.*, *Phys. Rev. Lett.* **75**, 2960 (1995).
- [15] M. Schmid, H. Stadler, and P. Varga, *Phys. Rev. Lett.* **70**, 1441 (1993).
- [16] L. Ruan, F. Besenbacher, I. Stensgaard, and E. Lægsgaard, *Phys. Rev. Lett.* **70**, 4079 (1993).
- [17] T. Jung, Y. W. Mo, and F. J. Himpsel, *Phys. Rev. Lett.* **74**, 1641 (1995).
- [18] J. E. Demuth, U. Koehler, and R. J. Hamers, *J. Microsc.* **152**, 299 (1988).
- [19] Y. Kuk and P. J. Silverman, *Appl. Phys. Lett.* **48**, 1597 (1986).
- [20] E. Tekman and S. Ciraci, *Phys. Rev. B* **40**, 10286 (1989).
- [21] C. J. Chen, *Phys. Rev. Lett.* **65**, 448 (1990).
- [22] J. Wintterlin *et al.*, *Phys. Rev. Lett.* **62**, 59 (1989).
- [23] A. R. H. Clarke *et al.*, *Phys. Rev. Lett.* **76**, 1276 (1996).
- [24] L. Jiutao, R. Berndt, and W.-D. Schneider, *Phys. Rev. Lett.* **76**, 1888 (1996).
- [25] *Atomic and Nanometer-Scale Modifications of Materials: Fundamentals and Applications*, Vol. 239 of *NATO ASI Series E: Applied Sciences*, edited by P. Avouris (Kluwer Academic Publishers, Dordrecht / Boston / London, 1993).
- [26] R. Wiesendanger, *Scanning Probe Microscopy and Spectroscopy* (Cambridge University Press, Cambridge, 1994).
- [27] J. A. Stroscio and D. M. Eigler, *Science* **254**, 1319 (1991).



## Chapter 2

# Theory of Tunneling

### 2.1 Introduction

This chapter deals with the theory of tunneling with special emphasis on STM. A thorough review of theoretical studies will not be given. Instead, focus has been aimed towards derivations and results necessary for the discussions in the following chapters. The scope will therefore be limited to one-dimensional models and the perturbative Bardeen approach [1] on which the STM theory of Tersoff and Hamann is based [2]. Not only is this a simple model with a straightforward interpretation, it also connects directly to the definition of the apparent barrier height — the subject of chapter 4. If these subjects are common knowledge to the reader, the chapter may be skipped. However, special attention should be paid to the strict definition of the apparent barrier height in the subsection *Image Potential and Barrier Height* on page 29.

### 2.2 Matching Wave Functions

In the most simple theoretical approach to tunneling, a one-dimensional model with a rectangular barrier is employed (see Fig. 2.1). The electrons, with mass  $m$ , impinging on the barrier have a total energy  $E$  which is higher than the potential energy  $V(z)$  in regions 1 and 3 but lower than the top of the barrier in region 2. By solving the time-independent Schrödinger

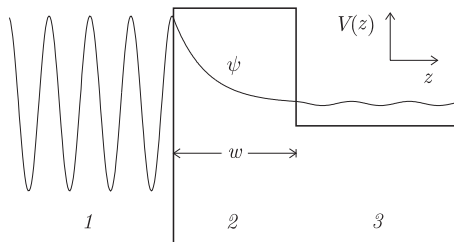


Figure 2.1: A sketch of the rectangular-barrier problem. Two electrodes, 1 and 3, are separated by a barrier of width  $w$ . In the barrier region (2), the wave function  $\psi$  decays exponentially according to Eq. (2.8).

equation,

$$\left\{ -\frac{\hbar^2}{2m} \frac{\partial^2}{\partial z^2} + V(z) \right\} \psi(z) = E \psi(z), \quad (2.1)$$

where  $\hbar$  is Planck's constant divided by  $2\pi$ , a solution to the wave function  $\psi$  in each of the three regions can be found. It has the general form,

$$\psi_l = A_l \exp(ik_l z) + B_l \exp(-ik_l z), \quad l = 1, 2, 3, \quad (2.2)$$

where  $k_1$  and  $k_3$  are one-dimensional wave vectors given by

$$k_l = \sqrt{\frac{2m(E - V_l)}{\hbar^2}}, \quad l = 1, 3. \quad (2.3)$$

As  $V_2$  is larger than  $E$ ,  $k_2$  becomes imaginary, and therefore  $\psi_2$  is not oscillatory — rather, it is a combination of two functions decaying exponentially with decay constant,

$$\kappa = \sqrt{\frac{2m(V_2 - E)}{\hbar^2}} \quad (2.4)$$

towards larger and smaller  $z$ , respectively. Relations between constants  $A_l$  and  $B_l$  in the three regions can now be found by matching  $\psi$  and  $\partial\psi/\partial z$  at the boundaries<sup>1</sup>.

Up till this point, the problem has been stationary. However, to calculate the incident and transmitted currents, a time dependence of  $\psi_l$  is

<sup>1</sup>These boundary conditions result from the physical constraint that the kinetic energy, and thus  $\partial^2\psi/\partial z^2$  [see Eq. (2.1)], has to be finite.

implicitly assumed<sup>2</sup>. From the current-density operator, given by

$$j_l = \frac{\hbar}{2im} \left( \psi_l^* \frac{\partial}{\partial z} \psi_l - \psi_l \frac{\partial}{\partial z} \psi_l^* \right), \quad l = 1, 3, \quad (2.5)$$

the two terms in Eq. (2.2) can be identified as right- and left-traveling plane waves, respectively. So, if the electrons are impinging on the barrier exclusively from region 1, then  $B_3$  will be zero, and thus the transmission  $\mathcal{T}$  can be calculated as the ratio between  $j_3$  and the incident current density  $j_{in}$ ,

$$\mathcal{T} = \frac{j_3}{j_{in}} = \frac{\hbar k_3 |A_3|^2 / m}{\hbar k_1 |A_1|^2 / m} = \frac{k_3 |A_3|^2}{k_1 |A_1|^2}. \quad (2.6)$$

As mentioned above, the boundary conditions relate  $A_3$  to  $A_1$ , and the final expression for the transmission then becomes

$$\mathcal{T} = \frac{16k_1 \kappa^2 k_3}{(k_1^2 + \kappa^2)(k_3^2 + \kappa^2)} [e^{2\kappa w} + e^{-2\kappa w} - 2\cos(2\alpha)]^{-1}, \quad (2.7)$$

where  $\alpha = \arctan(\kappa/k_1) + \arctan(\kappa/k_3)$ , and  $w$  is the width of the barrier.

Equation (2.7) is an exact expression for the transmission through a one-dimensional rectangular barrier. However, since tunneling probabilities in general are very small, one can, to a good approximation, neglect the two last terms inside the brackets. For instance, if the height of the barrier<sup>3</sup> is 5 eV, then  $\kappa$  will be roughly  $1 \text{ \AA}^{-1}$ . In other words, if the barrier has a width of a couple of ångströms or more, then  $\exp(2\kappa w)$  will dominate, and Eq. (2.7) then reduces to

$$\mathcal{T} \propto \exp(-2\kappa w). \quad (2.8)$$

Despite the simplicity of the procedure leading to Eq. (2.8), the result is characteristic for all tunneling problems — the dominating term in the expression for the transmission decreases exponentially as a function of barrier width.

---

<sup>2</sup>It is often stated that the wave-matching method is time-independent as time enters neither in Eq. (2.2) nor in Eq. (2.5). Nevertheless, the derivation of the current-density operator involves the time-dependent Schrödinger equation, which only makes sense if a time factor of  $\exp(-iEt/\hbar)$  is introduced into Eq. (2.2).

<sup>3</sup>For metal-vacuum-metal tunneling, the height of the barrier is approximately equal to the work function, and 5 eV is therefore a reasonable value.

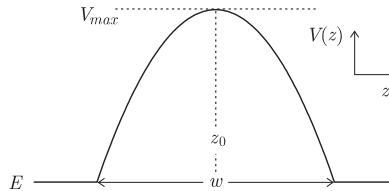


Figure 2.2: For small barrier widths  $w$ , the parabolic barrier, given by Eq. (2.9), is a more realistic model than a rectangular barrier.

### 2.3 Transmission through a Parabolic Barrier

Unfortunately, a rectangular barrier is not very representative for a physical system since, in reality, the potential  $V$  always changes continuously in space. A more realistic<sup>4</sup> one-dimensional model of the barrier is shown in Fig. 2.2. Here the barrier is a parabola given by

$$V(z) = V_{max} - \frac{1}{2}K(z - z_0)^2, \quad (2.9)$$

where  $K$  is a constant and  $z_0$  defines the center of the barrier. Although more complicated, it is also possible to solve the Schrödinger equation for this problem [3], and the exact result for transmission above and through the barrier is given by

$$\mathcal{T} = \frac{1}{1 + \exp(2\epsilon)}, \quad \text{where } \epsilon = \frac{\pi}{\hbar} \sqrt{\frac{m}{K}} (V_{max} - E). \quad (2.10)$$

In the tunneling regime, where  $V_{max} > E$ , a relation between  $K$  and the width of the barrier  $w$  can be found,

$$\sqrt{\frac{V_{max} - E}{K}} = \frac{\sqrt{2}}{4}w, \quad (2.11)$$

which makes it possible to rewrite  $\epsilon$  as

$$\epsilon = \kappa_p w, \quad \text{where } \kappa_p = \frac{\pi}{4} \sqrt{\frac{2m(V_{max} - E)}{\hbar^2}} \quad (2.12)$$

---

<sup>4</sup>While the rectangular barrier effectively is a zero-order approximation to a real barrier, the parabolic barrier is a second-order approximation.

deviates from the rectangular-barrier decay constant  $\kappa$  [Eq. (2.4)] by a factor of  $\pi/4$ . If a barrier of width 2 Å and height 5 eV is assumed, then  $\exp(2\kappa_p w)$  is by far the dominating term in the denominator of Eq. (2.10), and apart from a slightly different decay constant, the result is therefore equivalent to that already found for a rectangular barrier [Eq. (2.8)].

## 2.4 Barriers with Arbitrary Shapes

The transmission through a barrier with arbitrary shape can, in general, not be solved exactly, and one must resort to approximate methods. One standard way of proceeding is to employ the WKB<sup>5</sup> approximation [4,5]. Here, the essential idea is to make an expansion in powers of  $\hbar$ , disregarding terms higher than first order. In other words,  $\hbar$  is treated as a small number, which corresponds to approaching the classical limit. Below will be discussed why this might pose a problem in connection with STM.

In the WKB approximation, the time-independent part of the wave function is written as

$$\psi(z) = A \exp(iS(z)/\hbar) , \quad E > V , \quad (2.13)$$

$$\psi(z) = B \exp(S(z)/\hbar) , \quad E < V . \quad (2.14)$$

Using these expressions for  $\psi(z)$  in the Schrödinger equation [Eq. (2.1)] results in differential equations on  $S(z)$ . Now, by expanding  $S$  in powers of  $\hbar$ ,

$$S(z) = S_0(z) + \hbar S_1(z) + \hbar^2 S_2(z) \dots \quad (2.15)$$

and equating equal powers of  $\hbar$ , solutions for  $S_0(z)$  and  $S_1(z)$  can be found. When higher-order terms are omitted, the approximate wave functions become

$$\psi(z) = A\sqrt{k} \exp\left(\pm i \int^z k dz\right) , \quad E > V , \quad (2.16)$$

$$\psi(z) = B\sqrt{\kappa} \exp\left(\pm \int^z \kappa dz\right) , \quad E < V , \quad (2.17)$$

where  $k$  and  $\kappa$  are defined analogous to Eq. (2.3) and Eq. (2.4), respectively. From Eq. (2.17), the amplitudes of the wave function at the entrance and exit of the barrier can be found, which, in turn, gives the transmission

$$\mathcal{T} \simeq \exp\left\{-2 \int_{V(z)>E} \sqrt{\frac{2m[V(z)-E]}{\hbar^2}} dz\right\} . \quad (2.18)$$

---

<sup>5</sup>Wentzel, Kramers, and Brillouin.

If Eq. (2.18) is used to calculate the transmission for a rectangular or parabolic barrier, then it is easily found that  $\mathcal{T} \propto \exp(-2\kappa w)$ , in accordance with the results found in sections 2.2 and 2.3.

Due to the appealing simplicity of Eq. (2.18), the WKB approximation has often been applied to tunneling problems involving realistic barriers. For instance, this procedure was used by Simmons in a couple of thorough papers from 1963 [6,7] where the tunneling effect between two electrodes separated by a thin, insulating film was treated theoretically. However, care has to be taken when these results are transferred to STM-barrier problems since, strictly speaking, the WKB approximation is not valid for the small gap widths typically used in STM. This becomes obvious if the ratio of the two successive terms  $S_0$  and  $\hbar S_1$  in the expansion of  $S$  [Eq. (2.15)] is evaluated. It turns out that the WKB approximation is justified when the potential varies slowly on the scale of an electronic wavelength. As metallic Fermi wavelengths are  $\sim 5 \text{ \AA}$ , approximately the same size as the width of the tunneling barrier in STM, this criterion is not fulfilled for STM<sup>6</sup>. Furthermore, in the case of two planar electrodes separated by an insulating layer, a one-dimensional treatment seems reasonable, whereas this is certainly not true for the STM-barrier problem.

## 2.5 The Perturbative Bardeen Approach

In the previous sections, the tunneling problem has been treated in a one-dimensional model. However, the geometry of the junction in an STM, and therefore the barrier, is inevitably three-dimensional, and, unfortunately, neither the wave-matching method nor the WKB method is easily expanded into three dimensions. An alternative approach is thus needed.

The ultimate scheme for a calculation of the current in the junction would bear a large resemblance to the procedure used in section 2.2: Find the three-dimensional wave function by solving the Schrödinger equation for the combined system of tip and sample, and calculate the current density everywhere in the junction. However, even if the wave function for each isolated electrode can be found, it is far from trivial to take the effect of tip-surface interaction into account. On the other hand, as already discussed in sections 2.2 and 2.3, the wave functions decay exponentially in the barrier region with a decay constant of the order of  $1 \text{ \AA}^{-1}$ , and

---

<sup>6</sup>The wave functions given by Eq. (2.16) and Eq. (2.17) are, in fact, not applicable in the regions close to the classical turning points where  $k$  and  $\kappa$  approach zero. In STM, these regions can be thought of as encompassing the entire barrier.

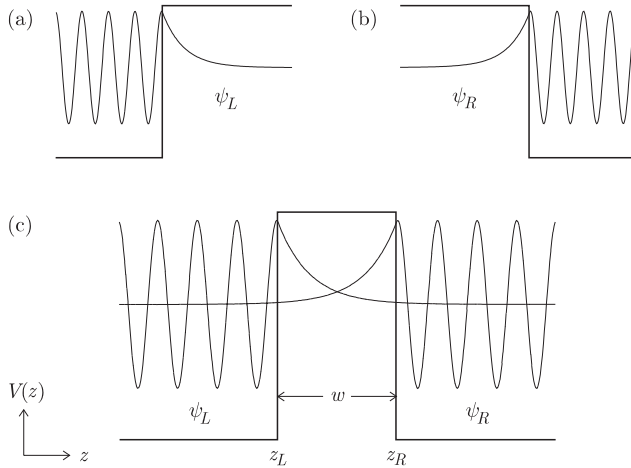


Figure 2.3: In the Bardeen approach, an approximate wave function  $\Psi$  [Eq. (2.19)] is constructed as a time-dependent linear combination of exact solutions to the two one-electrode problems shown in (a) and (b). Due to the decaying tails of  $\psi_R$  and  $\psi_L$ ,  $\Psi$  is not exact for  $z < z_L$  and  $z > z_R$  [see (c)].

since the width of a barrier usually is 3 Å or more, the overlap of the wave functions is very small. This observation led Bardeen to suggest a new perturbative approach to tunneling [1,8].

In ordinary first-order perturbation theory, an exact wave function to an approximate Hamiltonian is used to calculate the energy correction due to the perturbation. However, there is no obvious term in the tunneling Hamiltonian that can be treated as small. Instead, Bardeen solved the problem by using approximate wave functions in an exact Hamiltonian. A one-dimensional sketch of the model is shown in Fig. 2.3, where the two wave functions  $\psi_L$  and  $\psi_R$  would be exact solutions, with energies  $E_L$  and  $E_R$ , if the barrier continued to  $z = \infty$  and  $z = -\infty$ , respectively. Or phrased differently,  $\psi_L$  is the solution to the one-electrode problem shown in Fig. 2.3(a), and likewise,  $\psi_R$  is the solution to the one-electrode problem shown in Fig. 2.3(b). Now, due to the small overlap of  $\psi_L$  and  $\psi_R$  [Fig. 2.3(c)], an approximate wave function for the combined system can be written as a time-dependent linear combination,

$$\Psi = a(t) \exp\left(-i\frac{E_L}{\hbar}t\right) \psi_L + b(t) \exp\left(-i\frac{E_R}{\hbar}t\right) \psi_R. \quad (2.19)$$

Note that  $\Psi$  is exact for  $z_L < z < z_R$ , and furthermore, in the regions  $z < z_L$  and  $z > z_R$ , only the exponentially decaying tails of  $\psi_R$  and  $\psi_L$ , respectively, reduce  $\Psi$  to an approximation. Assuming again that the electrons are exclusively impinging on the barrier from the left-hand side [ $a(0) = 1$ ,  $b(0) = 0$ ] the time derivative of  $b$  (denoted  $\dot{b}$ ) can be found by solving the time-dependent Schrödinger equation which gives

$$\dot{b} = (i\hbar)^{-1} \left[ \int \psi_R^*(H - E_L)\psi_L d\vec{r} \right] \exp\left(-i\frac{E_L - E_R}{\hbar}t\right). \quad (2.20)$$

Here  $H$  is the Hamiltonian, and the integral inside the brackets is identified as the effective matrix element for tunneling, in analogy with standard time-dependent perturbation theory. Since  $H\psi_L = E_L$  for  $z < z_R$ , the integration can be restricted to  $z \geq z_b$ , where  $z_L \leq z_b \leq z_R$ . As the term  $\psi_L(H - E_R)\psi_R^*$  is zero for  $z > z_L$ , the matrix element can be symmetrized as

$$M_{LR} = \int_{z > z_b} [\psi_R^*(H - E_L)\psi_L - \psi_L(H - E_R)\psi_R^*] d\vec{r}. \quad (2.21)$$

The derivation of the effective matrix element is now completed by assuming that the tunneling process is elastic ( $E_R = E_L$ )<sup>7</sup>. Integrating Eq. (2.21) by parts, the final expression for  $M_{LR}$  then becomes

$$M_{LR} = \frac{\hbar^2}{2m} \int_S (\psi_R^* \vec{\nabla} \psi_L - \psi_L \vec{\nabla} \psi_R^*) d\vec{S}, \quad (2.22)$$

where  $S$  is an  $xy$  plane defined by  $z = z_b$ , that is, an arbitrary  $xy$  plane in the barrier region.

## 2.6 STM Theory by Tersoff and Hamann

The Bardeen approach was adopted by Tersoff and Hamann when they developed their often referenced theory of STM in 1984 [2]. Even though many theoretical studies have been carried out since then, it still stands as the theory which provides an easily tractable and general description of STM, giving some rules-of-thumb. As a perturbative calculation, it does not include any effects of tip-surface interactions, but it does include properties of the electronic structure and the three-dimensional nature of

---

<sup>7</sup>Usually, the bias voltage applied in STM is below 100 mV. The range of empty states accessible is therefore limited, and the assumption of elastic tunneling is thus reasonable.

the problem. For large gap widths, that is, small tunneling currents, the theory is therefore expected to be a reasonable approximation.

By using Fermi's golden rule, the current can be calculated from the matrix element [Eq. (2.22)] as

$$I = \frac{2\pi e}{\hbar} \sum_{T,S} f(E_T) [1 - f(E_S + eV_j)] |M_{TS}|^2 \delta(E_T - E_S). \quad (2.23)$$

Here the sum runs over all possible tip states  $T$  and sample states  $S$ . The Fermi function  $f(E_T)$  selects the filled states of the tip, while the available empty sample states are chosen by the expression in the brackets (the junction voltage  $V_j$  is applied to the sample). As already mentioned in the previous section (see footnote 7), only elastic tunneling is considered, which is the reason for the energy-conserving delta function. Furthermore, since most experiments are carried out at room temperature (RT) or below, it is reasonable to go in the limit of vanishing temperature and voltage,

$$I = \frac{2\pi e^2}{\hbar} V_j \sum_{T,S} |M_{TS}|^2 \delta(E_T - E_F) \delta(E_S - E_F). \quad (2.24)$$

For simplicity, it is assumed that tip and surface consist of the same material with Fermi energy  $E_F$ .

In order to get any further, appropriate models of tip and surface are needed. The surface can easily be described as a straightforward two-dimensional Bloch expansion,

$$\psi_S(\vec{r}_{\parallel}, z) = \Omega_S^{-\frac{1}{2}} \exp(i\vec{k}_{\parallel} \cdot \vec{r}_{\parallel}) \sum_{\vec{G}} a_{\vec{G}}(z) \exp(i\vec{G} \cdot \vec{r}_{\parallel}). \quad (2.25)$$

Here  $\Omega_S$  is a normalization volume,  $\vec{r}_{\parallel}$  is an in-plane position vector,  $\vec{k}_{\parallel}$  is a Bloch wave vector, and  $\vec{G}$  is a surface reciprocal-lattice vector. The exponential decay of the surface wave function into the vacuum is described by the  $a_{\vec{G}}(z)$  coefficients which can be calculated by noting that  $\psi_S$  has to be a solution to the Schrödinger equation outside the surface,

$$-\frac{\hbar^2}{2m} \vec{\nabla}^2 \psi_S + \mathcal{V} \psi_S = E_F \psi_S. \quad (2.26)$$

Here  $\mathcal{V}$  is the potential energy at the point of interest, and, in accordance with Eq. (2.24), focus has been put on wave functions at the Fermi level.

Using Eq. (2.25) in Eq. (2.26), the  $z$  dependence of the surface wave function can now be found as

$$\psi_S(\vec{r}_{\parallel}, z) = \Omega_S^{-\frac{1}{2}} \sum_{\vec{G}} a_{\vec{G}}(0) \exp\left(-\sqrt{\kappa^2 + |\vec{\kappa}_{\vec{G}}|^2} z\right) \exp(i \vec{\kappa}_{\vec{G}} \cdot \vec{r}_{\parallel}), \quad (2.27)$$

where  $\kappa = [2m(\mathcal{V} - E_F)/\hbar^2]^{\frac{1}{2}}$  is analogous to the decay constant defined in Eq. (2.4), and  $\vec{\kappa}_{\vec{G}} = \vec{k}_{\parallel} + \vec{G}$ .

As the tip geometry usually is far from well characterized in experiment, all STM theories, independent of complexity and accuracy, make use of a more or less *ad hoc* model of the tip. In the Tersoff and Hamann approach, the tip apex is modeled as a half sphere centered at  $\vec{r}_0$  with a radius of curvature  $R$ . The asymptotic behavior of the corresponding wave function is assumed to be an exponential decay of the form

$$\psi_T(\vec{r}) = \Omega_T^{-\frac{1}{2}} C_T \kappa R \exp(\kappa R) \frac{\exp(-\kappa|\vec{r} - \vec{r}_0|)}{\kappa|\vec{r} - \vec{r}_0|}, \quad (2.28)$$

where  $\Omega_T$  is a normalization volume, and  $\kappa$  is defined as above. Note that, at the perimeter of the sphere,  $\psi_T = \Omega_T^{-\frac{1}{2}} C_T$ , which means that the constant  $C_T$  has a value close to one.

The effective matrix element for tunneling can now be calculated by inserting Eq. (2.27) and an  $xy$ -Fourier expansion of Eq. (2.28) into Eq. (2.22),

$$M_{TS} = \Omega_T^{-\frac{1}{2}} C_T \frac{4\pi\hbar^2}{2m} R \exp(\kappa R) \psi_S(\vec{r}_0). \quad (2.29)$$

Finally, the current can be found from Eq. (2.24) and Eq. (2.29),

$$I = V_j \left[ \overbrace{\Omega_T^{-1} \sum_T \delta(E_T - E_F)}^{\rho_T(E_F)} \right] \left[ \overbrace{\sum_S |\psi_S(\vec{r}_0)|^2 \delta(E_S - E_F)}^{\rho_S(\vec{r}_0, E_F)} \right] \times \frac{8\pi^3 \hbar^3 e^2}{m^2} \exp(2\kappa R) (C_T R)^2, \quad (2.30)$$

where  $\rho_T(E_F)$  is the tip local density of states (LDOS) at the Fermi level, and  $\rho_S(\vec{r}_0, E_F)$  is the surface LDOS at the Fermi level evaluated at the center of the tip. Assuming a stable tip, that is,  $\rho_T(E_F)$ ,  $C_T$ , and  $R$  are constant in time, this equation predicts that variations in the tunneling conductance  $G = I/V_j$  only depend on the magnitude of the surface wave

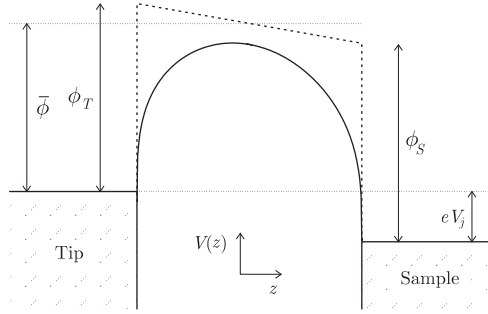


Figure 2.4: Sketch of the real barrier (solid line) and the corresponding trapezoidal approximation (dashed line). The work functions of tip ( $\phi_T$ ) and sample ( $\phi_S$ ) are indicated together with the approximate mean barrier height ( $\bar{\phi}$ ).

function at the position of the tip. This is a rather fortunate relationship as the surface is the electrode to be investigated. Equation (2.27) shows that<sup>8</sup>  $|\psi_S(\vec{r}_0)|^2 \propto \exp(-2\kappa z)$ , i.e., the current will be extremely sensitive to variations in the tip-surface separation, and consequently, at a fixed tunneling current, the tip will follow contours of constant surface LDOS at the Fermi level. By expanding  $\kappa$ , a relation between  $G$  and the energy difference  $\mathcal{V} - E_F$  can be found<sup>9</sup>,

$$G \propto \exp(-2\kappa z) \approx \exp(-1.025\sqrt{\mathcal{V} - E_F} z) \quad (\text{eV and \AA}). \quad (2.31)$$

### Image Potential and Barrier Height

In the derivation of Tersoff and Hamann,  $\mathcal{V}$  was equated with the vacuum level, and thus  $\mathcal{V} - E_F = \phi$ , where  $\phi$  is the work function of tip and sample. However, often the assumption of identical tip and sample material is relaxed, and then  $\mathcal{V}$  is evaluated in the middle of the barrier (see Fig. 2.4). Within a simple trapezoidal barrier approximation, an average barrier height  $\bar{\phi}$  can therefore be defined as

$$\mathcal{V} - E_F = \bar{\phi} = \frac{\phi_T + \phi_S - |eV_j|}{2}, \quad (2.32)$$

<sup>8</sup>The dominating term in Eq. (2.27) will be the one given by  $\vec{\kappa}_{\vec{G}} = \vec{0}$ .

<sup>9</sup>Formally,  $z$  is the coordinate of the tip center, however, as  $R$  is fixed,  $z$  can equally well be interpreted as the width of the tunneling gap. This definition will be used henceforth.

where  $\phi_T$  and  $\phi_S$  are the work functions of tip and sample, respectively. Early in the derivation, it was assumed that  $V_j$  is vanishing, which implies that the last term in the numerator of Eq. (2.32) can be neglected.

Based on Eq. (2.31) and (2.32) it has been commonly accepted to define an apparent barrier height (ABH) as

$$\phi_{ap} = 0.952 \left( \frac{d \ln G}{dz} \right)^2 = 0.952 \left( \frac{d \ln I}{dz} \Big|_{V_j} \right)^2 = 0.952 \left( \frac{d \ln V_j}{dz} \Big|_I \right)^2, \quad (2.33)$$

where  $\phi_{ap}$  and  $z$  are given in eV and Å, respectively. Here, it should be emphasized that  $\phi_{ap}$  is an experimental quantity, in the sense that it is defined from measured values of  $G$ ,  $I$ ,  $V_j$ , and  $z$ , that is,  $z$  is founded on the displacement at the base level of the tip. Even though this distinction may seem to be unimportant, it certainly is not as relaxations in the junction, caused by tip-surface forces, can give rise to a significant difference between movements at the base level of the tip and changes in gap width (see chapter 4).

In analogy with Eq. (2.32),  $\phi_{ap}$  is often compared with the average work function of tip and sample, and agreement within a factor of  $\approx 2$ –3 is indeed to be expected. However, in this approach, there is no justified reason to expect a better agreement, as the trapezoidal barrier approximation represents a highly idealized version of the real image potential reduced barrier (see Fig. 2.4). The reduction arises because an electron in the tunneling gap will experience an attractive interaction with the image charges inside the electrodes. Unlike a one-electrode problem, which only requires a single image charge, an infinite number of image charges is needed to describe the two-electrode case. For an electron, at a distance  $z_0$  from one of the electrodes, the potential will be lowered by

$$V_{image} = -\frac{e^2}{8\pi\epsilon_0} \left[ \frac{1}{2z_0} + \sum_{n=1}^{\infty} \left( \frac{nz}{(nz)^2 - z_0^2} - \frac{1}{nz} \right) \right], \quad (2.34)$$

where  $\epsilon_0$  is the vacuum permittivity. To first order,  $V_{image}$  thus goes as  $z_0^{-1}$  (this is exact for  $z_0 = z/2$ ). As the classical image potential is the asymptotic limit of the exchange-correlation potential, Eq. (2.34) does not apply close to the electrodes [9]. Nevertheless, for the electrode separations of interest in STM, the real potential will lie well below an approximate trapezoidal barrier constructed as shown in Fig. 2.4, whereas the same is not necessarily the case for the apparent barrier height [10–13]. The behavior of  $\phi_{ap}$  will be discussed further in chapter 4.

## References

- [1] J. Bardeen, Phys. Rev. Lett. **6**, 57 (1961).
- [2] J. Tersoff and D. R. Hamann, Phys. Rev. B **31**, 805 (1985).
- [3] B. S. Jeffreys, in *Quantum Theory*, Vol. 10-I of *Pure and Applied Physics*, edited by D. R. Bates (Academic Press, New York, 1961), Chap. 7, pp. 229–249.
- [4] S. Gasiorowicz, in *Quantum Physics* (John, Wiley and Sons, Inc., New York, London, Sydney, Toronto, 1974), pp. 469–471.
- [5] L. I. Schiff, in *Quantum Mechanics, International Series in Pure and Applied Physics*, 3rd ed. (McGraw-Hill, Inc., New York, 1968), pp. 268–279.
- [6] J. G. Simmons, J. Appl. Phys. **34**, 1793 (1963).
- [7] J. G. Simmons, J. Appl. Phys. **34**, 2581 (1963).
- [8] E. O. Kane, in *Tunneling phenomena in solids*, edited by E. Burstein and S. Lundqvist (Plenum Press, New York, 1969), Chap. 1, pp. 1–11, lectures presented at the 1967 NATO Advanced Study Institute at Risø, Denmark.
- [9] M. C. Payne and J. C. Inkson, Surf. Sci. **159**, 485 (1985).
- [10] J. H. Coombs, M. E. Welland, and J. B. Pethica, Surf. Sci. **198**, L353 (1988).
- [11] J. M. Pitarke, P. M. Echenique, and F. Flores, Surf. Sci. **217**, 267 (1989).
- [12] R. García-García and J. J. Sáenz, Surf. Sci. **251/252**, 223 (1991).
- [13] N. D. Lang, Phys. Rev. B **37**, 10395 (1988).



## Chapter 3

# Experimental Details

### 3.1 Introduction

This chapter contains a brief description of the experimental setup along with further information of experimental character that will be essential for the following chapters. Sections 3.2 to 3.4 will deal with details of the STM, the stage for cooling and heating, and the STM electronics, respectively. Then the various methods of measuring employed will be introduced in section 3.5, and the last two sections contain a presentation of the single-crystalline surfaces used in the present study (section 3.6) along with a brief discussion of tip stability and wetting in indentation experiments (section 3.7). For some specific technical topics, the reader is referred to appendix A.

### 3.2 The STM

A cross-sectional sketch of the Aarhus STM is shown in Fig. 3.1. It is a home built, very stable and compact ultrahigh vacuum (UHV) STM, based on a scanner tube and inchworm design. The small size, together with a rigid mounting of crystals directly on top of the STM housing, minimize the demand for external damping. A single-stage spring or viton suspension is therefore the only damping employed. Crystals can be changed *in situ* by pulling the sample holder *B* with the sample *A* away from the springs *C* which clamp the sample holder to top of the housing *D*. A new sample can then be introduced by pushing it beneath the spring load. The tip *E* is

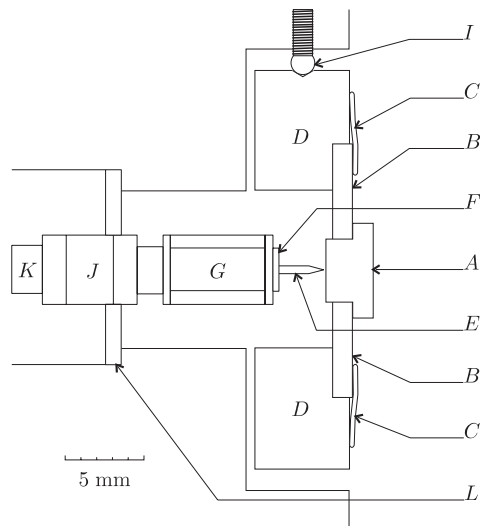


Figure 3.1: Cross-sectional sketch of the Aarhus STM. See text for details!

either made from a single-crystalline W wire of diameter 0.25 mm, which is electrochemically etched until a nice, sharp apex with crystal facets appears (Ni, Pt, and Au experiments), or from a polycrystalline Cu wire with the same dimensions cut in a sharp angle (Cu experiments). A stainless-steel plate is used as a base for the tip, and it is either spot-welded directly on top of the plate (W tips) or clamped in a capillary tube, which, in turn, is spot-welded to the plate (Cu tips). Mounting is accomplished by sliding the base plate under a U-shaped spring  $F$  glued on top of the scanner tube  $G$ . The top part  $D$  holding the sample is thermally isolated from the rest of the housing via three quartz balls  $I$ . In this way, the sample can be cooled or heated, while the STM is kept at RT.

### The Scanner Tube

The scanner tube  $G$  is a tube of piezo electric ceramics (PZT-5A) which has thin silver electrodes inside and outside. The outer electrode is divided into four equally sized electrodes ( $x$  and  $y$  electrodes) running along the tube axis, as shown in Fig. 3.1. The  $z$  movement (normal to the surface) is achieved by applying a voltage  $V_z$  to the inner electrode. For fixed voltages on the outer electrodes, the tube will lengthen/shorten if  $V_z$  is

increased/decreased. The deflection needed for the raster scanning (see Fig. 1.1 on page 11) is achieved as follows: By applying voltages  $-V_x$  and  $+V_x$  on the two opposite  $x$  electrodes, the corresponding parts of the tube will lengthen and shorten ( $V_x > 0$  V), respectively, i.e., the tube will bend over. The  $y$  deflection is controlled in the same way with voltages  $-V_y$  and  $+V_y$  on the  $y$  electrodes. Hence full three-dimensional movement of the tip is accomplished by controlling  $V_x$ ,  $V_y$ , and  $V_z$ .

### The Inchworm

Coarse approach of the tip towards the sample is performed by a linear motor, the inchworm. It consists of a piezo-electric tube  $J$  and a silicon-nitride ( $Si_3N_4$ ) shaft  $K$  on which the scanner tube is mounted, as shown in Fig. 3.1. Apart from the division of the electrodes, the tube is identical to the scanner tube described above. It is fixed to the STM housing by a rigid macor disc  $L$ , and while the inner electrode is undivided, the outer electrode is divided into three cylindrical parts with length ratios of 1:2:1. Bearings at the top and bottom fit the shaft very precisely, and by applying a positive or negative voltage to the corresponding electrodes, the bearings will clamp or unclamp the rod respectively (the inner electrode is kept at ground potential at all times). An approach cycle is as follows: The upper part clamps, the lower part unclamps, the center part expands (applying a negative voltage), the lower part clamps, the upper part unclamps, and finally the center part is contracted, i.e. the shaft, and thereby the scanner tube and the tip, is moved towards the sample. Such a cycle moves the tip approximately 2000 Å closer to the sample, however, each step of the center-part contraction can be as small as 2 Å. The approach is terminated as soon as a tunnel current is detected, and raster-scanning can then begin. At the end of scanning, the cycles are reversed and the tip is withdrawn approximately 1 mm.

### 3.3 The Heating and Cooling Stage

The original design of the spring-suspended cradle, on which the STM housing is mounted, has been changed to allow for heating and cooling of the sample. Several constraints had to be fulfilled at this redesigning phase: The performance of the STM should not deteriorate, the modifications should be kept at a minimum, and the accessibility was not allowed to change very much. Only for the latter point has the new design failed to some extent — it has become more time-consuming to take the STM

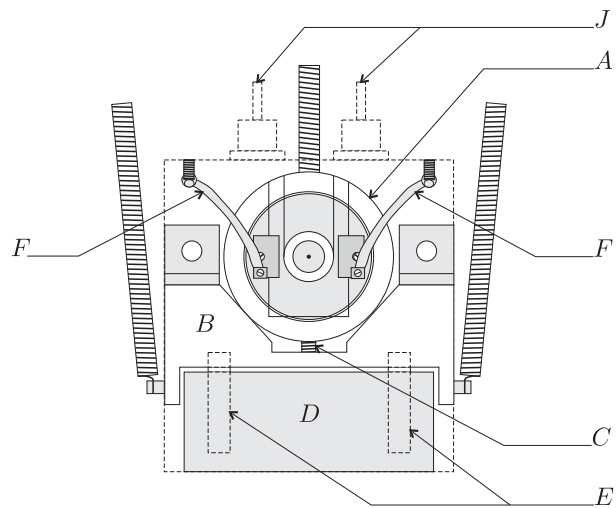
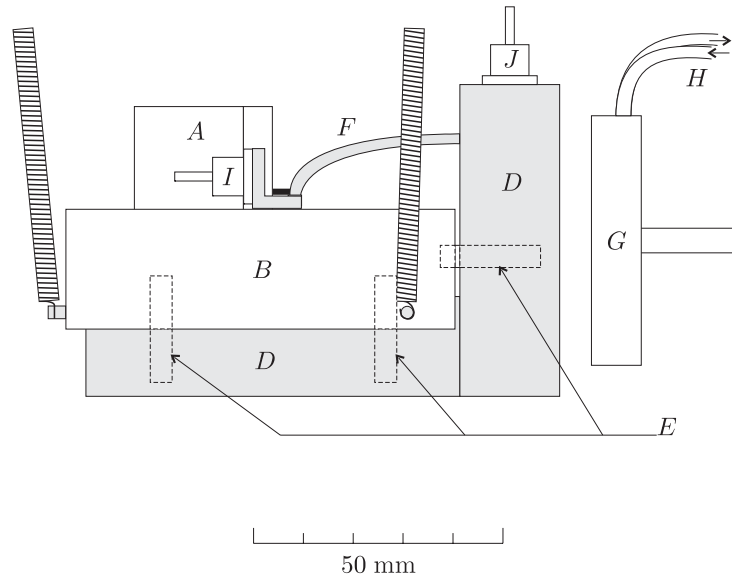


Figure 3.2: Sketch of the variable-temperature cradle and STM design.

apart. Figure 3.2 shows schematic drawings of the cradle. The STM  $A$  is lying in a trough where it is held tight to the stainless-steel block  $B$  by a screw  $C$  at the bottom. Below and in front of the STM are placed two Al blocks  $D$  that act as heat reservoirs. Aluminum has been chosen because it has the largest specific heat (0.90 kJ/kg K or 2.4 times the value of Cu) of all metals (leaving alkali and alkali-earth metals out). This is important because the weight of the entire cradle, and thereby the resonance frequency, was not allowed to change as a consequence of the redesign. Quartz tubes  $E$  and thin stainless-steel screws are used as thermal isolation between the stainless-steel block and the Al blocks. In order to be able to cool or heat the top of the STM, on which the sample is mounted (see  $D$  on Fig. 3.1), two Cu braids  $F$  connect the top to the Al blocks. Locking of the cradle is accomplished by pushing the Cu piece  $G$ , which is mounted on a linear translator, towards the vertical Al block. When the cradle is free-hanging (Cu piece retracted), there will be no mechanical coupling to the surroundings, except via the suspension springs and the wires necessary for operation of the STM, as was the case for the original version of the cradle.

Cooling is achieved by locking the cradle to make good thermal contact between the Cu piece and the vertical Al block. Then liquid N<sub>2</sub> is pumped through the tube  $H$  which intersects the Cu piece. In this way, the sample can be cooled from RT to 170 K in less than an hour, and the lower limit is approximately 140 K. During cool-down, the temperature of the STM top is typically 20 K higher than the temperature of the Al blocks. Once cooled down, the cradle is unlocked, and scanning can start. Because of the heat reservoir, the warm-up rate is as low as 6 K/hour, facilitating long periods of scanning without interruptions. A slow decrease in the temperature of the STM cannot be avoided, and two zener diodes<sup>1</sup>  $I$  have therefore been mounted on the stainless-steel block<sup>2</sup>. Due to the zener voltage of 75 V, a large power can be dissipated at a modest current level, and large cross-sectional leads can thus be avoided. Typically, the current on the two diodes is limited to 100 mA. By heating once every second hour, it is possible to keep the STM temperature within 10 K of RT.

Likewise, it is possible to heat the Al blocks, and thereby the top of the STM. This was first tested out by leading steam through the tube  $H$ . Although cumbersome, it did work out. Later two additional zener diodes  $J$  were mounted on top of the vertical Al block. A temperature above 400 K can readily be achieved within 1–2 hours. Care has to be taken in order not

---

<sup>1</sup>Diodes: BZY93C75, 20W

<sup>2</sup>Surprisingly, these diodes have proven to be UHV-compatible.

to damage the diodes, which have an upper temperature limit of 470 K.

The performance of this variable-temperature STM is demonstrated by the fact that atomic resolution of close-packed metal surfaces is easily obtained both at 170 K, RT, and 390 K. Due to the slightly non-constant temperature of the sample when scanning, the uncertainty of the temperatures stated throughout the entire thesis is  $\pm 10$  K. Note that, even though the tip initially is at RT, it is not clear whether its temperature is changed by repeatedly indenting it into a hot or cold sample. This will be elaborated on in appendix B (section B.1).

### 3.4 Electronics

STM images can be acquired in one of two modes: the constant current mode or the constant height mode. The latter is almost never used, as it is a reminiscence from the early days of STM, where the microscopes and the electronics had not yet reached the present level of perfection. In the constant current mode, a feedback loop continuously adjust the motion of the tip normal to the sample by adjusting  $V_z$  in order to keep the tunnel current constant, as the tip is raster-scanned across the surface [see Fig. 1.1(b)]. Simultaneously,  $V_z$  is recorded and shown in a color-coded format on a computer monitor, resulting in an image which, in a simple picture [see Eq. (2.31)], can be interpreted as a topographic map of the surface.

Figure 3.3 shows a sketch of the feedback loop and the data acquisition circuit, which is completely monitored and controlled from a standard IBM-compatible computer (PC) via digital-to-analog converters (*DAC*) and analog-to-digital converters (*ADC*). *DAC1* governs the bias on the sample  $V_b$  and thereby the junction voltage  $V_j$ , as the tip is on the virtual ground potential of the tunnel current preamplifier. In the preamplifier the current signal is converted to a voltage which depends on the selected range (see section A.1 in appendix A for details). The converted signal continues to the loop amplifier which compares the voltage signal for the measured current with a voltage signal for the demanded value of the current. If the measured current is too high it will result in a retraction of the tip (decreasing  $V_z$ ) and *vice versa*. From the loop amplifier, the corrected  $z$  electrode signal is fed into a low pass filter which has a cut off below the resonance frequency of the STM ( $\approx 8$  kHz). Finally, a high voltage amplifier converts the low voltage signal ( $\pm 5$  V) to a high voltage signal ( $\pm 400$  V) needed on the scanner tube.

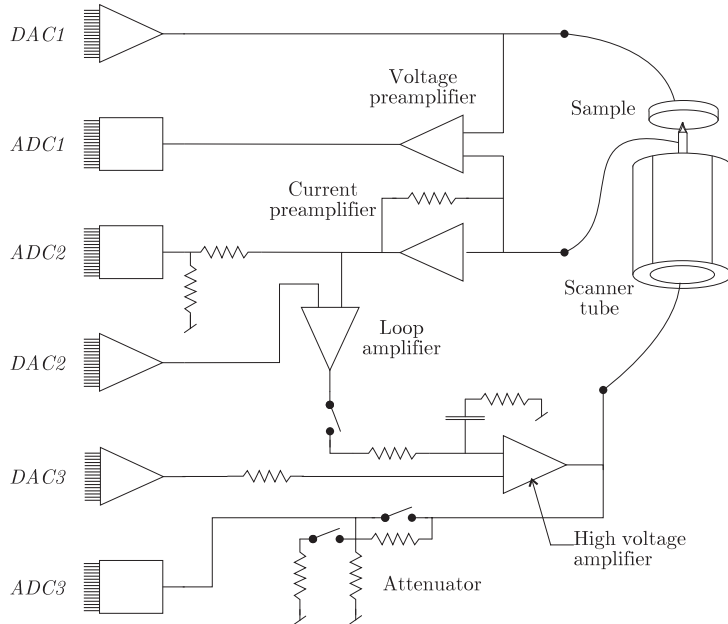


Figure 3.3: Sketch of the electronics. See text for details!

Three analog-to-digital converters ( $DAC1$ – $DAC3$ ) continuously convert the measured junction voltage  $V_j$ , the measured tunnel current  $I$ , and  $V_z$ , respectively, to 16 bit digital signals. The junction voltage preamplifier is quite unique for this setup. It is developed for a special purpose (see section 3.5 below) and is not needed during image acquisition, as the bias voltage on the sample  $V_b$  is subject to direct computer control via  $DAC1$ . In the constant current mode described above, the gain in the loop amplifier is set as high as possible to make the  $z$  piezo respond as fast as possible to changes in  $I$ . At normal conditions,  $I$  will thus, to a high precision, be equal to the demanded tunnel current controlled via  $DAC2$ . Hence,  $ADC3$ , which converts the imaging parameter  $V_z$ , is the only  $ADC$  that is really needed in the constant current mode. To be able to check that the feedback loop indeed manage to keep the current constant, the readout from  $ADC2$  is also recorded, giving rise to an averaged value of  $I$  for each image.

In the constant height mode the gain in the loop amplifier is set to a very low value, which implies that the feedback loop only responds to

very slow variations in the current, i.e., the tip follows the overall slope of the sample but not the finer details. The structure of the surface is now reflected in the readout from *ADC2*, since, again in a simple picture,  $I$  increases as the tip passes over a protrusion and *vice versa*. Constant height imaging has not been used in the experiments described, however, a special kind of current imaging has been employed (see section 3.5 below).

During raster-scanning, it is possible to interrupt the scanning in a certain pixel of the image to perform a local measurement before scanning is continued (see section 3.5 below). Here, it is often a necessity to have explicit control of the tip height independent of  $I$ . For that purpose an electronic switch is incorporated into the feedback loop. When the switch is open, the capacitor in the low pass filter keeps the  $z$  signal at a constant potential, that is, the  $z$  position of the tip is kept fixed. Alternatively, the  $z$  signal can be adjusted by superimposing a signal from *DAC3*, if, for example, a ramping of  $V_z$  is required.

### 3.5 Methods of Measuring

In this section the various methods of measuring will be described. The first two methods [ $z(I)$  and  $z(V_b)$ ] are standard to most STM implementations, whereas ABH images, error-signal images, and conductance measurements during indentations are special features of the Aarhus STM and the controlling software. Error-signal images and ABH images are multi-pixel measurements, that is, an image is formed from measurements in each single pixel of a constant current image.

#### Bias and Displacement: $z(V_b)$

At a fixed location and with closed feedback loop ( $I$  constant), the change in  $V_z$  is recorded as  $V_b$  is ramped. From a knowledge of the  $z$  calibration ( $\approx 12 \text{ \AA}/V$ ), changes in  $V_z$  are easily converted to tip displacements, which, in turn, determines the apparent barrier height through Eq. (2.33).

#### Current and Displacement: $z(I)$

This measurement is analogous to  $z(V_b)$ , however, instead of ramping  $V_b$  at constant  $I$ , it is here the demanded tunnel current which is varied at constant  $V_b$ . Again, the apparent barrier height can be determined from Eq. (2.33).

### ABH Images

In every single pixel of a constant current image, the feedback loop is opened, the tip is displaced with a preset value  $\Delta z$ , and after a short relaxation time, which typically is set to 100  $\mu\text{s}$ ,  $I(z + \Delta z)$  is measured before the tip is brought back to the original tunneling position. The difference  $\Delta I = I(z) - I(z + \Delta z)$  is recorded and stored in the corresponding pixel of the apparent barrier height image. In this way, it is possible to make a direct comparison between features in the topographic image and spatial variations in the apparent barrier height, which in analogy Eq. (2.33) is calculated as

$$\phi_{ap} = 0.952 \left\{ \frac{\ln[I(z)/I(z + \Delta z)]}{\Delta z} \right\}^2 = 0.952 \left\{ \frac{\ln[1 - \Delta I/I(z)]}{\Delta z} \right\}^2, \quad (3.1)$$

where  $\phi_{ap}$  and  $z$  are given in eV and  $\text{\AA}$ , respectively. Note that there is a distinct difference between measurements of  $z(I)$  and ABH images. In the first case, the response of the feedback loop is measured as  $I$  is changed, while, in the latter case, the decay of  $I$  irrespective of the feedback loop is measured.

### Error-Signal Images

Error-signal images are essentially current images analogous to the ones obtained in the constant height mode, the difference being that error-signal images are acquired simultaneously with a constant current image, and with the loop-amplifier gain set as high as possible. From an error signal image, it can thus be determined how precisely the feedback loop manage to keep the current constant.

### Indentations

The motion of the tip during an indentation process is depicted in Fig. 3.4 where the origin of the displacement scale corresponds to the initial tunneling position ( $\sim 1\text{--}10 \text{ M}\Omega$ ). When the tip passes a preselected point in the constant current image, the feedback loop is opened and the indentation is performed: The tip is retracted 15  $\text{\AA}$  to a position where it is allowed to relax for 1 ms before it is driven towards the surface at a rate of 320  $\text{\AA}/\text{s}$ . The tip advances beyond the initial tunneling position to an indentation depth of 4  $\text{\AA}$  where it is forced to stay for another relaxation time of 1 ms. Subsequently, the tip is withdrawn from the surface, again

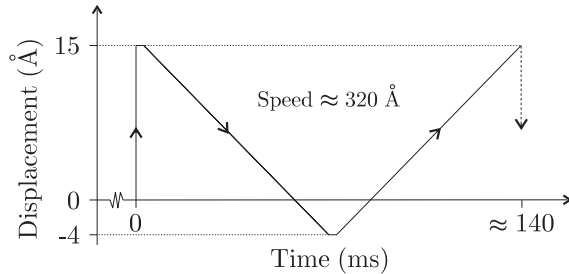


Figure 3.4: Tip-indentation sequence. See text for details!

at a rate of  $320 \text{ \AA/s}$ , back to the starting point of the indentation. Finally, the tunneling is re-established by a gentle tip approach. The above mentioned typical values can all be adjusted as appropriate. Furthermore, the bias voltage during indentations  $V_b^i$  can be set independently of the bias voltage during scanning  $V_b$ .

In order to measure the conductance  $G$  (or equivalently the resistance  $R$ ) in the tunnel junction during the indentation process, it is necessary to know *both*  $I$  and  $V_j$ . From an experimental point of view, an easy way to accomplish this is to keep the bias voltage  $V_b^i$  constant and then measure  $I$ . However, it is far from certain that the experimental setup is capable of keeping the real tunnel voltage in the junction  $V_j$  equal to the bias voltage  $V_b^i$  during the entire indentation. The assertion that  $V_j \approx V_b^i$  is only true when the effective input impedance of the preamplifier<sup>3</sup>  $R_{in}$  is orders of magnitude smaller than  $R$ . In an indentation experiment this is *not* the case as demonstrated in Fig. 4.1 on page 53, since conductances<sup>4</sup> above  $1000 \text{ \mu S}$  often are reached ( $R \leq 1 \text{ k}\Omega$ ). This problem has been circumvented by introducing a low noise ( $\approx 3 \text{ \mu V}_{RMS}$ ) high impedance ( $> 1 \text{ T}\Omega$ ) voltage preamplifier which measures  $V_j$  *directly* across the STM junction (see section 3.4 above and the more detailed discussion in section A.1 of appendix A). This setup allows a determination of  $G$  over six orders of magnitude.

<sup>3</sup>For all measurements presented throughout the thesis,  $R_{in}$  was either  $11 \text{ k}\Omega$  or  $116 \text{ k}\Omega$ .

<sup>4</sup>The conductance is here given in Siemens ( $1 \text{ S} = 1 \text{ \Omega}^{-1}$ ). Henceforth, conductances will be given in units of  $G_0 = 2e^2/h$  ( $\sim 77.5 \text{ \mu S}$ ,  $\sim 12.9 \text{ k}\Omega$ ) which is the fundamental quantum unit of conductance.

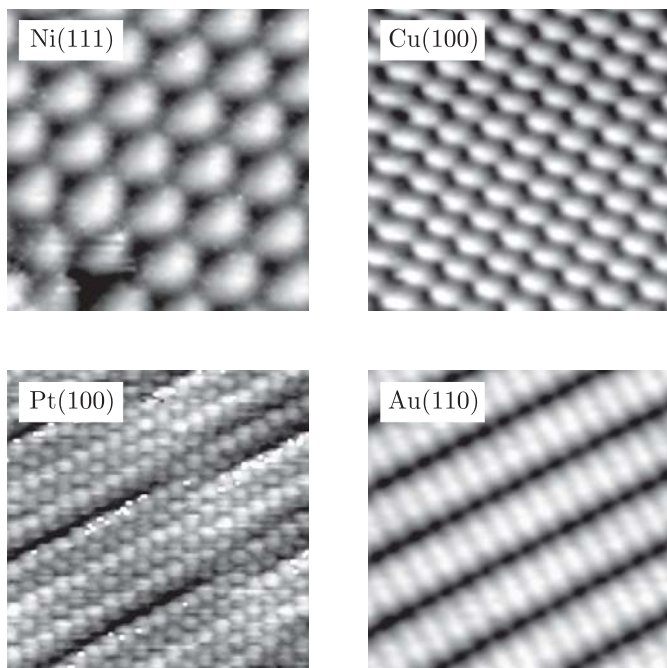


Figure 3.5: Atomic structure of the surfaces employed. The images corresponds to areas of  $12 \times 12 \text{ \AA}^2$  [Ni(111)],  $24 \times 24 \text{ \AA}^2$  [Cu(100)],  $45 \times 45 \text{ \AA}^2$  [Pt(100)], and  $40 \times 40 \text{ \AA}^2$  [Au(110)].

### 3.6 The Surfaces

The experiments included in the present thesis have been carried out on the following surfaces: Ni(100), Ni(111), Cu(100), Pt(100), Au(110). It is more or less a mere coincidence that three different facets are represented. Measurements on Ni(110) and Cu(110) have also been done, however, the indentation experiments did not reveal any significant discrepancies in the results obtained on the different facets. The initial surface-cleaning procedures included oxidation-reduction cycles and repeated Ne sputtering until perfect, impurity-free surfaces were obtained, as observed by low energy electron diffraction (LEED), auger electron spectroscopy (AES) and STM. However, due to the nobleness of Au, this surface only required a very few Ne sputterings before it was suited for experiments. The Au(110) as well as the Pt(100) surface reconstructs spontaneously at RT into a  $(1 \times 2)/(1 \times 3)$

reconstruction and a more complicated quasihexagonal overlayer structure [1], respectively (see Fig. 3.5).

### 3.7 The Tip: Stability and Wetting

When an experiment is started, the reproducibility of the indentation measurements is fairly low. One indentation to a depth of 10 Å may not lead to the formation of a neck at all, while another indentation to a depth of 2 Å produces a neck with a stretching length of more than 20 Å. These long stretching necks are often connected with a considerable tip change and a deposition of material on the crystal over an area of  $10^4$  Å<sup>2</sup>.

After a sequence of  $\sim 30 - 100$  initial indentations, each done at a new clean spot of the crystal, the situation has changed markedly. Now a single indentation will result in a very small modification of the tip, i.e. the change in tip length (measured as the change in substrate height in the corresponding topographic image) is less than 1 Å, and the overall behavior in a series of indentations is the same. It is believed that such a stable tip is the result of natural selection, that is, if an indentation by chance produces a particularly stable configuration of the tip, it is much less probable that it will undergo a change in the following indentations<sup>5</sup>.

Another likely effect of this initial “cleaning” procedure is a wetting of the tip with substrate atoms due to the lower surface energy of Ni, Cu, Pt, and Au compared to W; a picture which is supported by simulations of Landman *et al.* in the case of a Ni tip on a Au substrate [2]. Because of the wetting, the connective neck forming between tip and surface (to be described in forthcoming chapters) will mainly consist of substrate material. It will therefore be assumed that the observed behavior is characteristic for a constriction made of substrate atoms only. To verify this assumption, a Cu tip was mounted in two series of measurements on Cu(100). Indeed, these data did not deviate from data acquired with a W tip.

Often it was found to be very difficult to form a contact on Au. Sometimes, though, it worked remarkably well. This effect was not understood until it was found to be correlated with previous scanning on Ni. Indeed, it turned out that if many indentations were carried out on a Ni crystal, presumably causing a wetting of the tip, then contacts on Au could readily be produced in agreement with the simulations by Landman *et al.* [2]. These observations can be explained from phase diagrams, as W and Au are immiscible at RT whereas W and Ni alloys. Even though Ni and Au

---

<sup>5</sup>An illustrative example of the point made, is given in Fig. 5.2 on page 80

do not form a bulk alloy at RT, it has recently been shown that they do form a surface alloy [3] and, consequently, a contact can be formed.

## References

- [1] T. R. Linderoth *et al.*, Phys. Rev. Lett. **77**, 87 (1996).
- [2] U. Landman, W. D. Luedtke, N. A. Burnham, and R. J. Colton, Science **248**, 454 (1990).
- [3] L. P. Nielsen *et al.*, Phys. Rev. Lett. **71**, 754 (1993).



## Chapter 4

# Apparent Barrier Height

### 4.1 Introduction

The most fundamental quantities of any tunneling problem are the width, height, and shape of the barrier. As shown in chapter 2, they determine the transmission and, in multi-dimensional systems like the STM junction, also the distribution of tunneling particles. While both width and shape in principle can be controlled by adjusting the tip-surface distance and utilizing a tip with a certain geometry<sup>1</sup>, respectively, the barrier height for a fixed system is not subject to a direct control, but it can be found by measurements. In this way, the barrier height can be mapped out as a function of gap width at different sites on the surface. Going even a step further, it should be possible to achieve chemical specificity of surface atoms from variations in the barrier-height contour. However, despite the fact that STM by now is a well established and powerful instrument for atomic-scale imaging of clean and adsorbate-covered surfaces, detailed information on the barrier height is still very scarce. This is rather a paradox, as all STM measurements depend heavily on the characteristics of the barrier.

In this chapter, data and various aspects of the apparent barrier height, as defined in Eq. (2.33), will be presented and discussed. The chapter essentially consists of two parts following the review in the next section. In the first part (sections 4.3 and 4.4), which, to a great extent, is identical to publication IV, the apparent barrier height as a function of gap width

---

<sup>1</sup>The geometry is usually specified by an effective radius of curvature, implicitly assuming a half-spherical tip shape.

is investigated. Based on both experimental results and theoretical calculations, it will be shown that tip-surface interactions play a crucial role for the apparent barrier height at small gap widths. The last part of the chapter (sections 4.5 and 4.6) deals with the lateral variations in the apparent barrier height on the Au(110) surface (to appear in publication VI). By employing a special data-acquisition scheme, three different ways of deducing the apparent barrier height can be compared. These measurements are effectively done at “constant-tip” conditions, and discrepancies due to tip changes can therefore be ruled out. Finally, the chapter is summarized in section 4.7.

## 4.2 Review

Even before the days of STM, Binnig *et al.* used a precursor version of an STM to study the  $z$  dependence of the tunneling current [1]. A W/Pt tip-sample system was used, and a constant value of  $\phi_{ap} = 3.2$  eV was found within the  $z$  range studied. After the invention of the STM, a calibration of the gap width became possible, and Binnig *et al.* therefore repeated the experiment on a W/Au(100) system. However, the same result was obtained, i.e., a constant  $\phi_{ap}$  with a value of 3.2 eV [2]. In other words, no image-potential lowering of the barrier height was observed; a fact which the authors were able to explain in the following way: The real potential in the barrier was approximated by an image-reduced rectangular barrier with a height of  $\phi(z) = \bar{\phi} - \alpha/z$ , where the last term represents the image potential [cf. Eq. (2.34) on page 30]. If this expression for the barrier height is substituted into Eq. (2.31), and the square root in the exponent is Taylor expanded, then it turns out that the perturbation introduced by the image potential is a second-order effect in  $z^{-1}$ .

At approximately the same time, Payne and Inkson reported results from a theoretical study of the apparent barrier height deduced from measurements of  $I(z)$  and  $V_b(z)$ , respectively [3]. This work was motivated by experimental results, showing that ABH values deduced from  $I(z)$  are consistent with work functions measured by other techniques, whereas values deduced from  $V_b(z)$  are anomalously low. By considering the response of the barrier height, and the positions of the classical turning points when the gap width is increased at a constant  $I$  or  $V_b$ , respectively, they were able to understand this trend. Payne and Inkson thus concluded that the experimental results indeed suggest that the tunneling electrons are affected by the image potential.

This explanation was rejected by Coombs *et al.* [4] on the grounds of the simple mathematical identity,

$$\left[ \frac{d \ln V_b}{dz} \right]_I \times \left[ \frac{d \ln I}{dz} \right]_{V_b}^{-1} = -\frac{I/V_b}{dI/dV_b}, \quad (4.1)$$

which is equivalent to negative unity if the conductance is ohmic, as found earlier by Pashley *et al.* [5]. Accordingly, the image potential cannot be probed by a comparison of  $I(z)$  and  $V_b(z)$  measurements. Coombs *et al.* also pointed out that the approximate expression for the image-reduced barrier height employed by Binnig *et al.* was inaccurate for the gap width used in their calculation. Consequently, a more correct expression for the image potential, derived by Simmons [6], was used to study the behavior of the apparent barrier height. Again it was concluded that the image potential will have essentially no effect on the apparent barrier height. Pitarke *et al.* elaborated further on this point [7]. Here an additional  $z$ -dependent pre-exponential factor was included in the expression for the current. This gives rise to a  $z^{-1}$  term in  $\phi_{ap}$ , which, however, is rather small and vanishes whenever second- and higher-order terms can be neglected.

Although Coombs *et al.* argued for a reduced influence of the image potential on the apparent barrier height, it was noted that *the collapse of the deduced barrier heights at low tunnel barrier widths does contribute evidence for the importance of the image potential; such an effect has recently been observed.* These observations were done by Gimzewski and Möller [8]. Here the tunnel current was measured as a function of  $z$  during tip excursions as large as 6 Å. After a movement of 4 Å, a discontinuity in the current was observed. This was attributed to the formation of a contact between tip and surface (further details are given in chapter 5). However, before the onset of this current jump, a deviation from a linear relationship between the logarithm of the current and  $z$  was measured, corresponding to a collapse of the apparent barrier height. Similar results were obtained by other experimental groups [9–12].

These findings were confirmed in a theoretical study by Lang [13]. He pointed out that it is of crucial importance to realize the atomistic, three-dimensional nature of the problem when tip and surface are in close proximity. In this case, the potential-energy surface for the electrons in the gap forms a narrow hole, through which there is no direct barrier for tunneling. Nevertheless, an effective barrier arises because the constriction of the electronic motion in the direction perpendicular to the hole implies a minimum kinetic energy associated with motion in this direction (see also Refs. [14,15]). Taking these effects into account, Lang calculated  $I$

for a fixed  $V_b$  within the local-density approximation and found that  $\phi_{ap}$  decreases below the sample work function at  $z \approx 6 \text{ \AA}$ , and that it has dropped by a factor of two at  $z \approx 4 \text{ \AA}$ . In this calculation, all image effects were ignored, and the adsorbed atom was not allowed to move relative to the supporting electrode. Consequently, effects due to forces between the tip and sample cannot be expected to be well described in this calculation. However, the overall agreement with the experiment of Gimzewski and Möller was found to be very good, i.e., the collapse of the apparent barrier height at small gap widths was reproduced.

This is in contrast to the results obtained by Dürig *et al.* who measured a constant apparent barrier height independent of  $z$  for an Ir tip-sample system [16]. By referring to Lang [13] and Gimzewski and Möller [8], the authors argue that the reason why they do not observe a collapse could be *the result of an accidental cancellation of the counteracting influences of barrier collapse and increasing participation of  $d$  electrons in the conduction process at small distances*. A constant apparent barrier height was also found by Zeppenfeld *et al.* for a Pt(111) surface cooled to 4 K [17].

Yet another behavior is encountered in mechanically controllable break-junction experiments at 1.3 and 4.2 K [18,19]. In a range of less than an ångström at the smallest electrode separations, a faster-than-exponential decrease in the tunneling resistance is observed, that is  $\phi_{ap}$  increases, for decreasing gap width. According to Voets *et al.*, this effect provides evidence for strong adhesion forces [19]. Similar STM results have been reported by Chen and Hamers [20]. They deduced the apparent barrier height for a W/Si tip-sample system at RT from measurements of  $I(z)$ . An increase from 3.5 eV to a maximum of 4.8 eV was observed when the tip was moved towards the surface. Proceeding further from this point, the apparent barrier height suddenly decreased by a factor of ten within a distance of 1 Å. This drop was attributed to the formation of a contact between tip and sample. To explain the data, Chen and Hamers assumed that the “real” apparent barrier height was constantly 3.5 eV throughout the entire region studied, and that the deviation from this value was caused by a difference between the piezo displacement and the real displacement in the gap. In the attractive regime, the gap displacement would be larger than the piezo displacement, giving rise to a higher measured apparent barrier height. Likewise, in the repulsive regime, the gap displacement would be much smaller than the piezo displacement, resulting in a very low value.

Wintterlin *et al.* used a different approach when determining the apparent barrier height [21]. In experiments without any observable change

in tip conditions, the close-packed Al(111) surface was imaged with atomic resolution at different values of  $I$ . By measuring the corrugation in the corresponding images,  $\phi_{ap}$  could be determined from an expression analogous to Eq. (3.1), which resulted in a value of  $\approx 3.5$  eV. Furthermore, it was pointed out that the observed corrugations (up till 0.8 Å) clearly were inconsistent with the theory of Tersoff and Hamann, as contours of constant surface-charge density for Al(111), obtained in He-scattering experiments, exhibit a corrugation less than 0.02 Å. Instead, it was suggested that elastic deformations of the tip, due to attractive tip-surface interactions, were responsible. This explanation was rejected in a theoretical study by Ciraci *et al.* [22,23], who wrote: *In the range where attraction increases with decreasing  $z$  the tip-induced elastic deformation would reduce the corrugation of STM.* Instead, Tekman and Ciraci found that the huge corrugation on Al(111) is caused by an enhancement of the site-dependent potential barrier due to tip-induced modifications of the electronic structure [24].

The apparent barrier height was also deduced from measured corrugations in a work by Clarke *et al.* [25]. However, a new calculation scheme was used, in which any reference to variations in the gap width is avoided, i.e.,  $\phi_{ap}$  only depends on the measured corrugation, the corresponding surface reciprocal lattice vector, and the absolute value of the tunneling conductance<sup>2</sup>. In this way, values close to 2 eV were obtained on a Cu(100) surface. Moreover, Clarke *et al.* showed that, at large gap widths ( $> 4$  Å), the corrugation increases for decreasing tip-surface separation, whereas it saturates, or even decreases, at closer tip proximity. This effect was ascribed to attractive tip-surface interactions, which is in direct conflict with the suggestion of Wintterlin *et al.* [21].

The observation of anomalously low barrier heights ( $\ll 1$  eV) has been hard to reconcile in light of the more decent values obtained by other techniques. Coombs and Pethica have proposed that these low values may be explained by an elastic contact between tip and surface [27]. If this is the case, then the displacement in the gap will be a fixed fraction of the  $z$  piezo-dictated movement. Meepagala and Real reported on an experimental investigation in the case of a Au sample in air [28]. They used a combined STM and AFM to study whether the force gradient could explain the anomalously low barrier heights obtained. Even though the gradient was shown to have the correct sign necessary to cause this behavior, the magnitude was far too small, and thus *the results show that the tip-sample*

---

<sup>2</sup>A similar procedure was used by Bode and Pascal [26], however, they did not provide absolute values for  $\phi_{ap}$ .

*force gradient does not play a significant role in the lowering of the apparent barrier heights in STM measurements on gold in air.*

Anomalously low barrier heights have also been found in UHV. Schuster *et al.* studied the behavior of  $I(z)$  for a smooth and a highly corrugated metal surface [29]. The measurements were done in two ways, either by a lock-in technique or by looking at the corrugation for different currents in topographic images. On the smooth Cu(110) surface, a constant apparent barrier height of  $\approx 2.5$  eV was found for all currents over the entire distance range studied. However, on the highly corrugated Au(110) surface, the apparent barrier height measured with the lock-in technique gave 2 eV above the  $[1\bar{1}0]$  rows, while it was found to be 0.1 eV in the troughs between the rows. A more rigorous comparison showed a difference of 60–300% in  $dI/dz$  measured on top of and in between the rows, respectively. This was in contradiction to data deduced from the corrugation in topographic images which showed a difference of less than 10%. If the lock-in measured  $dI/dz$  data were correct, then an image inversion should occur when the current was varied from 16 nA to 6.3 nA. This was not observed, and since a careful examination of the experimental setup did not reveal any explanation for this discrepancy, it was concluded that *the interpretation of  $dI/dz$  measurements in terms of local barrier heights can fail on highly corrugated surfaces.*

### 4.3 Experimental Results

According to Eq. (2.33), the apparent barrier height can be deduced from the conductance curve measured during the approach sequence of an indentation. In Fig. 4.1(c) are shown four examples, one for each of the surfaces Ni(100), Cu(100), Pt(100), and Au(110). For all four surfaces, it is found that  $G$  increases exponentially in the tunneling regime until a dramatic jump occurs. At this point, a metallic contact is formed between tip and surface (to be dealt with in chapter 5). Since  $\phi_{ap}$  is defined from the logarithmic derivative of  $G$  with respect to  $z$ , these experimental results lead to the conclusion that  $\phi_{ap}$  stays constant, independent of  $z$ , until point contact is established.

As described in chapter 3, the actual voltage across the junction,  $V_j$ , is *not at all* equal to the fixed applied bias voltage,  $V_b^i$ , throughout the entire tip approach. To emphasize the importance of this point when determining  $G$  and, in turn,  $\phi_{ap}$ , Fig. 4.1(a) displays the variations in  $I$  and  $V_j$  for the measurements on Cu(100) and Au(110). In both cases, it is clearly seen

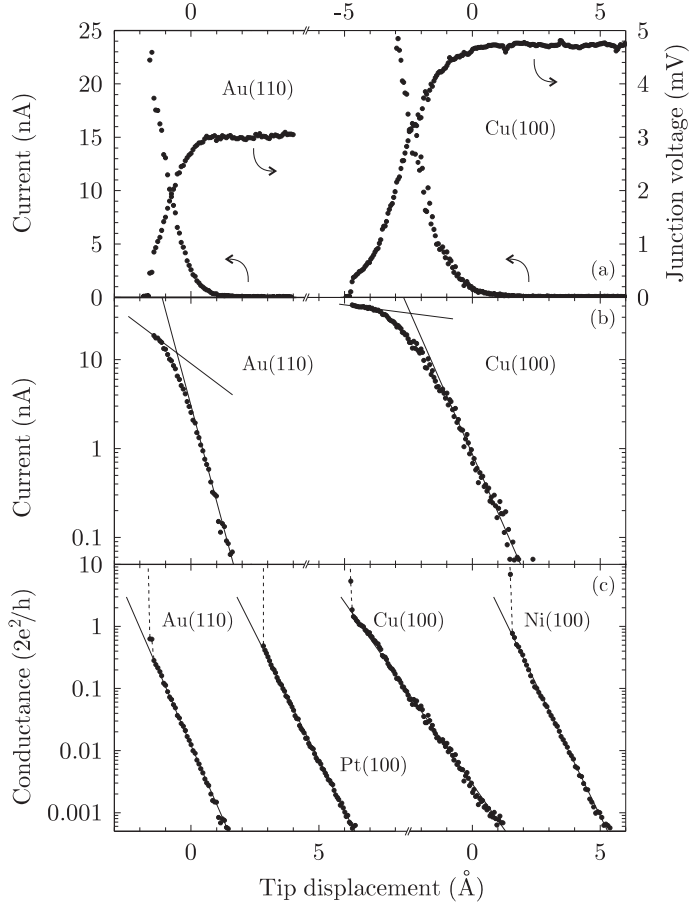


Figure 4.1:  $I$ ,  $V_j$  (a), and corresponding conductance  $G$  (c) measured during tip approach on Au(110) and Cu(100). Resulting curves for Pt(100) and Ni(100) are also shown in (c) (displaced horizontally by 4.5 Å and 3.0 Å, respectively, for clarity). For all four metals, the conductance increases exponentially, giving rise to a constant  $\phi_{ap}$ . Fitting the curves in (c) to exponential functions in analogy with Eq. (2.33) results in the following values for  $\phi_{ap}$ : 3.7 eV (Ni), 1.8 eV (Cu), 3.4 eV (Pt), and 4.7 eV (Au). When deducing  $\phi_{ap}$ , it is essential to include variations in  $V_j$ , as demonstrated in (b). If  $\phi_{ap}$  were determined exclusively from  $I$ , assuming a constant  $V_j = V_b^i$ , then the erroneous conclusion of a collapsing barrier would result, corresponding to a decrease in  $\phi_{ap}$  from 5.1 to 0.3 eV for Au, and from 2.3 to 0.02 eV for Cu.

Table 4.1: Average values for the apparent barrier height measured at 170 K, RT, and 390 K. For Ni and Pt, only RT data are available. The percentage of indentations, in which a value of  $\phi_{ap}$  can be determined consistently, is also listed. For all average values shown here, this percentage amounts to more than 170 individual indentations.

	Surface	170 K	RT	390 K
$\phi_{ap}$ (eV)	Ni(111)	—	$3.63 \pm 0.07$	—
	Cu(100)	$3.67 \pm 0.09$	$2.43 \pm 0.05$	$1.76 \pm 0.02$
	Pt(100)	—	$3.75 \pm 0.04$	—
	Au(110)	$3.95 \pm 0.04$	$3.2 \pm 0.2$	$2.83 \pm 0.06$
Percentage included	Ni(111)	—	85%	—
	Cu(100)	61%	55%	85%
	Pt(100)	—	99%	—
	Au(110)	91%	47%	71%

how  $V_j$  drops towards zero when the junction resistance becomes comparable to the input impedance of the preamplifier (116 k $\Omega$  for the data shown in Fig. 4.1). Consequently, the behavior of  $\phi_{ap}$  *cannot* be determined solely from variations in  $I$ , as is demonstrated in Fig. 4.1(b)<sup>3</sup>. Here  $I$  has been plotted on a logarithmic scale, and it is immediately evident that the slope decreases in magnitude when the gap width is diminished. So, if  $\phi_{ap}$  had been evaluated exclusively from variations in  $I$ , erroneously assuming that  $V_j = V_b^i$ , then a decreasing  $\phi_{ap}$ , i.e., a collapsing barrier, would have been the result. In this specific case, a decrease from 2.3 to 0.02 eV for Cu and from 5.1 to 0.3 eV for Au can be deduced. However, by including the variations of  $V_j$  in the right way [cf. Fig. 4.1(c)],  $\phi_{ap}$  is found to be constant with values of 1.8 eV and 4.7 eV, respectively.

In Table 4.1 are listed average values of  $\phi_{ap}$  from indentations on Ni(111), Cu(100), Pt(100), and Au(110). For Ni(111) and Pt(100), only RT data are available, whereas measurements also have been carried out at 170 K and 390 K for Cu and Au. Although representative, not all conductance curves in a data set look like the ones showed in Fig. 4.1.

<sup>3</sup>If the input impedance of the preamplifier is orders of magnitude smaller than the lowest junction resistances obtained in the tunneling regime, which correspond to approximately one quantum unit of conductance  $\approx 12.9$  k $\Omega$ , then the voltage variation in the junction is negligible, and  $\phi_{ap}$  can be determined from  $I$  only.

Table 4.2: Experimental and theoretical values for the work function listed and calculated by Skriver and Rosengaard (Ref. [30]).

	Ni(111)	Cu(100)	Pt(100)	Au(110)
Experiment (eV)	5.35	4.59	—	5.40
Theory (eV)	5.77	5.26	6.97	5.40

Occasionally, there are strong indications for atomic mobility and restructuring in the junction. Most often, this is revealed as a sudden increase or decrease in  $G$ , after which an exponential behavior is resumed, that is, the conductance curve is merely displaced along the  $y$  axis. An example is shown in Fig. 5.5 on page 84. Often, it is still possible to deduce a value for  $\phi_{ap}$  in these cases, based on the largest unbroken part of the curve. More rarely, many irregular jumps in  $G$  are observed in the main part of the tunneling regime, and then a deduction of  $\phi_{ap}$  is impossible. Included in Table 4.1 is therefore also the percentage of the total number of indentations, in which  $\phi_{ap}$  could be determined consistently (more than 170 indentations in each case).

As immediately apparent from Table 4.1, no anomalously low apparent barrier heights are found. By comparing with the work-function values listed in Table 4.2, it is seen that, at RT,  $\phi_{ap}$  is typically lying in the range from 50% to 70% of the work function, and the general trend in the two tables is the same, i.e., both the work function and  $\phi_{ap}$  are slightly lower for Cu compared to the other metals. This is not surprising as the two quantities are related, however, as already discussed in chapter 2, there is no reason to expect that they should be exactly equal. Further inspection of Table 4.1 reveals that, for Cu and Au,  $\phi_{ap}$  decreases for increasing temperature. This cannot be caused by a temperature-induced change in the sensitivity of the  $z$  piezo as that would give rise to the opposite effect<sup>4</sup>, and moreover, the temperature of the STM itself is always held at RT as described in chapter 3. When experiments are carried out at 170 or 390 K, the conductance measurement is calibrated after the initial cooling/heating procedure has been completed, and, as described in appendix B, the measurement is double-checked by making yet another

<sup>4</sup>The sensitivity of the piezo decreases for decreasing temperature, that is, a larger voltage has to be applied in order to cause a specific displacement. From outside, this will be interpreted as if the tip is moved a distance larger than the real change in gap width, and consequently, a reduced value for  $\phi_{ap}$  would result, which is in contradiction with Table 4.1.

calibration at the end of each experiment. However, essentially no drift is revealed after several hours of data acquisition, and thus it is concluded that the temperature dependence of  $\phi_{ap}$  is a real physical effect of the junction. Finally, it is noted that for both Cu and Au, the percentage of indentations, in which a value of  $\phi_{ap}$  can be deduced consistently, is smaller at RT compared to the two other temperatures.

## 4.4 Discussion

Before entering a discussion of the results presented in the previous section, a few general remarks about the apparent barrier height will be made. First, it should be emphasized that caution has to be exercised when  $\phi_{ap}$  is interpreted as a measure of the average barrier height. In fact, only when  $\phi_{ap}$  is independent of  $z$  does it have a straightforward interpretation at relatively large gap widths. This is evident from the derivation in chapter 2, leading to the definition of  $\phi_{ap}$  [Eq. (2.33)]. Here it was implicitly assumed, when taking the derivative of  $G$  with respect to  $z$ , that  $\bar{\phi}$  is independent of  $z$ . Also, from a physical reasoning, the inadequacy of  $\phi_{ap}$  can easily be recognized. Consider a pure tunneling problem, in which the height of the barrier by some means can be varied. If the height is held constant, then  $G(z)$  would increase exponentially as  $z$  (the barrier width) is decreased, as characteristic for tunneling [like in Fig. 4.1(c)]. Now, if the barrier height is increased at the same time as the width is decreased, then a slower-than-exponential increase in  $G(z)$  would obviously be the result [compare to Fig. 4.1(b)], i.e., the absolute value of  $d \ln G(z)/dz$  decreases for decreasing  $z$ , which, in turn, would give rise to a *decreasing*  $\phi_{ap}$ . So, when the real barrier height increases,  $\phi_{ap}$  decreases. Furthermore, it has been pointed out by García-García and Sáenz that a pre-exponential factor,  $1/z$ , in the expression for the tunneling current has been disregarded when defining  $\phi_{ap}$  [31]. What makes the picture even more complicated is the existence of an additional effective barrier at the smallest gap widths, due to the constricted electronic motion in the  $xy$  plane [13–15].

In the light of the discussion concerning increasing/decreasing corrugations due to relaxations in the junction [21–23,25], it is instructive also to examine how the apparent barrier height is affected by tip-surface forces. Only attractive forces are considered, as repulsive forces will not be encountered before tip and surface are in mechanical contact. Figure 4.2 is a schematic illustration showing the implications of attractive tip-surface forces. Two contours of motion are depicted; one outlined by the center

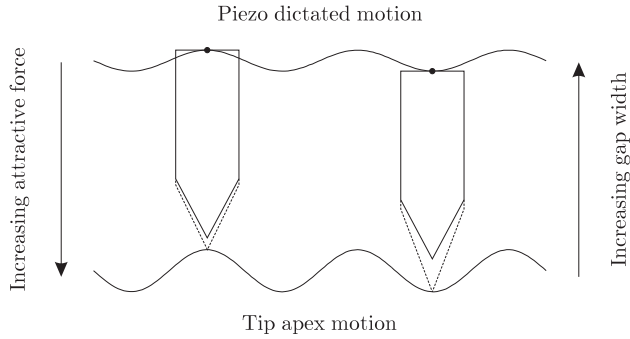


Figure 4.2: Schematic illustration of the force-induced difference between the piezo-dictated displacement of the tip and the motion of the apex. Only attractive forces are considered, which causes an elastic elongation of the tip (indicated by dashed lines). As the gap width is decreased, the total interaction force becomes larger, and, consequently, the elongation is increased. See text for further details!

point at the base of the tip, and another followed by the apex. Due to the attraction, the tip will be elastically elongated<sup>5</sup>. If the gap width is decreased, the total attractive force on the tip is increased, i.e., the elongation becomes larger and *vice versa*. As a consequence, the displacements in the gap,  $dz_{gab}$ , are larger than the corresponding displacements at the base level of the tip<sup>6</sup>,  $dz$ . Since a deduction of  $\phi_{ap}$  is based on  $dz$  rather than  $dz_{gab}$ , the effect of the attractive forces is to *increase* the absolute value of  $d \ln G/dz$ , and thus  $\phi_{ap}$ .

Returning to the results of the previous section, it can immediately be noted that the data presented in Fig. 4.1 exhibit no sign of an image-potential lowering of  $\phi_{ap}$ , in accordance with the predictions [2,4,7]<sup>7</sup>. However, the constant apparent barrier heights found in Fig. 4.1 are at variance with most experimental STM measurement of  $\phi_{ap}$  reported [8–12]. Dürig *et al.* did find a constant  $\phi_{ap}$ , though, which they attributed to an in-

<sup>5</sup>This argument is not restricted to tip deformations. More generally, the difference between the unperturbed and the dashed tip contours in Fig. 4.2 can be regarded as the total change in gap width due to attractive forces.

<sup>6</sup>This simple argument immediately rules out attractive tip-surface interactions as a possible source of huge corrugations in STM, as suggested by Winterlin *et al.* [21].

<sup>7</sup>In fact, it will be very hard to disentangle an image-potential lowering effect, as a collapse of the barrier is found even in theoretical calculations, in which the classical image potential has been neglected [13].

creasing tunnel-current contribution from the  $d$  electrons of Ir as the gap width is diminished. This explanation can be excluded on basis of the results in Fig. 4.1, since the  $d$ -band levels of Cu and Au lie approximately 2 eV below the Fermi energy [32], whereas both Ni and Pt have  $d$  bands crossing the Fermi energy. The  $d$  electrons can therefore not be responsible as  $V_b^i$  was far below 2 V (less than 5 mV) for all the indentations shown in Fig. 4.1.

It is characteristic for all experimental investigations, in which a collapsing barrier has been found, that  $\phi_{ap}$  is deduced from variations in  $I$  only. As demonstrated in Fig. 4.1(b), this can easily lead to wrong conclusions, depending on the specifications of the experimental setup. The same procedure was also used by Zeppenfeld *et al.* [17], however, they considered the problem carefully, as is evident from the following: *Particular care was devoted to correct the measured conductance for the internal impedance of the electrometer used to measure the tunneling current and to account for possible current and voltage offsets. If omitted, significant systematic errors are introduced especially in the most interesting region close to tip-sample contact!* Zeppenfeld *et al.* found a constant apparent barrier height all the way to the point of contact. This indicates that a possible explanation for the collapsing barriers found in other experiments is the lack of a proper inclusion of tunnel-voltage variations caused by a decreasing junction resistance during tip approach. However, this can only be a supposition (see also footnote 3 on page 54).

Considering Lang's theoretical investigation of the apparent barrier height [13], in which  $\phi_{ap}$  decreased to half its original value over a distance of  $\approx 2 \text{ \AA}$ , it is not obvious how the experimental findings of a constant  $\phi_{ap}$  can be conceived. However, attention should be paid to the fact that Lang's model was static, i.e., effects due to attractive tip-surface forces are *not* treated in this calculation. Since Dürig *et al.* reported experimental evidence for exponentially increasing adhesive forces at decreasing gap widths [16], and furthermore, the effect of these forces is to increase the measured  $\phi_{ap}$ , as discussed above, it seems promising to pursue the relationship between  $\phi_{ap}$  and attractive forces in greater detail.

In the following, the experimental findings will be compared with the results of a conductance calculation which includes the full three-dimensional character of the electronic potential between tip and surface. This calculation of  $G$  is carried out for a geometry similar to the one used by Lang [33,13], with a single atom between two jellium surfaces. The tip-surface separation, however, is obtained from a simulation of the atomic structure in the junction.

The conductance calculation is carried out as follows<sup>8</sup>: First, the electron density is calculated as a simple superposition of the density from a Au atom (tip) and from the two jellium surfaces with  $r_s = 3$  bohr, appropriate for Au. From the electron density, the potential is then obtained as the electrostatic potential plus the exchange-correlation term in a local-density approximation. The transmission coefficient for the motion of an electron from one jellium surface to the other through the tip atom is calculated using a recursive coupled-channel technique with a plane-wave basis set, and then, finally, the conductance can be found from the Landauer expression for ballistic electron transport (consult chapter 6).

As input to the conductance calculation are used the actual distances from the tip atom to the jellium surfaces, as calculated from atomistic simulations<sup>9</sup>. Here the tip is modeled by a pyramid-shaped structure [see insert in Fig. 4.3(a)] consisting of nine Au(100) layers with 1, 4, 9, . . . , and 81 atoms, respectively, while a slab of nine Au(100) layers with  $12 \times 12$  atoms in each layer represents the substrate. Atoms in the three top-most layers of the tip and the three bottom layers of the substrate are static [shown as filled circles in Fig. 4.3(a)], and the atomic interactions are described by potentials derived from the effective-medium theory [34]. Further theoretical details are given in publication IV.

In the simulations, the static part of the tip is lowered towards the surface in steps of 0.005 Å. Between each step, the atomic positions are relaxed by a minimization procedure similar to steepest descent (see Ref. [35] for details). For comparison, molecular-dynamics simulations of the tip-surface approach at 300 K have also been performed. The results are rather similar those obtained with the minimization technique, but the contact formation is initiated about 0.2 Å further from the surface in the finite-temperature simulations because of thermal fluctuations. Other tip geometries have also been tried, e.g., a more blunt [110] oriented tip with a single apex atom. The results differ in the details, but the overall behavior is the same.

As the tip approaches the surface, it is stretched due to the attractive, adhesive forces acting between tip and surface. Furthermore, the atoms in the surface below the tip apex are displaced towards the tip. These relaxations imply that the actual separation between tip and surface is smaller than if the tip and surface were static. Approximately 25% of the total decrease in tip-surface distance is provided by an increase of the bond length between the apex atom and the four atoms in the next layer of

---

<sup>8</sup>Performed by M. Brandbyge.

<sup>9</sup>Performed by M. R. Sørensen.

the tip. The relaxations of the atoms in the rest of the tip contribute with approximately 50%, and the remaining 25% arises from the displacements of the surface atoms. In Fig. 4.3(a) is shown the actual tip-surface distance as a function of the unrelaxed gap width. As a consequence of the contact-formation process, which occurs at an unrelaxed separation of 3.2 Å, the total deformation jumps from  $\approx 0.5$  Å (before) to the maximum value of

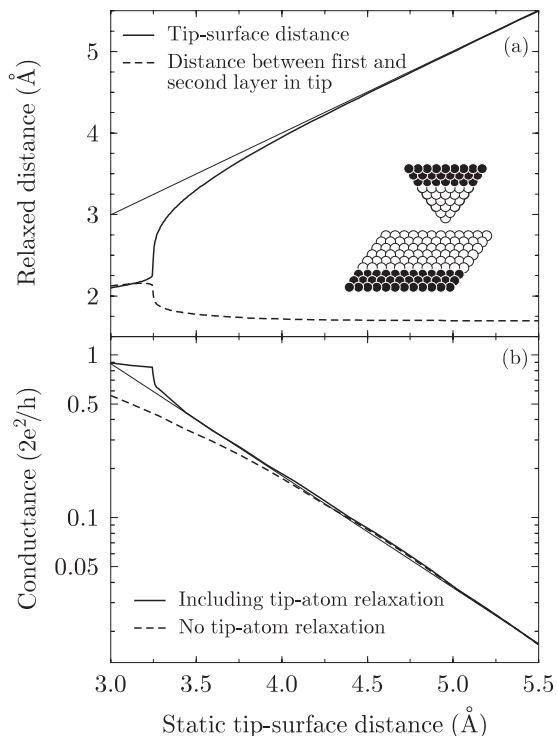


Figure 4.3: (a): The actual distance between the tip atom and the surface as a function of the static distance (defined as the distance between tip atom and surface in the absence of tip-surface forces). The insert shows the configuration used in the simulation. (b): The calculated conductance as a function of the static distance in the case where relaxations are taken into account (full curve) and when they are not (dashed curve). For the latter curve, the corresponding apparent barrier height varies from about 3.5 eV at a separation of 6 Å to 0.6 eV at 3 Å.

1.0 Å (immediately after), as seen in Fig. 4.3(a).

Figure 4.3(b) is a plot of the calculated conductance in the case of a Au/Au tip-surface system. The dashed curve shows how, in the case of a static tip atom, a saturation of the conductance begins to set in which corresponds to a decreasing  $\phi_{ap}$  for decreasing tip-surface distance. This is equivalent to the result obtained by Lang [13]. When the relaxations are included (full curve), the saturation is compensated for by the attraction of the tip atom towards the surface over a distance of about 1 Å (compare to Fig. 4.1). At closer approach, the relaxation effect even dominates so that the conductance increases slightly faster than exponential before the formation of a contact. This latter behavior is observed in break-junction experiments at low temperature ( $\leq 4.2$  K) [18,19]. A reason why this is not observed at RT may be that the onset of contact formation occurs farther from the surface. This can either be caused by thermal fluctuations, as observed in the simulations, or because activated processes, which are not described on the time scale of the molecular-dynamics simulations, become possible as the temperature is raised (in chapter 5 it will be shown that the latter explanation indeed is very plausible).

In conclusion, it has been shown that it is of crucial importance to include variations in  $V_j$ , when deducing  $\phi_{ap}$  — otherwise, the erroneous conclusion of a collapsing barrier may be the outcome. Furthermore, the constant apparent barrier height found experimentally can be explained by including effects of the strong, attractive tip-surface forces at small gap widths, which works to counteract the collapse of  $\phi_{ap}$  found in static calculations.

The interpretation becomes more subtle and speculative when the values presented in Table 4.1 are considered. As a starting point, it can be noted that thermal activation must play a substantial role for the processes taking place in the junction. This can be inferred from the temperature dependence seen in the lower panel of Table 4.1. Indentations, in which a deduction of  $\phi_{ap}$  fails, are characterized by instabilities and irregular conductance jumps in the tunneling regime, as described in the previous section. Since these are bound to be caused by atomic motion in or near the junction, it is reasonable to conclude that the apparent barrier height can be extracted more often at 170 K than at RT due to thermal activation. However, this picture does obviously not hold when comparing RT and 390 K data as the success rate is highest at 390 K. It might be speculated that the mobility at 390 K is so high that each data point in an indentation curve represents an average over several conductance jumps. A rough estimate can be made, based on the diffusion rate given

by  $1/\tau = \nu \exp(-E_a/k_bT)$ , where  $\nu$  is an attempt frequency,  $E_a$  is the activation energy, and  $T$  is the absolute temperature. If the mean time  $\tau$  between events is 10 ms at RT, and the usual attempt frequency of  $10^{13} \text{ s}^{-1}$  is assumed, then the rate will be a factor of  $\approx 350$  higher<sup>10</sup> at 390 K, i.e.,  $\tau$  will be smaller than the time resolution in these measurements (270  $\mu\text{s}$ ). However, it is not clear why the conductance jumps are accompanied by a *decreasing*  $\phi_{ap}$  for increasing temperatures. If the gap width decreases faster than dictated by the piezo, then an increasing  $\phi_{ap}$  would result, as discussed above. In analogy, a decreasing  $\phi_{ap}$  corresponds to a gap width which decreases *more slowly* than dictated. This can either be accomplished by a movement of atoms away from the junction or by a relief of strain in the tip-surface system. Both scenarios seem very unlikely in view of the increase in attractive forces at decreasing tip-surface distances. In conclusion, further experiments are required to clarify the matter.

## 4.5 Atom-Resolved Apparent Barrier Height

Among the most severe problems in STM are the lack of an easy and reliable way to define or characterize the tip and the frequent and uncontrollable changes in tunneling behavior caused by reconstructions taking place in the junction. Consequently, it is not obvious how to measure absolute reproducible values for, e.g., the apparent barrier height since the ability to reproduce data will depend on the ability to re-establish previous experimental conditions, including a certain state of the tip. An often used approach is to employ special tip-treatment procedures [36] to make the tip as stable as possible. Then a suitable kind of average can be formed by repeating the measurement numerous times. In this way, peculiarities of the individual measurements are averaged out, and a representative value of the quantity under investigation is found<sup>11</sup>. This is the method employed in section 4.3.

Experiments described in this section represent an alternative approach. Here, much effort has been used in order to achieve a particularly stable tip configuration for an extended period of time. Measurements of  $z(I)$ ,  $z(V_b)$ ,

---

<sup>10</sup>Here it is important to note that only the sample is cooled/heated, as described in chapter 3. It is not clear whether the tip stays at RT, or it is affected by the temperature of the sample (see also section B.1 in appendix B)

<sup>11</sup>Obviously, the average formed in this way is subject to the overall geometry and structure of the tip. So, if a comparison is carried out between different experiments, then it is implicitly assumed that the “average” tips were the same. In most cases, this assumption is not justified.

and ABH images were carried out. Since the tip stayed constant during the experiment<sup>12</sup>, a *direct* comparison of apparent barrier-height values, deduced from the three independent ways of measuring, can be carried out. It is the hope that these experiments can shed light on the discussion between Payne and Inkson on the one hand [3], and Coombs *et al.* on the other [4] (see section 4.2). The Au(110) surface was chosen for these investigations for two reasons: First, due to the  $p(1 \times 2)/p(1 \times 3)$  reconstruction, the periodicity perpendicular to the close-packed rows is fairly long ( $\geq 8 \text{ \AA}$ ), and atomic-scale variations in  $\phi_{ap}$  can therefore routinely be obtained. Secondly, the Au(110) surface was used in the experiment by Schuster *et al.*, where inexplicable anomalously low values of  $\phi_{ap}$  were found [29].

Figure 4.4 shows a topographic image (b) together with the corresponding current image (d). As the two images have been acquired at the same time (details can be found on page 41), they represent the same  $23 \times 25 \text{ \AA}^2$  surface area. The rows of the  $p(2 \times 1)$  reconstruction are easily identified in (b), whereas no resolution along the rows is seen. White horizontal lines in (b) and (d) indicate the locations of the contours shown in (a) and (c), respectively. That is, while the tip was following the contour depicted in (a) the current shown in (c) was recorded. First, it can be noted that the operation of the feedback loop clearly is reflected in (a) and (c): When the current is higher/lower than the preset value [compare with dotted line in (c)], the tip is withdrawn/advanced. This is the reason for the apparent phase shift of the images in (b) and (d). Moreover, the corrugation is measured to be  $\approx 1 \text{ \AA}$ , and from the symmetry of the contour in (a), it can be inferred that the tip geometry does not give rise to any obscure effects. Finally, the mean value of the current [dotted line in (c)] is found to be  $1.254 \pm 0.009 \text{ nA}$ . The smallest deviations from the mean value are recorded where the slope of the height contour in (a) is zero, that is, in between and on top of the rows.

The results presented in Fig. 4.4(c) can be used to estimate the uncertainty of  $\phi_{ap}$  deduced from the apparent barrier-height image shown in Fig. 4.5(d). Here the lateral variation in  $\Delta I$  for a normal displacement of  $\Delta z = 0.45 \text{ \AA}$  is shown (see description on page 41). From the coincidence of maxima and minima in (b) and (d)<sup>13</sup>, it can be concluded that  $\phi_{ap}$  attains the highest and lowest values on top of and in between the

<sup>12</sup>The absence of tip changes was inferred from a visual inspection of topographic images along with measurements of a constant corrugation height.

<sup>13</sup>A small phase shift of 1–2  $\text{\AA}$  is apparent from the contours in (a) and (c). It is not clear whether this is caused by the non-symmetric variation in the current seen in Fig. 4.4, a slightly asymmetric tip, a  $z$  movement which is not exactly normal to the

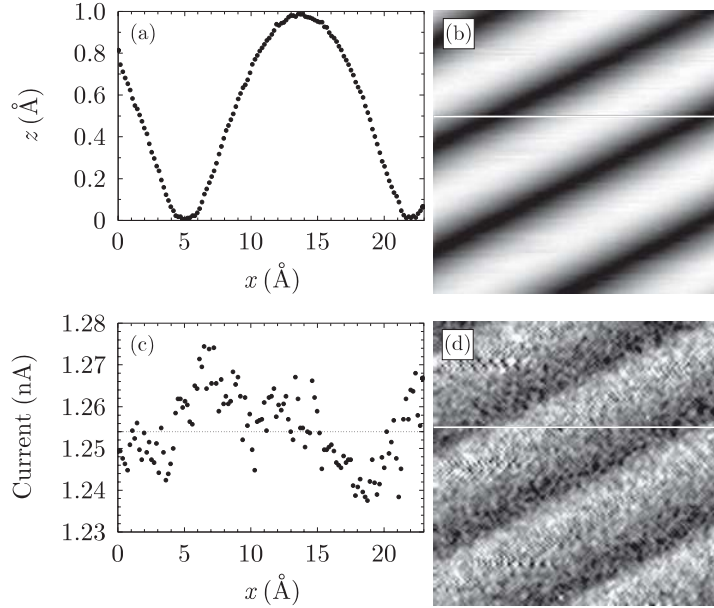


Figure 4.4: Simultaneously acquired topography (b) and current image (d) of a  $23 \times 25 \text{ \AA}^2$   $p(1 \times 2)$  reconstructed area on Au(110). Contours along the same horizontal scan line [indicated by a white line in (b) and (d)] are shown in (a) and (c). The dotted line in (c) corresponds to the mean value of the current throughout the line scan. Parameters were  $I = 1.25 \text{ nA}$  and  $V_b = 432 \text{ mV}$ . See text for further details.

rows, respectively, as expected<sup>14</sup>. The contour of  $\Delta I$  in (c) has been fitted to a sinusoidal function, with an amplitude of  $0.032 \text{ nA}$  around a mean value of  $0.736 \text{ nA}$ . From Fig. 4.4(c) and Fig. 4.5(c), it is estimated that, at maxima and minima positions of the height contour, the uncertainty on  $I$  and  $\Delta I$  is  $0.005 \text{ nA}$  and  $0.01 \text{ nA}$ , respectively. Since the conductance is very low (of the order  $10^{-5}$  quantum units), attractive forces are not expected to cause any significant elastic deformation in the junction. Consequently, an uncertainty of 10% on  $\Delta z$  is assumed. From Eq. (3.1)  $\phi_{ap}$  can now be deduced, and it is found to vary from  $3.2 \pm 0.2 \text{ eV}$  between the

surface, or a combination of these.

<sup>14</sup>At the present tunneling conditions, the corrugation was observed to decrease for increasing gap width, in agreement with Ref. [25]. This means that the conductance decreases faster on top of the rows than between rows, i.e.,  $\phi_{ap}(\text{top}) > \phi_{ap}(\text{between})$ .

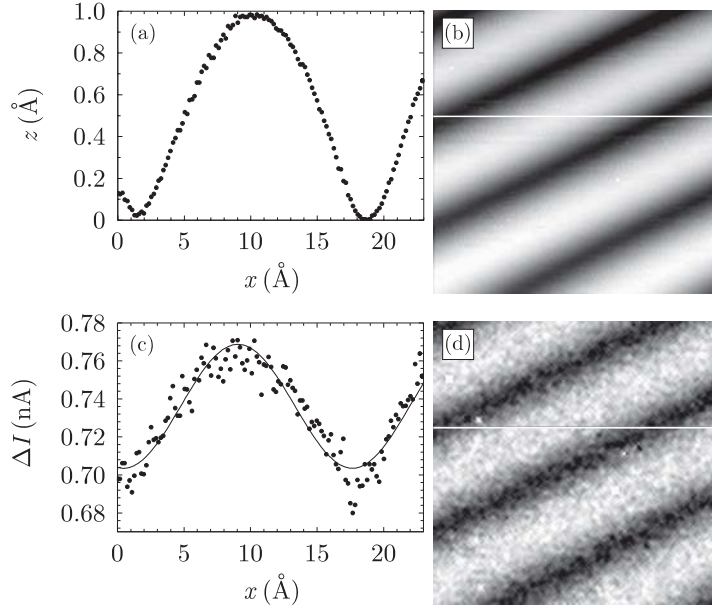


Figure 4.5: As in Fig. 4.4 except that (d) is an apparent barrier height image ( $\Delta z = 0.45$  Å) rather than a current image. The contour in (c) has been fitted to a sinusoidal function, with an amplitude of 0.032 nA around a mean value of 0.736 nA. A relaxation time of 100  $\mu$ s was used (see page 41).

close-packed rows to  $4.3 \pm 0.3$  eV on top of the rows. During a series of three sets of images, these values were confirmed to within 0.1 eV. Here, it should be emphasized that all measurements presented in this section have been performed with an 116 k $\Omega$  input resistance of the preamplifier, a minimum bias voltage of 24 mV, and a maximum current of 1.3 nA. Consequently, the difference between  $V_b$  and  $V_j$  will be less than 150  $\mu$ V, and it can therefore be neglected.

Figure 4.6 displays data from eleven measurements of  $z(I)$  performed on top of the close-packed rows (a) and in the troughs between the rows (b). In both cases, the data points are seen to gather around a straight line. For each measurement, a fit to a function  $z = \alpha \ln I + \beta$  has been made, yielding a value of  $d \ln I / dz = \alpha^{-1}$  which, in turn, determines the apparent barrier height via Eq. (2.33). The results for  $\phi_{ap}$  are  $4.2 \pm 0.1$  eV (on top) and  $3.6 \pm 0.1$  eV (in trough).

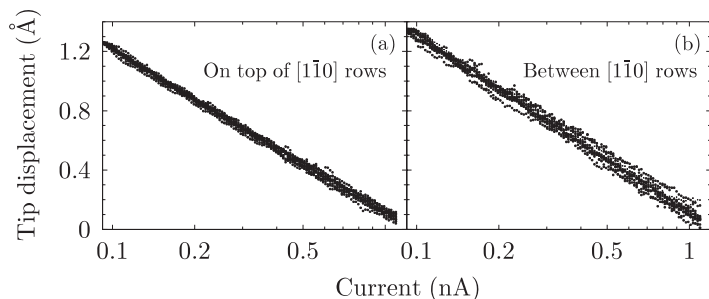


Figure 4.6: Data from eleven measurements of  $z(I)$  on top of (a) and in between (b) the close-packed rows. The bias voltage was  $V_b = 432$  mV.

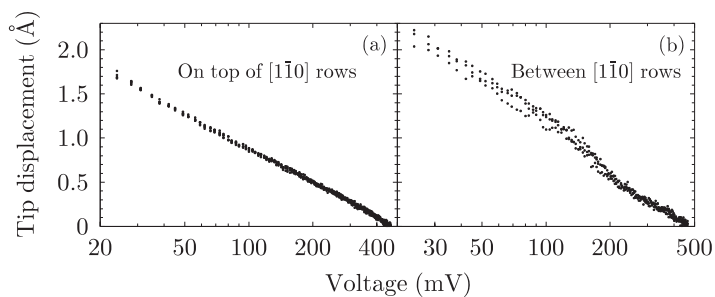


Figure 4.7: Data for  $z(V_b)$  from five measurements on top of the close-packed rows (a), and three measurements between the rows (b). The current setpoint of the feedback loop was 1.26 nA.

Likewise, Fig. 4.7 contains data from measurements of  $z(V_b)$ . Unfortunately, the constant tip conditions did not last forever, and therefore only five and three measurements were available on top of and in between the rows, respectively. By proceeding in the same way as above,  $\phi_{ap}$  is found to be  $3.0 \pm 0.1$  eV on top of the rows. The interpretation of the data in (b) is less straightforward as a bend in the curve is seen in the range 120–230 mV. However, it is reasonable to make a fit in the two separate sections below and above the bend. This results in a value of  $2.2 \pm 0.2$  eV for  $V_b < 120$  mV and  $2.7 \pm 0.2$  eV for  $V_b > 230$  mV. In Table 4.3, the results of the present section are summarized.

Table 4.3: Values for the apparent barrier height (given in eV) deduced from apparent barrier height images,  $z(I)$ , and  $z(V_b)$ .

	ABH image	$z(I)$	$z(V_b)$
$\phi_{ap}(\text{top})$	$4.3 \pm 0.3$	$4.2 \pm 0.1$	$3.0 \pm 0.1$
$\phi_{ap}(\text{between})$	$3.2 \pm 0.2$	$3.6 \pm 0.1$	$2.2^\dagger, 2.7^\ddagger \pm 0.2$

$^\dagger V_b < 120$  mV

$^\ddagger V_b > 230$  mV

## 4.6 Discussion of Atom Resolved Apparent Barrier Height

The result presented in the previous section demonstrates that it is possible, consistently to atomically resolve a variation of 15–25% in the apparent barrier height. An inspection of Table 4.3 reveals that none of the methods employed resulted in anomalously low values<sup>15</sup>. This is in contrast to the findings of Schuster *et al.* [29] who obtained values as low as 0.1 eV between the rows of the  $p(1 \times 2)$  reconstruction of Au(110). Furthermore, it is seen that there is a fair agreement between values deduced from  $z(I)$  and ABH images. Here, it is also interesting to note that the value of 3.95 eV obtained from indentations on Au (Table 4.1) is lying in the middle of the range from  $\phi_{ap}(\text{between})$  to  $\phi_{ap}(\text{top})$ . This is to be expected as the indentations described in section 4.3 were made at random lattice sites.

Albeit only a small number of  $z(V_b)$  measurements were carried out, there is no doubt that, at the tunneling conditions used in the present study, the resulting values for  $\phi_{ap}$  are approximately 30% lower than values deduced at a constant  $V_b$ . This is an important input to the discussion concerning possible differences between measurements done at a constant voltage and at a constant current, respectively. If the tunnel current for a specific setup only is a function of  $z$  and  $V_b$ , and the gap is ohmic, then the argument by Coombs *et al.* [4], based on the mathematical identity in Eq. (4.1), is definitely convincing. However, if the exponent in the relation between  $G$  and  $z$  really depends on  $V_b$ , as suggested in Eq. (2.32), then the gap is not ohmic since  $I/V_b \neq dI/dV_b$ , and Eq. (4.1) does not apply. According to the results in Table 4.3, this indeed seems to be the

<sup>15</sup>Based on the work of Gimzewski and Möller [8], it is often stated that such high values for the apparent barrier height are indicative of a clean tip.

case. Although the values deduced here are not anomalously low, as those referred to by Payne and Inkson [3], this does support their picture in which the change in separation between the classical turning points of an image-reduced barrier is different from the change in gap width.

Finally, the bend in Fig. 4.7(b) will be commented on. Since all measurements were intermixed, that is, both on-top and  $z(I)$  data were acquired in between each of the measurement presented in Fig. 4.7(b), a change in tip conditions can be excluded as a possible cause of the bend. Moreover, as Fig. 4.7(a) does not reveal a similar effect, it must be site-specific. Judged solely from the data, an appealing explanation is therefore a site-specific spectroscopic effect. However, it is far from evident how this can be conceived in terms of the band structure of Au.

## 4.7 Summary

The present chapter has focused on the apparent barrier height which is defined from the logarithmic derivative of the tunneling conductance with respect to gap width. In section 4.3 it was found that, contrary to both theoretical predictions employing a static geometry of the junction and most experimental results reported, the apparent barrier height stays constant all the way to the point where a contact is formed between tip and surface. That is, no collapse of the barrier was detected. In this connection, the importance of a proper inclusion of variations in the junction voltage was emphasized, and it was shown that if a deduction of  $\phi_{ap}$  was based solely on variations in the tunneling current, which is analogous to what has been done in the majority of apparent barrier-height measurements, then the erroneous conclusion of a collapsing barrier resulted. Moreover, values for  $\phi_{ap}$  at RT were found to lie in the range from 50% to 70% of the work function, and for both Cu and Au  $\phi_{ap}$  decreased for increasing temperature. Section 4.4 started out with a discussion of the relation between the apparent barrier height and the average of the real barrier height, and it was stressed that only when  $\phi_{ap}$  is independent of gap width does it have a simple interpretation. Then it was shown that the effect of increasing attractive tip-surface forces at decreasing electrode separation is to increase the apparent barrier height, an effect which counteracts the collapse of the barrier predicted in static calculations. Within this picture, the constant apparent barrier height found experimentally could be explained. Next, data from a “constant-tip” experiment on atom-resolved apparent barrier heights were presented in section 4.5. Here three different ways of mea-

suring  $\phi_{ap}$  were employed. In all cases, a 15–25% variation perpendicular to the close-packed rows of the  $p(1 \times 2)$  reconstructed Au(110) surface was deduced (highest on top of rows and lowest in troughs between rows), and no anomalously low values were obtained. Good agreement was found between values based on ABH images and  $z(I)$ , whereas  $z(V_b)$  gave values lying 30% lower. These results were in section 4.6 interpreted as evidence for a gap which is not purely ohmic, and they also seem to support the work of Payne and Inkson [3].

## References

- [1] G. Binnig, H. Rohrer, C. Gerber, and E. Weibel, *Appl. Phys. Lett.* **40**, 178 (1982).
- [2] G. Binnig *et al.*, *Phys. Rev. B* **30**, 4816 (1984).
- [3] M. C. Payne and J. C. Inkson, *Surf. Sci.* **159**, 485 (1985).
- [4] J. H. Coombs, M. E. Welland, and J. B. Pethica, *Surf. Sci.* **198**, L353 (1988).
- [5] M. D. Pashley, J. B. Pethica, and J. Coombs, *Surf. Sci.* **152/153**, 27 (1985).
- [6] J. G. Simmons, *J. Appl. Phys.* **34**, 2581 (1963).
- [7] J. M. Pitarke, P. M. Echenique, and F. Flores, *Surf. Sci.* **217**, 267 (1989).
- [8] J. K. Gimzewski and R. Möller, *Phys. Rev. B* **36**, 1284 (1987).
- [9] Y. Kuk and P. J. Silverman, *J. Vac. Sci. Technol. A* **8**, 289 (1990).
- [10] I.-W. Lyo and P. Avouris, *Science* **253**, 175 (1991).
- [11] R. Berndt, J. K. Gimzewski, and R. R. Schlittler, *Ultramicroscopy* **42-44**, 528 (1992).
- [12] G. Doyen *et al.*, *Phys. Rev. B* **48**, 1738 (1993).
- [13] N. D. Lang, *Phys. Rev. B* **37**, 10395 (1988).
- [14] S. Ciraci and E. Tekman, *Phys. Rev. B* **40**, 11969 (1989).
- [15] K. Hirose and M. Tsukada, *Phys. Rev. B* **51**, 5278 (1995).
- [16] U. Dürig, O. Züger, and D. W. Pohl, *Phys. Rev. Lett.* **65**, 349 (1990).
- [17] P. Zeppenfeld, C. P. Lutz, and D. M. Eigler, preprint (unpublished).
- [18] J. M. Krans *et al.*, *Phys. Rev. B* **48**, 14721 (1993).
- [19] J. Voets, R. J. P. Keijsers, O. I. Shklyarevskii, and H. van Kempen, *Phys. Rev. B* **53**, 1072 (1996).
- [20] C. J. Chen and R. J. Hamers, *J. Vac. Sci. Technol. B* **9**, 503 (1991).
- [21] J. Wintterlin *et al.*, *Phys. Rev. Lett.* **62**, 59 (1989).

- [22] S. Ciraci, A. Baratoff, and I. P. Batra, Phys. Rev. B **42**, 7618 (1990).
- [23] S. Ciraci, Ultramicroscopy **42-44**, 16 (1992).
- [24] E. Tekman and S. Ciraci, Phys. Rev. B **42**, 1860 (1990).
- [25] A. R. H. Clarke *et al.*, Phys. Rev. Lett. **76**, 1276 (1996).
- [26] M. Bode and R. Pascal, Triannual report 1993-1995, Microstructure Advanced, Research Center Hamburg, University of Hamburg (unpublished).
- [27] J. H. Coombs and J. B. Pethica, IBM J. Res. Develop. **30**, 455 (1986).
- [28] S. C. Meepagala and F. Real, Phys. Rev. B **49**, 10761 (1994).
- [29] R. Schuster *et al.*, Ultramicroscopy **42-44**, 533 (1992).
- [30] H. L. Skriver and N. M. Rosengaard, Phys. Rev. B **46**, 7157 (1992).
- [31] R. García-García and J. J. Sáenz, Surf. Sci. **251/252**, 223 (1991).
- [32] O. Jepsen, D. Glötzel, and A. R. Mackintosh, Phys. Rev. B **23**, 2684 (1981).
- [33] N. D. Lang, Phys. Rev. B **36**, 8173 (1987).
- [34] K. W. Jacobsen, J. K. Nørskov, and M. J. Puska, Phys. Rev. B **35**, 7423 (1987).
- [35] M. R. Sørensen, K. W. Jacobsen, and P. Stoltze, Phys. Rev. B **53**, 2101 (1996).
- [36] C. J. Chen, *Introduction to Scanning Tunneling Microscopy, Oxford series in optical and imaging sciences* (Oxford University Press, New York, 1993), Chap. 13, pp. 281-293.

## Chapter 5

# Contact Formation

### 5.1 Introduction

The physics underlying contact-formation processes between a probe tip and a sample surface has recently attracted much attention from both experimental and theoretical side. Not only is it of importance to the SPM community to achieve an improved knowledge of forces that tend to drive probe and sample into contact while measuring, the tribological implications are more profound than may be anticipated at first. Since ordinary surfaces are not atomically flat, but rather consist of many asperities on a corrugated support, contact phenomena are dominated by the interaction between such asperities [1]. These interactions are thus important ingredients in a detailed description of macroscopic adhesion, friction, and wear, and the model system consisting of SPM tip and sample is therefore of more direct technological relevance than is usually the case in pure science [2].

Furthermore, it is expected that advances in the field may have an impact on the understanding of the material-transfer techniques used in SPM for atomic-scale manipulation. This is due to the lack of a clear-cut distinction between contact formation immediately followed by disruption and a process where material is expelled from one electrode, transferred, and subsequently adsorbed on the other electrode. At least from an experimental point of view, it can, under certain conditions, be very hard to disentangle these two scenarios — a fact which indeed has led to discussions in the literature.

Despite the large number of studies carried out, the nature of the

processes that lead to the formation of a contact is still a subject of debate. Many explanations have been proposed, and, as a further complication, there are reasons to believe that different mechanisms can be responsible, depending on the circumstances under which the individual experiment is carried out. This will be clear from the review in section 5.2 which has been included in order to provide a context for the rest of the chapter. Experimental results for Ni, Pt, and Au are presented and discussed in sections 5.3 and 5.4, respectively. Sections 5.5 and 5.6 have been devoted to a presentation and a following discussion of new experimental evidence for a polarity-dependent effect in contact formation. Here, measurements on a Cu tip-sample system will be given a special emphasis, as they do not seem to fit into any of the existing frameworks in the field. Finally, the last section of the chapter contains a brief summary.

## 5.2 Review

Experiments can largely be divided into three main groups according to the way in which a contact or transfer process is initiated. An often used procedure is to apply a short voltage pulse to the electrodes while they are within tunneling distance from each other. Topographic images recorded before and after the pulse reveal that this procedure can lead to the formation of mounds and/or pits on the surface, i.e., material is transferred to or from the sample. Another approach, which conceptually is the most simple way to establish a contact, is to mechanically drive the tip towards the surface. Frequently, the result of this procedure, after a subsequent separation of the electrodes, is also a net transfer of material. The last group of experiments bears a large resemblance to the previous one, except that here the contact is formed spontaneously without any apparent change in tunneling parameters.

Many of the voltage-pulse experiments have been motivated by the prospects of ultrahigh density storage [3]. If it is possible to write stable atomic-scale structures on surfaces with SPM, then the technique may form the basis for tomorrow's information storage devices. A real example was first demonstrated by Becker *et al.* who succeeded in making protrusions on a Ge(111) surface in UHV by raising the tip bias to -4 V at a constant current of 20 pA [4]. A "bit" size as small as a very few or maybe even a single atom was achieved in this way. It was suggested that the protrusions consisted of Ge atoms transferred from tip to sample<sup>1</sup>, however, no physical

---

<sup>1</sup>In this study, a W tip was used, and it was therefore assumed that Ge atoms were

explanation for the transfer process was proposed. Becker *et al.* also tried to make the same kind of manipulation on a Si(111) surface, but it failed. Four years later, Lyo and Avouris demonstrated how single atoms of the  $7 \times 7$  reconstruction of Si(111) could be removed (3 V pulse on sample) and later redeposited (-3 V pulse on sample) at another location on the surface [5,6]. A threshold field for transfer of  $\approx 1 \text{ V/\AA}$  was found, and it was argued that field evaporation would be the most likely effect. Similar conclusions were reached by a team at the *Aono Atomcraft Project* [7–9]. However, in this case no correlation was found between the polarity of the voltage pulse and the direction of the transfer process, and furthermore, the probability for a transfer process was shown to be independent of the magnitude of the current [7]. Interestingly enough, it was also reported that in more than 40% of the events, the transfer process happened after the voltage pulse was over [9].

Another set of voltage-pulse experiments have been performed on Au surfaces in air. In the first of these, Schneir *et al.* used a PtIr tip and voltage pulses larger than 0.7 V in order to write a “T” on a Au surface [10]. However, the procedure was not very reproducible, and both polarities could result in pits instead of mounds. Li *et al.* reported similar results, except that in this case, the majority of events created pits on the surface, while mounds only were formed occasionally [11]. A threshold voltage for the “electro-etching” process was found to be  $\approx 2.7 \text{ V}$ , and it was suggested that the observed phenomenon was an explosive substrate evaporation due to a large power dissipation in a small sample volume below the tip. This was questioned in a comment by Marella and Pease who pointed out that the thermal diffusion length for Au is  $\approx 10 \mu\text{m}$ , and that a possible temperature increase therefore would be smaller than 1 K, which is inconsistent with a thermally activated evaporation process [12].

Nearly two years later, Mamin *et al.* demonstrated in a thorough experiment with a Au tip how mounds could be made in a very reproducible way [13]. With closed feedback loop and tunneling conditions, short (300 ns) voltage pulses of 3.6 V were applied to the sample. Even pulses with a duration as short as 10 ns resulted in reproducible mounds. At fixed tunneling conditions, the probability for mound formation was observed to increase from 0 to 1 when the pulse voltage was increased from 0.2 V below to 0.2 V above a certain threshold voltage  $V_{th}$  (3.4–4.0 V depending on tunneling parameters). Furthermore,  $V_{th}$  increased linearly with the logarithm of the gap impedance, that is,  $V_{th}$  increased linearly with electrode separation. An upper limit on the corresponding critical field was

---

present on the apex of the tip due to a previous indentation into the surface.

evaluated to be  $0.4 \text{ V}/\text{\AA}$ . No differences between positive and negative polarity were found except a slightly lower  $V_{th}$  in the case of negative pulses. These results were interpreted as a clear indication of a field effect, and the physical mechanism was suggested to be field evaporation. Mamin *et al.* noted that the critical field was an order of magnitude lower than observed in field ion microscopy (FIM). However, it was also pointed out that this could be caused by the close proximity of the electrodes in STM.

These conclusions were rejected in a later paper by Pascual *et al.* as the required flux of ions would be several orders of magnitude higher than previously observed for ion emission from Au tips [14]. Experiments also showed that applying a  $14 \mu\text{s}$  long  $6 \text{ V}$  pulse to a sample resulted in a  $10 \text{ ms}$  current pulse. The magnitude of the current pulse corresponded to a junction resistance of  $267 \Omega$  ( $V_b = 0.4 \text{ V}$ ) which was attributed to a contact between tip and sample. As further evidence, two mounds were produced, one by a voltage pulse and another by mechanically forcing tip and sample into contact, and no essential difference between the mounds was observed. Pascual *et al.* thus concluded that in both cases, the observed protrusion was a result of a broken contact. Moreover, it was proposed that the contacts could be formed either by an electric pile-up effect where hillocks are generated on both tip and sample as a consequence of the field<sup>2</sup>, or by a mechanical deformation due to an attractive electrostatic force between tip and sample. Mamin and Rugar responded in a comment by providing further evidence for their interpretation [16]. A current trace from a  $900 \text{ ps}$  pulse was shown, and the corresponding junction resistance was at no point lower than  $10^7 \Omega$ . Still a mound was formed. Mamin and Rugar also argued that even in cases where a contact is formed, this could be caused by field evaporation.

This discussion was taken up by Taylor *et al.* who observed two kinds of behavior, one in which the current decreased exponentially after the pulse, and another where the preamplifier stayed at the saturation level until the tip was withdrawn several nanometers [17]. While a mound was produced in nearly all cases where saturation occurred, only 25% of the exponential events produced mounds. Taylor *et al.* concluded that field evaporation could explain the exponential events, whereas saturation was consistent with the formation of a contact. Chang *et al.* also argued in favor of field evaporation [18]. In their experiment, both pits and mounds were formed at a threshold field of  $\approx 0.6 \text{ V}/\text{\AA}$ , and as contact formation

---

<sup>2</sup>Very recently, Méndez *et al.* reported on observations of field-assisted diffusion on a Au(111) surface at fields as low as  $0.2 \text{ V}/\text{\AA}$  [15]. The authors suggest that field-assisted diffusion could be a responsible mechanism for mound formation.

cannot explain pits, it was inferred that field evaporation indeed was the predominant mechanism.

Eigler *et al.* used voltage pulses when they demonstrated how a Xe atom on a Ni(110) surface at 4 K could be switched back and forth between tip and surface in a reproducible way [19]. However, in this case, the Xe transfer was always directed towards the positively biased electrode. As the  $6s$  resonance of Xe lies 4–5 eV above the Fermi level, negative ion formation, and thereby field evaporation, seemed improbable. Furthermore, no threshold field was observed; instead the probability for transfer per unit time at a gap resistance of 906 k $\Omega$  depended on the magnitude of the voltage pulse as  $V^{4.9\pm 0.2}$ . On these grounds, Eigler *et al.* speculated that the mechanism underlying the transfer process could be electromigration, as previously suggested by Ralls *et al.* [20].

A number of theoretical papers have addressed the pulse-induced transfer/contact process, and further mechanisms have been proposed. For instance, Tsong argued that field evaporation was unlikely to take place at the low field strengths used in the experiment of Mamin *et al.* [21]. Instead, Tsong suggested that the tip apex melts as a consequence of resistive joule heating, resulting in a liquid-metal cone bridging tip and sample. Later on, this opinion was apparently revised, as Tsong was co-author on a couple of papers dealing with field evaporation in double-electrode systems [22,23]. In these papers, results were presented which showed that doubly charged negative ions should be favored in STM field evaporation of Si and Au.

Lang also studied the pulse-transfer mechanism and found that due to the narrow gap width in STM, both Al and Si atoms would transfer towards the negatively biased electrode, with a net positive charge lower than a few tenths of the electronic charge [24,25]. Although related, this process deviates substantially from the usual picture of field evaporation in which an ion is formed and subsequently ripped off the surface by the field. Similar results were obtained by Hirose and Tsukada from first principles for the case of Na transfer from sample to tip [26]. Here the transfer process was described in terms of a field-induced bonding between the Na atom and the tip.

Recently, two additional explanations have been proposed. Sáenz and García treated the Xe-atom transfer in the experiment by Eigler *et al.* as a tunneling phenomenon [27], while the Nottingham effect was suggested by Gratzke and Simon to be responsible for the mound formation in voltage-pulse experiments on Au [28]. In the latter case, a positive or negative energy is released to the apex of the cathode (tip), depending on the difference between the Fermi level and the energy of field-emitted electrons.

For fixed conditions, this effect tends to stabilize the temperature at a value that may be higher than the melting point, causing a liquid neck to be formed between tip and surface. Gratzke and Simon also pointed out that thermal expansion of the tip could play a role in the formation of a contact.

When turning to the other two categories of experiments, a major uncertainty can be left out, as contact formation no longer is a question but rather a fact. In these studies, the so-called jump to contact is usually attributed to the adhesive avalanche predicted by Pethica and Oliver in 1987 [29] and later confirmed in other theoretical studies [30–38]. Irrespective of the rigidity of the SPM, an avalanche will occur within a very short time scale ( $\approx 1$  ps according to Ref. [32]) at an electrode separation smaller than  $\approx 1$ – $2$  Å. In a simple continuum model, this will happen whenever the tip-surface interaction-force gradient  $\nabla F^{int}$  surpasses the total rigidity of the system  $\partial F^{def}/\partial h$ . Here  $F^{def}$  denotes the deformation force needed in order to cause a change  $h$  in the gap width<sup>3</sup>.

The first experiment, in which the tip has been driven purposely into contact with the sample, was reported in 1986 by Abraham *et al.* [3]. Here the intention was to modify a Au surface with the tip, and from a change in topography and a junction resistance of  $200 \Omega$ , it could be inferred that electrical and mechanical contact indeed had been created. A year later, Gimzewski and Möller studied the transition from tunneling to contact in further detail [39]. They found an abrupt change in current when the tip was advanced more than  $4$  Å towards the sample from the initial tunneling position. As the resistance then reached a value of  $\approx 10$  k $\Omega$ , the current jump was attributed to the formation of a single-atom contact. Similar results were obtained in other STM studies [40–44] as well as in mechanically controllable break-junction experiments [45–48]. This effect was directly used by Smith to demonstrate a quantum point contact switch [49]. Here it is interesting to note that for all low-temperature experiments (less than  $10$  K), the resistance immediately after the jump to contact attained a value corresponding to a single-atom contact, as calculated by Lang [50]. This is not true for all room-temperature experiments as Muller *et al.* [47] and Stalder and Dürig [44] observed contact resistances of  $\approx 100 \Omega$  and  $\approx 1$  k $\Omega$ , respectively, corresponding to contact diameters of  $\sim 10$ – $30$  Å.

As already mentioned, the latter group of experiments is characteristic in the sense that a contact is formed spontaneously, i.e., without any

---

<sup>3</sup>Both  $\vec{F}^{int}$  and  $\vec{F}^{def}$  are directed along the  $z$  direction as axial symmetry around the tip is assumed.

apparent change in the tunneling parameters. These experiments were done by Kuipers *et al.* on (110) and (111) facets of a Pb single crystal [51,52]. At room temperature, normal scanning was possible over extended periods of time ( $I = 2$  nA,  $V_b = -5$  V on sample). However, if the temperature was increased slightly, a short circuit resulted after some time of scanning. For temperatures above 350 K, no tunnel current could be detected prior to a short circuit. Kuipers *et al.* therefore estimated that the jump distance could be as long as 8 Å or more, implying long-range forces. Moreover, as the frequency of short circuits increased when the electric field was reduced by decreasing  $V_b$  at a constant  $I$ , electrostatic forces were excluded as a possible explanation for the jumps. Instead, the van der Waals forces and adatom diffusion on the surface were suggested to be the responsible mechanisms.

Most recently, Sørensen *et al.* have proposed a new, thermally activated mechanism for the contact-formation process at elevated temperatures (e.g. RT) [53]. In this study, molecular-dynamics simulations were performed for a Au tip-surface model system in order to identify stable, intermediate atomic configurations and migration processes that can lead to a tip-surface contact. Based on these simulations, it was found that energy barriers for migration processes on the tip are lowered significantly by the proximity of the surface. Sørensen *et al.* therefore suggest a “diffusion-to-contact” scenario in which a sequence of individual jumps of atoms from the tip towards the surface lead to a contact. Despite a resemblance to the proposal of Kuipers *et al.*, it is not the same mechanism as no effect of long-range forces is included here. Evidently, the diffusion to contact also deviates from adhesive avalanche in several ways, and the dissimilarities should make possible an experimental distinction. Characteristic for this thermally activated diffusion-to-contact process compared to adhesive avalanche is the onset at a larger gap width (up to 5 Å compared to 1–2 Å) and a much longer time scale (milliseconds compared to picoseconds).

### 5.3 Experimental Results

Figure 5.1 shows three examples of the region where the conductance  $G(z)$  starts to deviate from an exponential increase in the ingoing part of indentation curves for Ni(111), Pt(100), and Au(110), respectively. The transition is characterized by a sudden orders-of-magnitude jump in  $G(z)$  within a tip displacement of less than 0.5 Å — a behavior which is not

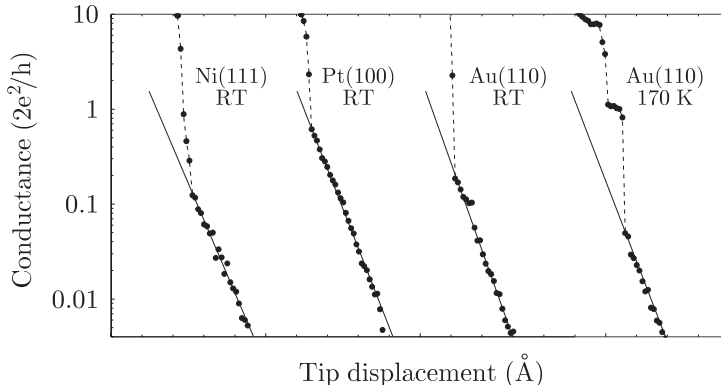


Figure 5.1: Conductance data from indentations on Ni(111), Pt(100), and Au(110), showing the transition from an exponential increase to a faster-than-exponential behavior during tip approach. The three leftmost curves represent RT data, while the right-hand curve has been measured at 170 K. In all cases, the indentation speed and magnitude of the bias voltage were fixed at values lying in the ranges 310–350 Å/s and 4.4–4.9 mV, respectively. For clarity, the curves have been separated along the horizontal axis which measures the relative displacement between data points belonging to the same indentation.

consistent with tunneling. For all three materials, this predominantly happens at a conductance  $G_{jump}$  between 0.1 and 1 quantum unit ( $\sim 100$  k $\Omega$  to  $\sim 10$  k $\Omega$ ) although, occasionally, lower values are also observed. A general trend for  $G_{jump}$  is hard to establish as the values do not reproduce very well from one series of measurement to the other. For instance, based on more than 300 individual measurements on Au(110) at RT, with an indentation speed of  $360 \pm 20$  Å/s and  $|V_b^i| = 4.8 \pm 0.2$  mV,  $G_{jump}$  was found to be  $0.16 \pm 0.02$  quantum unit. Later, using the same set of parameters, this experiment was repeated, resulting in a new value of  $G_{jump} = 0.47 \pm 0.02$  quantum unit. Such discrepancies must be caused by variation in experimental conditions that are not subject to a direct control, and it is therefore believed that the geometry/structure of the tip plays a major role for the onset of the conductance jump.

Once a jump is initiated,  $G$  does not settle at a value corresponding to a one-atom contact, as reported by Gimzewski and Möller [39]. Rather, it continues to increase by two orders of magnitude, typically, reaching values between 10 and 100 quantum units ( $\sim 1$  k $\Omega$  to  $\sim 100$   $\Omega$ ). However,

at 170 K, a few exceptions have been observed, as illustrated by the last curve in Fig. 5.1. Here the conductance jumps to a value very close to one quantum unit where it stays fairly constant as the tip is advanced more than 0.5 Å. Then another jump of approximately seven quantum units occurs, after which a more moderate increase takes over. Consequently, the duration of the total conductance-jump sequence is to be measured in milliseconds. The RT data display a faster increase when the conductance starts to deviate from the tunneling behavior. However, in general it is not very much faster. As shown on page 148 in appendix A, the response time of the electronics at a sampling period of 270  $\mu\text{s}$  per data point corresponds to approximately two data points. The response time can therefore not explain the number of data points measured during the conductance jump for the first two curves in Fig. 5.1. In other words, at RT the process takes place on a microsecond-to-millisecond time scale.

The jump in  $G$  is always found to be correlated with mound formation and a significant hysteresis in the conductance curve. On the other hand, if no jump is observed, then  $G(z)$  is reversible and, as judged from topographic images, no modification of the surface has taken place. An example will illustrate these points. In Fig. 5.2 are shown two successive constant-current images of the same  $180 \times 250 \text{ \AA}^2$  area on Au(110) recorded at 170 K with a time separation of 9 s. During the acquisition of each image, four indentations (1–4 and 5–8, respectively) have been made at the locations marked with arrows. In order to appreciate Fig. 5.2, it is important to notice the direction of raster scanning as shown in Fig. 1.1(b) on page 11, i.e., from left to right and from bottom to top. Consequently, Fig. 5.2(a) was recorded in the following way: First the bottom part of the image was scanned as usual. As soon as the tip reached point 1 from the left, scanning was stopped and the feed-back loop opened. Then the first indentation was made by moving the tip in the direction normal to the surface ( $z$  direction), as described in chapter 3. After completion of the indentation, which took roughly 140 ms, tunneling was re-established and the feed-back loop closed before raster scanning continued towards point 2. Here the entire sequence was repeated: opening loop, indenting, resuming tunneling, closing loop, scanning towards point 3, and so forth<sup>4</sup>. This description also holds for indentations 5–8 in Fig. 5.2(b). As a consequence of the recording procedure, the part of an image lying *below/above* one of the marked points represents the surface topography *before/after* the

---

<sup>4</sup>In practice, an indentation is performed by pointing and clicking with the mouse during image acquisition. This facilitates the selection of a new, clean spot on the surface for each indentation.

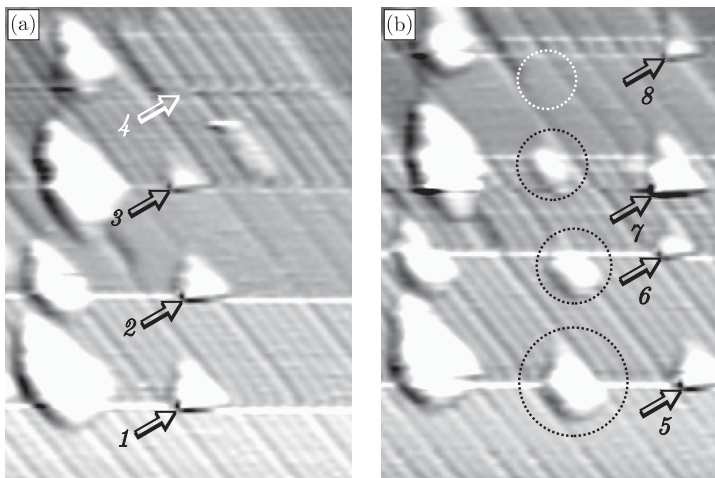


Figure 5.2: Successive  $180 \times 250 \text{ \AA}^2$  constant-current images of Au(110) recorded at 170 K with a time separation of 9 s and parameters  $I = 1.7 \text{ nA}$  and  $V_b = 37 \text{ mV}$ . A total of eight indentations [1–4 in (a) and 5–8 in (b)] have been made during acquisition of the images at the positions marked with arrows. The circles in (b) encompass the locations of the indentations 1–4 in (a). See text for further details!

corresponding indentation.

As immediately apparent from Fig. 5.2, four hillocks are lying on top of the surface on the left-hand side of the images. These are the results of four previous indentations, and here they serve as reference points, confirming that (a) and (b) are indeed topographic images of the same surface area. The  $(1 \times 2)/(1 \times 3)$  reconstruction of Au(110) is also visible as rows running diagonally across the images, implying a resolution of  $\approx 8 \text{ \AA}$ . What may seem very surprising is that the indentations do not spoil the resolution, although small changes in the contrast are observed as well as slight shifts ( $\leq 1 \text{ \AA}$ ) of the substrate level. The latter can be explained as a decrease in tip length, causing the terrace to appear lower<sup>5</sup>. Even more astonishing than the preservation of resolution is the lack of lateral shifts in the images. Between the  $(1 \times 2)$  patches are seen single  $(1 \times 3)$  periods running throughout the images without any kind of discontinuity. This means that

<sup>5</sup>A decrease in tip length is not universal as indentations occasionally give rise to a lengthening of the tip.

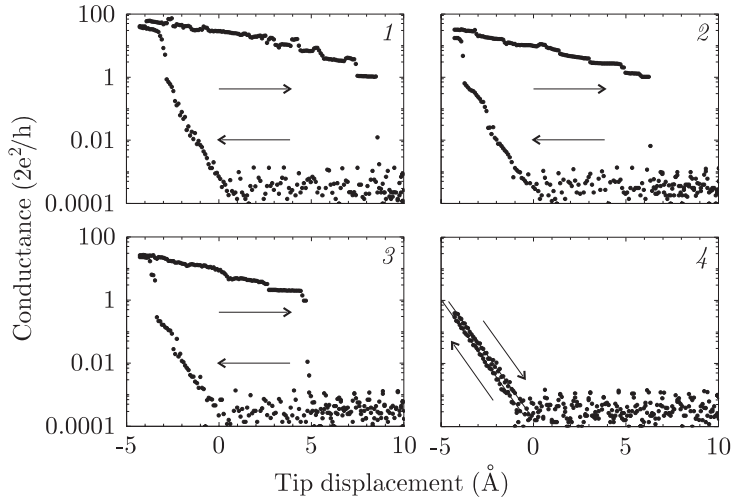


Figure 5.3: Measured conductance corresponding to the four indentations made during acquisition of the image in Fig. 5.2(a). The indentation speed was  $335 \text{ \AA/s}$ . A discussion of the curves is given in the text.

not only can the tip sustain indentations without a severe degradation, the location of the most protruding part of the tip is also preserved within a few ångströms.

By inspecting Fig. 5.2(a), it is evident that the first three indentations produced a mound on the surface, while indentation 4 apparently did not. This is confirmed in (b) where circles encompass the positions indicated in (a). In the three black circles is seen a protrusion with a volume in the range  $700\text{--}2500 \text{ \AA}^3$ , whereas the white circle reveals an ostensibly unperturbed surface.

Comparing these observations with the conductance curves measured during indentations 1–4 (Fig. 5.3) leads to several general conclusions: When  $G(z)$  exhibits a sudden jump in the exponential regime during tip approach (1–3), a mound is formed on the surface and *vice versa*. In the same circumstances,  $G$  attains values of orders of magnitude larger than what can be explained as a tunneling phenomenon — a situation which even remains after a tip withdrawal of several ångströms, which gives rise to a considerable hysteresis in  $G(z)$ . If, however, no jump is observed (4), then  $G(z)$  decreases exponentially during tip retreat, that is,  $G(z)$  is

reversible, and no mound is detected<sup>6</sup>.

These results suggest that the conductance jump is associated with considerable atomic motion and adhesion between tip and sample, that is, contact formation. However, despite the fact that exactly the same set of parameters has been used for all the indentations 1–8, and the tip effectively is left undisturbed, as argued above, a contact is only formed in seven out of the eight indentations. It is therefore evident that the process, under unchanged conditions, is governed by some probability which, in the present case, is less than one. A natural question then arises: If the tip is kept at a fixed position very close to the surface, will a contact then develop spontaneously, in analogy with the results reported by Frenken *et al.* [51,52]? In order to answer this question, measurements of the conductance as a function of time were made. An example for Au(110) at 170 K is shown in Fig. 5.4.

Figure 5.4 is divided into three sections illustrating the sequence in which the measurements were made. First, the tip was moved towards the surface at a constant speed of 310 Å/s in the usual way. In the tunneling regime, the conductance increased exponentially as a function of  $z$  (left-most part of figure). Before a contact was formed, the direction of motion was reversed ( $z_{min} = -2.8$  Å), leading to an exponential decrease in  $G$  corresponding to the behavior of curve 4 in Fig. 5.3. After a total retraction of 0.6 Å from the deepest point of indentation, the tip movement was stopped by freezing  $V_z$ . Conductance measurements did not stop, however, and at a fixed tip position,  $G$  was recorded at a regular time interval of 320  $\mu$ s. These data are shown in the middle section of Fig. 5.4, while the last section displays the conductance evolution during the final separation of tip and surface.

During the first  $\approx 100$  ms of the time sequence in Fig. 5.4,  $G$  stays well below the conductance of 0.5 quantum unit measured at the most protruding tip position. So even though a small change in gap width cannot be totally ruled out<sup>7</sup>, it is clear that the tip-surface separation does not decrease to the value it reached at the deepest point of indentation. The contact that develops during the subsequent time period of  $\approx 20$  ms can therefore not be caused solely as a consequence of the proximity of tip

---

<sup>6</sup>From a careful inspection of curve 4 in Fig. 5.3, it is obvious that a small hysteresis of  $\approx 0.3$ – $0.4$  Å is present also in this case. This is an artifact of the measurement itself rather than being a real effect. It is caused by a measurable time lag between the software-dictated motion of the tip and the  $V_z$  voltage that drives the scanner tube. As shown on page 148 in appendix A, this delay in  $V_z$  corresponds to a hysteresis of  $0.4 \pm 0.1$  Å at a speed of 295 Å/s.

<sup>7</sup>A change in gap width may arise as a consequence of thermal drift.

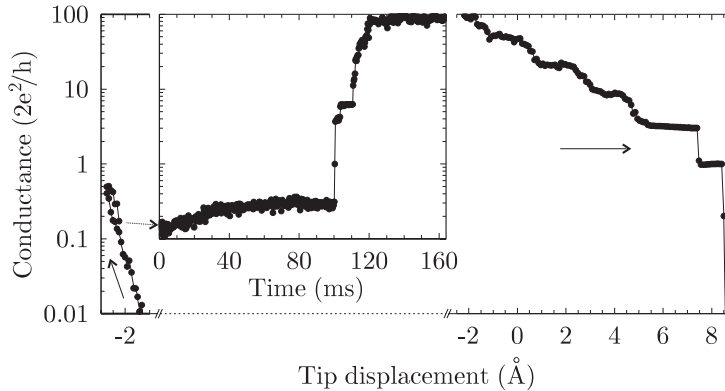


Figure 5.4: Conductance *versus* tip displacement and time (at a fixed tip position) at 170 K and  $V_b^i = 4.6$  mV. In the leftmost part of the plot, the exponential increase in the tunneling conductance is shown as the tip is moved towards the surface at a speed of  $310 \text{ \AA/s}$ . It reaches a maximum value of  $\approx 0.5$  quantum unit at  $z = -2.8 \text{ \AA}$  before the direction of motion is reversed. At  $z = -2.2 \text{ \AA}$ , the movement is stopped, and  $V_z$  is then kept at a fixed value during a time period of 163 ms. Meanwhile, at a time interval of  $320 \mu\text{s}$ , the conductance is measured, and the result is shown in the middle part of the plot. The conductance during the final separation of tip and surface is shown in the rightmost section.

and surface as in the adhesive avalanche.

Similar results have been obtained at RT, although the time period spent in the tunneling regime before the formation of a contact in general is smaller (typically  $\sim 10$  ms)<sup>8</sup>. As discussed in connection with Fig. 5.1, the temperature thus seems to play a role, suggesting that thermally activated processes may be important. This is further supported by yet another observation.

In Fig. 5.5 is shown a conductance curve for Au(110) measured at RT. A characteristic feature of this indentation is the presence of two conductance jumps during tip approach. The second jump is in all respects analogous to what has previously been described, whereas the first jump is different. It occurs entirely within the tunneling regime, excluding a direct

<sup>8</sup>These experiments are not very reproducible, and the comments made on page 78 in connection with measurements of  $G_{jump}$  therefore also apply here. However, it is indeed observed that the success rate (counting the number of indentations where a contact actually is formed within the time sequence) is higher at RT compared to 170 K.

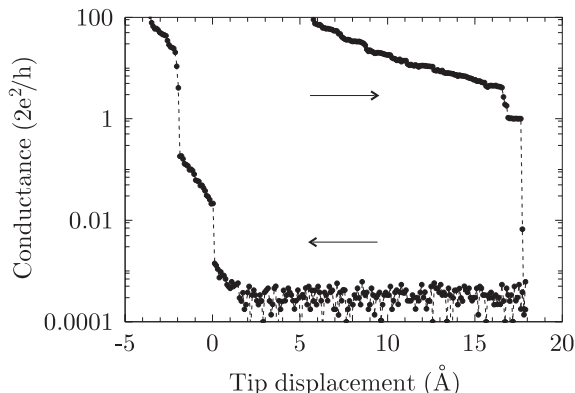


Figure 5.5: Conductance curve for Au(110) measured at RT with an indentation speed of  $330 \text{ \AA/s}$  and a bias voltage of  $5.1 \text{ mV}$ . As the tip advances towards the surface, a jump in  $G$  is observed in the tunneling regime. Such a “prejump” cannot be correlated with contact formation. See text for further details!

connection with contact formation processes. However, as the jump can only be explained as a consequence of a change in the effective gap width and/or tunneling area, this “prejump” must be associated with atomic motion in the junction, providing evidence for a fairly long-range interaction. Furthermore, the frequency with which prejumps are observed depends strongly on temperature. Based on more than 350 individual indentations at RT, it was found that prejumps occurred in approximately 70% of the incidents. From a similar number of measurements at 170 K, the same figure was determined to be below 10%<sup>9</sup>.

## 5.4 Discussion

As a starting point for the discussion, it can be noted that transfer processes do not take place in the experiments described above. This can be inferred from the experimental fact that mound formation is never observed without an accompanying high conductance level and hysteresis characteristic for a tip-surface contact. Atomic tunneling and field evaporation can therefore immediately be ruled out as possible candidates for

<sup>9</sup>No comparison to high temperature measurements has been made, since the jump frequency at 390 K probably is too high to resolve single prejumps within a sample period as discussed on page 61.

an underlying mechanism. Nevertheless, this does not *a priori* exclude any influence by the electrical field. In order to get a feeling for the magnitude of the field, an upper limit on the field strength could be evaluated if the minimum gap width was known. Unfortunately, this is not the case. However, from molecular-dynamics simulations, the jump distance in an adhesive avalanche process for a Ni/Au tip-sample system at 300 K was found to be approximately 2 Å [32]. A gap width of 1 Å should therefore be well below the accessible range, making it suitable as a lower limit. From the applied bias voltage, which in all indentation measurements carried out has been lower than 6 mV, the resulting upper limit on the field becomes<sup>10</sup> 6 mV/Å. This is roughly two orders of magnitude lower than the threshold fields for mound and/or pit formation found in voltage-pulse experiments [5,13,18] as well as two orders of magnitude lower than the estimated critical field for the Nottingham effect [28]. It is therefore reasonable to assume that the electrical field only plays a minor role, if any at all, in these experiments.

From a theoretical point of view, the adhesive avalanche seems to be a well established effect occurring at gap widths smaller than 1–2 Å [30–38]. Indeed, the contact-formation process has been interpreted as an adhesive phenomenon in experimental studies performed both at cryogenic temperatures [41–43,45,46] and at RT [39,40,44]. However, even though adhesion, by definition, is present when a contact has been formed, the question is whether adhesion is the *cause* of the contact. Several properties of the data presented in the previous section indicate that other processes are involved. For instance, the gap width, at which the conductance jump occurs, varies with more than 1 Å at unchanged conditions, as evident from Fig. 5.3. Since the attractive tip-surface-force gradient should reproduce at a given gap width in the ingoing part of an indentation, this is not consistent with adhesive avalanche. Here an objection could be made, as indentations 1–4 are located at different positions on the surface, and minor tip changes cannot be ruled out, which may imply a non-reproducible behavior of the force curve. More convincing is the fact that a contact can form spontaneously, as shown in Fig. 5.4. Here it is most important to recognize that the gap width, at which the conductance jump occurs, certainly is *larger* than it was at the deepest point of indentation where no jump was observed. Adhesive avalanche can therefore not explain the behavior seen in Fig. 5.4. Furthermore, as already mentioned in the previous section, the time scale of a conductance jump in the experiments is in

---

<sup>10</sup>This limit is certainly an upper limit as the voltage across the junction decreases below the bias voltage  $V_b^*$  at low gap resistances.

general microseconds to milliseconds, in sharp contrast to the picosecond time scale found in molecular-dynamics simulations of adhesive avalanche [32].

A much better agreement between experiment and theory is obtained by comparing the data with the diffusion-to-contact model proposed by Sørensen *et al.* [53]. The speed of contact formation in this model is controlled by the speed of the individual migration processes on the tip, that is, by Boltzmann factors  $\exp(E_a/k_B T)$ , where  $E_a$  is the activation energy and  $T$  is the absolute temperature. So, unlike the adhesive avalanche process, which in principle only depends on the tip-sample separation (for a static system), the diffusion to contact is governed by a probability per unit time which is a function of temperature. In this way, spontaneous contact formation as well as the temperature dependence of the preceding time period spent in the tunneling regime (Fig. 5.4) can be explained. Furthermore, Sørensen *et al.* find that the activation energies involved result in a process which at RT takes place on a millisecond time scale, in agreement with the experimental observations. At lower temperatures, the diffusion rate is smaller according to the Boltzmann factor, and consequently, a diffusion-to-contact mechanism would be more slow. Indeed, this is very likely to explain why plateaus in the ingoing conductance curve only are observed in measurements at 170 K (Fig. 5.1). Moreover, prejumps in the tunneling regime are bound to be caused by atomic rearrangements in the junction, and since the probability for prejumps depends on temperature, these can be well described as initial migration processes towards a contact. Finally, it can be noted that, according to Sørensen *et al.*, at RT, diffusion to contact sets in at a larger gap width, and therefore at an earlier stage of indentation, than avalanche adhesion. This may be the reason why the faster-than-exponential increase in the conductance just before contact formation is observed at 4 K and not at RT, as described on page 61 in chapter 4. Based on the experiments carried out, it can thus be concluded that the diffusion scenario, proposed by Sørensen *et al.*, is the most reasonable explanation for the contact-formation process at elevated temperatures.

## 5.5 Polarity Dependent Contact Formation

In a set of experiments, the polarity of  $V_b^i$  was changed for every fourth indentation, and, quite surprising, this was found to have a drastic influence on the conductance level at which contact formation initiates ( $G_{jump}$ ).

The results from indentations on Ni, Cu, and Au<sup>11</sup> are shown in Table 5.1. As noted in section 5.3, a direct comparison between different experiments is not possible, presumably due to variations in the structure and/or geometry of the tip. Nevertheless, since the sign of  $V_b^i$  has been changed regularly throughout the measurements, a polarity-dependent contrast in  $G_{jump}$  should reflect a real physical property of the system.

Table 5.1 shows that in all cases, except for Au at 390 K,  $G_{jump}$  is highest at positive polarity<sup>12</sup>. Moreover, the onset of contact formation

Table 5.1: Average values for  $G_{jump}$  measured on Ni(111), Cu(100), and Au(110) for both polarities at three different temperatures. Each value is based on more than 150 indentations, all recorded at a bias voltage less than 5 mV and with an indentation speed in the range 300–400 Å/s. Only absolute numbers within the same row and column (same material and temperature) can be compared directly. Further details are discussed in the text.

Temperature	Polarity	Ni	Cu	Au
170 K	Negative	—	$0.32 \pm 0.03$	$0.12 \pm 0.01$
	Positive	—	$0.75 \pm 0.05$	$0.31 \pm 0.02$
270 K	Negative	$0.18 \pm 0.01$	$0.20 \pm 0.01$	$0.38 \pm 0.03$
	Positive	$0.53 \pm 0.05$	$2.22 \pm 0.08$	$0.55 \pm 0.04$
390 K	Negative	—	$0.37 \pm 0.01$	$1.24 \pm 0.08$
	Positive	—	$1.17 \pm 0.05$	$0.94 \pm 0.05$

takes place at a conductance less than one quantum unit, as expected, if two values for Cu and one for Au are disregarded. These observations induce two important questions: What is the origin of the polarity dependence, and how can a tunneling conductance of 2.2 quantum units be explained? To investigate this in further detail, a series of experiments was initiated. Since Cu demonstrates the most prominent effects, as seen in Table 5.1, this was the choice of tip-sample material.

Figure 5.6 shows a manifestation of the difference between positive and negative polarity. Two indentations have been made with a time separation of less than 20 s and at the same parameters, apart from a sign change on  $V_b^i$ . In the first part of the tunneling regime, the conductance

<sup>11</sup>These experiments have not yet been carried out for Pt, and only RT data for Ni are available.

<sup>12</sup>The bias voltage is applied to the sample, and at positive polarity, the electrons therefore transfer *from tip to sample*, and *vice versa*.

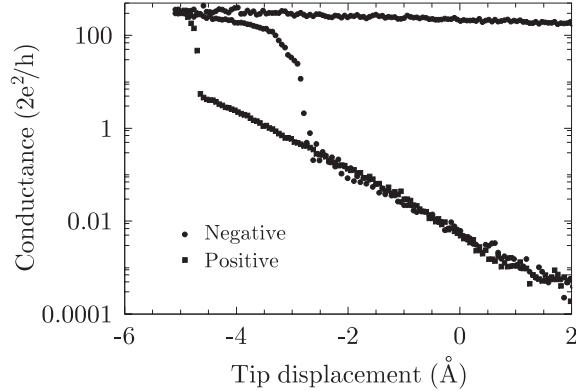


Figure 5.6: Conductance measured during indentation of a Cu tip into a Cu(100) surface at RT. The two curves have been recorded with a time separation of less than 20 s and at the same parameters ( $V_b^i = 4.8 \pm 0.1$  mV, speed  $\approx 210$  Å/s), apart from a change of polarity.

is independent of polarity. However, at negative  $V_b^i$ , a contact is formed at  $z = -2.7$  Å. From this point of indentation, the tip can be moved 2 Å further towards the surface, at positive polarity, before a contact develops. Most remarkable, in this region,  $G(z)$  continues to increase exponentially at the same rate, and  $G_{jump}$  reaches a value as high as 5.6 quantum units. Still though, the jump in  $G$  is correlated with conductance hysteresis and mound formation, that is, if the direction of motion is reversed before the conductance jump sets in, then  $G(z)$  is found to be reversible.

Results as those shown in Fig. 5.6 are not exceptional examples, rather they represent typical behavior at RT, as also indicated in Table 5.1. This is seen in Fig. 5.7. Here the depth of indentation has been varied, that is, for a number of fixed values of  $z_{min}$ , the tip has been indented more than 40 times for each polarity (again, changing sign on  $V_b^i$  for every fourth indentation). A single data point is thus an average value based on many individual indentations. Figure 5.7(a) displays average values for the conductance at  $z = z_{min}$  for those indentations that did not result in a contact. The first point to be noticed is that for both polarities,  $G(z_{min})$  increases exponentially as  $z_{min}$  decreases, and, taking the error bars into account, the rate of increase is almost the same. However, for  $z_{min} < -3.2$  Å at negative  $V_b^i$ , contact formation is found in every indentation, whereas, for positive polarity, there are still examples at  $z_{min} < -4.5$  Å that do not

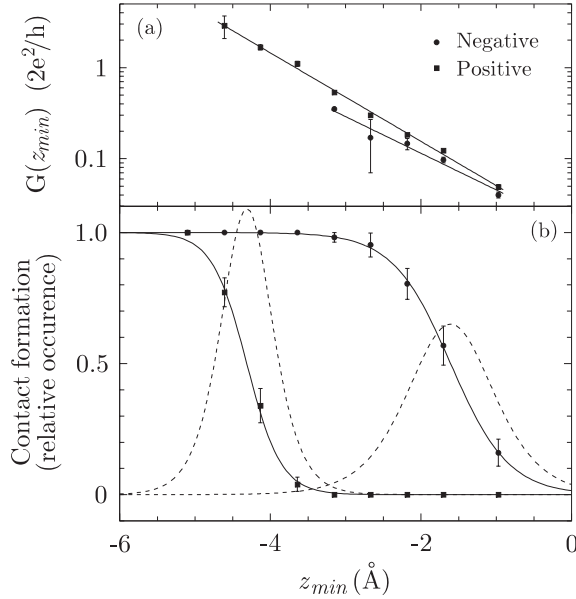


Figure 5.7: RT data from more than 40 indentations at each polarity and depth. In (a) is shown average values of  $G(z_{min})$  for those indentations that did not result in a contact. The relative occurrence of contact formation is plotted in (b) together with fitted curves of the form given in Eq. (5.1) (solid lines). Also depicted are the absolute values of the derivatives (dashed lines) which have peaks lying at  $z_{min} = -4.3 \pm 0.1 \text{ \AA}$  (positive  $V_b^i$ ) and  $z_{min} = -1.6 \pm 0.2 \text{ \AA}$  (negative  $V_b^i$ ).

lead to a contact, even though the conductance reaches values well above one quantum unit, an order of magnitude higher than observed for negative  $V_b^i$ .

The relative occurrence of, or probability for, contact formation is shown in Fig. 5.7(b) along with Fermi-Dirac-like functions,

$$y = \frac{1}{1 + \exp[\alpha + \beta(z_{min} - z_0)]}, \quad (5.1)$$

fitted to the data points (solid lines) and the corresponding derivatives (dashed lines). As the integrated area below each dashed curve is equal to one, the infinitesimal area below these curves at any given depth represent the probability for contact formation. From the positions of the peaks, it

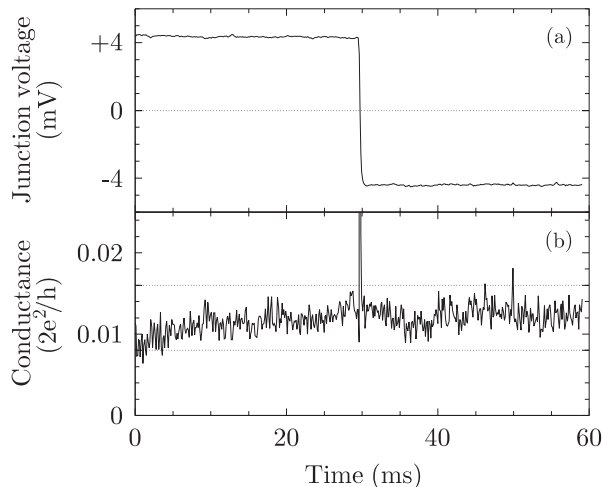


Figure 5.8: At a fixed tip-sample distance (fixed  $V_z$ ), the conductance was measured as a function of time (b). After a time period of 30 ms, the polarity was switched, as revealed in the measured junction voltage shown in (a). This did not affect the tunneling conductance, as it stayed within the range of 0.008–0.016 quantum units throughout the entire time period of 60 ms.

is confirmed that contact formation at positive polarity happens at a much later stage of indentation than at negative polarity — the difference in  $z$  is found to be  $2.7 \pm 0.3 \text{ \AA}$ .

Since these results were rather unexpected, much effort was used to rule out any experimental errors. The conductance measurement was double-checked by calibrating both before and after the experiments, as described on page 154 in appendix B. Essentially no drift in the measurements was found. Likewise, it was verified that the absolute value of  $V_b^i$  stayed within  $4.7 \pm 0.1 \text{ mV}$  throughout the experiments. Finally, it was tested whether a change in polarity could cause a shift of the  $z$  scale. Since the origin of the  $z$  scale is defined as the initial tunneling position before the feedback loop is opened (see page 41 in chapter 3), such a discrepancy would occur only if the tunneling conductance was polarity-dependent. This is not the case, as shown in Fig. 5.8. For a fixed tip-sample distance, no change in conductance was observed when the sign of  $V_b^i$  was changed. Consequently, the polarity effect in contact formation does not seem to be an artifact.

In section 5.4, it was argued that the electrical field in these expe-

periments is too small to be expected to have a major impact on contact formation. This does not leave many possibilities for a responsible candidate, and the focus was thus aimed towards the magnitude of the current. Even though the total tunneling current is very small, the density reaches extreme values (of the order  $10 \text{ nA}/\text{\AA}^2$  or, equivalently,  $10^6 \text{ A}/\text{mm}^2$ ), and an influence of the current is therefore plausible. As described in section A.1 in appendix A, the maximum current in the indentations can be changed by changing the input impedance of the preamplifier which, in turn, is done by changing the feedback resistor shown in Fig. A.1 on page 146. In this way, the input impedance was changed from  $11 \text{ k}\Omega$  to  $116 \text{ k}\Omega$ . At large junction resistances, the current is not affected very much, but at a conductance of one quantum unit, the current will be reduced by roughly a factor of five (see Fig. A.2 in appendix A).

Figure 5.9 shows the results from an experiment where all parameters, apart from the reduced current, were unchanged (compare with Fig. 5.7). As immediately apparent from the data points in (a) and the relative peak positions in (b), the polarity effect has now disappeared<sup>13</sup>. A comparison of Figs. 5.9(a) and 5.7(a) indicates that this has happened, not because contact formation occurs at a lower conductance level for positive polarity, but rather because the junction can withstand higher conductances at negative polarity without forming a contact. Since  $G_{jump}$  usually is found to be below one quantum unit (see Table 5.1), this behavior may seem surprising, however, it does confirm that the current plays a significant role in the contact-formation process.

Encouraged by these findings, it was decided to carry out similar experiments at  $170 \text{ K}$  and  $390 \text{ K}$ . From the corresponding results, shown in Figs. 5.10 and 5.11, it is again confirmed that contact formation depends strongly on polarity. However, in contrast to the RT experiments, the relative peak positions in (b) and (d) are not affected by a reduction of the current neither at  $170 \text{ K}$  nor at  $390 \text{ K}$ . In all cases, the peaks are displaced by an amount which is lying in the range  $1.1\text{--}1.4 \pm 0.4 \text{ \AA}$ , that is, significantly lower than the  $2.7 \pm 0.3 \text{ \AA}$  found at RT. Furthermore, it can be inferred from (a) in both figures that, at high current and positive polarity,  $G_{jump}$  does not attain values much higher than one quantum unit, in agreement with Table 5.1. This is also true at low current (c), where  $G(z_{min})$  shows a tendency for saturation, i.e., it deviates from an exponential function for small  $z$ . For negative polarity,  $G(z_{min})$  stays far

---

<sup>13</sup>Since the tunneling position determines the origin of the  $z$  scale, it may not be the same from one experiment to another. Consequently, only relative changes in peak positions can be compared.

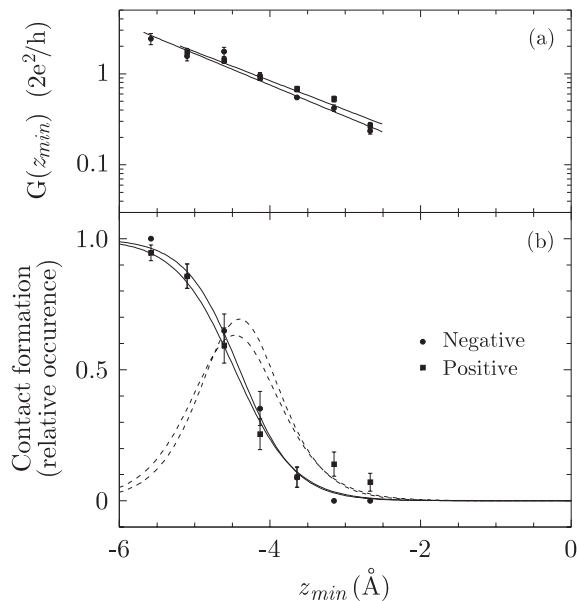


Figure 5.9: Apart from a change in input impedance of the current preamplifier ( $11\text{ k}\Omega \rightarrow 116\text{ k}\Omega$ ), causing a reduction of the current, the data presented in this figure have been acquired in the same way and at the same conditions as the data shown in Fig. 5.7 (see the corresponding caption details). The positions of the peaks in (b) are  $-4.5 \pm 0.2\text{ \AA}$  and  $-4.4 \pm 0.2\text{ \AA}$  for positive and negative polarity, respectively.

below one quantum unit, also at low currents, which again is different from the behavior at RT.

## 5.6 Discussion of Polarity Effects

The experimental results presented in section 5.5 further support the previous conclusion that adhesive avalanche cannot explain the observed behavior — current-dependent effects are bound to be of importance, at least at RT. Since the diffusion-to-contact scenario was favored in section 5.4 as the most promising explanation for contact formation, it is an important question whether this model is consistent with a polarity dependence. Apparently, it would require a current-induced directional diffusion, that is,

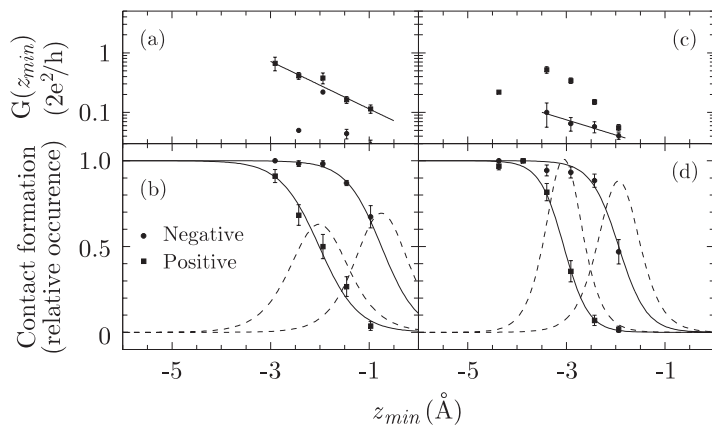


Figure 5.10: Data from measurements carried out at 170 K. High-current data are shown in (a) and (b), while low-current data are shown in (c) and (d). Refer to the caption of Fig. 5.7 for further explanation. The peak positions are, in (b),  $-2.0 \pm 0.2 \text{ \AA}$  (positive) and  $-0.8 \pm 0.3 \text{ \AA}$  (negative), and in (d),  $-3.0 \pm 0.1 \text{ \AA}$  (positive) and  $-1.9 \pm 0.1 \text{ \AA}$  (negative).

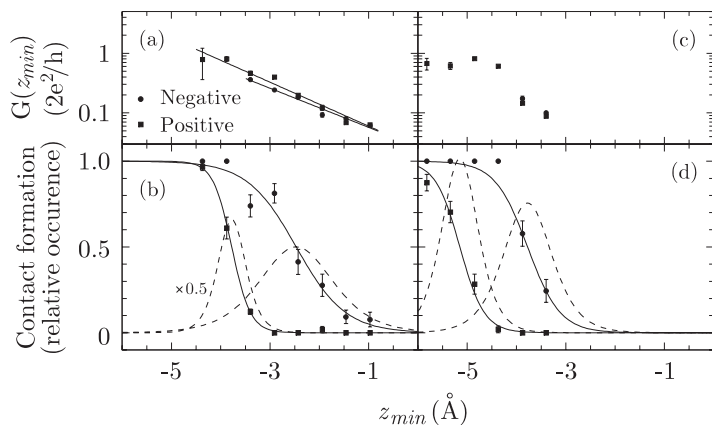


Figure 5.11: Data from measurements carried out at 390 K. High-current data are shown in (a) and (b), while low-current data are shown in (c) and (d). Refer to the caption of Fig. 5.7 for further explanation. The peak positions are, in (b),  $-3.8 \pm 0.1 \text{ \AA}$  (positive) and  $-2.5 \pm 0.2 \text{ \AA}$  (negative), and in (d),  $-5.2 \pm 0.2 \text{ \AA}$  (positive) and  $-3.8 \pm 0.2 \text{ \AA}$  (negative).

electromigration. However, in order not to precipitate a conclusion, it is worthwhile to discuss the results in greater detail.

From a comparison of Figs. 5.10 and 5.11, it is revealed that there is essentially no difference between the results obtained at 170 K and 390 K. The RT results are in sharp contrast to these in three ways: The polarity effect depends on current, conductances well above one quantum unit can be reached without contact formation, and finally, at high current, the polarity effect is much larger than observed at other temperatures. A tempting explanation for these discrepancies, especially since RT is lying in the middle of the temperature range, would be that the RT results were wrong for some experimental reason. However, this is very unlikely, as the same deviation is seen Table 5.1 which is based on a completely different set of data. So why is RT a special temperature? A possible explanation could be that two temperature effects are in play, pulling in opposite directions, and that the same results are obtained at 170 K and 390 K only by chance. This would, of course, not make easier an interpretation on basis of the present data set.

Now, focusing on Figs. 5.6 and 5.7, there are essentially two unusual and challenging observations to be explained, namely tunneling conductances as high as five quantum units, and the  $z$  difference between contact formation at positive and negative  $V_b^i$ . Concerning the latter point, it is clear that either the tip is in mechanical contact with the surface before an electrical contact is established at positive polarity, or contact formation is initiated at a tip-sample distance larger than three ångströms at negative polarity. If tip and sample were in mechanical but not electrical contact, it would imply an insulating layer between tip and surface. This is not very plausible, as each indentation is located at a new, clean spot of the crystal. Of course, foreign atoms could be present on the tip, however, it is hard to believe that they would be able to withstand several hundred indentations and contacts during an experiment. Consequently, these considerations implies that contact formation takes place at a large tip-surface distance at negative polarity, which further supports the diffusion-to-contact scenario [53]. On the other hand, it is far from clear how a tunneling conductance can be as high as five quantum units unless the gap width is vanishing, and the effective tunneling area is tremendous<sup>14</sup>.

This discussion leaves more open questions than answers, and further experiments are needed in order to identify the underlying physical mechanisms. However, the results show with no doubt that contact formation

---

<sup>14</sup>In chapter 6 it will be shown that the conductance of the smallest metallic contacts is close to one quantum unit. This is in agreement with theoretical calculations [50,54].

indeed does depend on the direction of the current. According to the author's knowledge, such an effect has not been reported before.

Finally, it should be emphasized that a polycrystalline Cu tip with a purity of 99.9% was used in these experiments. This has the consequence that the two electrodes, tip and sample, only differ in geometry and internal structure. If the two electrodes were equal the polarity effect could not be present due to symmetry, and a proper model therefore has to include geometrical and/or structural parameters.

## 5.7 Summary

This chapter has dealt with the physical processes taking place when a contact is formed between a sample surface and a probe tip. It was found in section 5.3 that this process happens on a millisecond time scale and is accompanied by a large conductance jump, mound formation, and conductance hysteresis. Evidence for spontaneously developing contacts and temperature-dependent prejumps in the tunneling regime was also presented. On these grounds, it was concluded in section 5.4 that the diffusion-to-contact scenario, recently proposed by Sørensen *et al.* [53], was most likely to be the underlying mechanism. Section 5.5 focused on an effect not reported previously, namely polarity-dependent contact formation. For a Cu tip-sample system, it was found that a contact develops at a larger gap distance when electrons are tunneling from the sample to the tip, compared to the opposite current direction. This effect was seen at 170 K, RT, and 390 K, and, furthermore, at RT, it depended on the magnitude of the current. Also observed at RT was the existence of tunneling conductances as high as five quantum units. In section 5.6, these findings were discussed, and it was concluded that further experimental investigations are necessary in order to provide a model for the observed behavior.

## References

- [1] F. P. Bowden and D. Tabor, Proc. R. Soc. London, Ser. A **169**, 391 (1939).
- [2] I. L. Singer, J. Vac. Sci. Technol. A **12**, 2605 (1994).
- [3] D. W. Abraham, H. J. Mamin, E. Ganz, and J. Clarke, IBM J. Res. Dev. **30**, 492 (1986).
- [4] R. S. Becker, J. A. Golovchenko, and B. S. Swartzentruber, Nature **325**, 419 (1987).

- [5] I.-W. Lyo and P. Avouris, *Science* **253**, 175 (1991).
- [6] P. Avouris, I.-W. Lyo, and Y. Hasegawa, *J. Vac. Sci. Technol. A* **11**, 1725 (1993).
- [7] M. Aono *et al.*, *Japanese Journal of Applied Physics* **32**, 1470 (1993).
- [8] H. Uchida, D. Huang, F. Grey, and M. Aono, *Phys. Rev. Lett.* **70**, 2040 (1993).
- [9] F. Grey *et al.*, *Proceedings of the Japan Academy* **69**, 101 (1993).
- [10] J. Schneir *et al.*, *J. Appl. Phys.* **63**, 717 (1988).
- [11] Y. Z. Li *et al.*, *Appl. Phys. Lett.* **54**, 1424 (1989).
- [12] P. F. Marella and R. F. Pease, *Appl. Phys. Lett.* **55**, 2366 (1989).
- [13] H. J. Mamin, P. H. Guethner, and D. Rugar, *Phys. Rev. Lett.* **65**, 2418 (1990).
- [14] J. I. Pascual *et al.*, *Phys. Rev. Lett.* **71**, 1852 (1993).
- [15] J. Méndez *et al.*, *J. Vac. Sci. Technol. B* **14**, 1145 (1996).
- [16] H. J. Mamin and D. Rugar, *Phys. Rev. Lett.* **72**, 1128 (1994).
- [17] R. Taylor *et al.*, *Surf. Sci.* **306**, L534 (1994).
- [18] C. S. Chang, W. B. Su, and T. T. Tsong, *Phys. Rev. Lett.* **72**, 574 (1994).
- [19] D. M. Eigler, C. P. Lutz, and W. E. Rudge, *Nature* **352**, 600 (1991).
- [20] K. S. Ralls, D. C. Ralph, and R. A. Buhrman, *Phys. Rev. B* **40**, 11561 (1989).
- [21] T. T. Tsong, *Phys. Rev. B* **44**, 13703 (1991).
- [22] N. M. Miskovsky and T. T. Tsong, *Phys. Rev. B* **46**, 2640 (1992).
- [23] N. M. Miskovsky, C. M. Wei, and T. T. Tsong, *Phys. Rev. Lett.* **69**, 2427 (1992).
- [24] N. D. Lang, *Phys. Rev. B* **45**, 13599 (1992).
- [25] N. D. Lang, *Phys. Rev. B* **49**, 2067 (1994).
- [26] K. Hirose and M. Tsukada, *Phys. Rev. Lett.* **73**, 150 (1994).
- [27] J. J. Sáenz and N. García, *Phys. Rev. B* **47**, 7537 (1993).
- [28] U. Gratzke and G. Simon, *Phys. Rev. B* **52**, 8535 (1995).
- [29] J. B. Pethica and W. C. Oliver, *Phys. Scr.* **T 19**, 61 (1987).
- [30] J. B. Pethica and A. P. Sutton, *J. Vac. Sci. Technol. A* **6**, 2490 (1988).
- [31] J. R. Smith, G. Bozzolo, A. Banerjee, and J. Ferrante, *Phys. Rev. Lett.* **63**, 1269 (1989).
- [32] U. Landman, W. D. Luedtke, N. A. Burnham, and R. J. Colton, *Science* **248**, 454 (1990).

- [33] U. Landman and W. D. Luedtke, *Applied Surface Science* **60/61**, 1 (1992).
- [34] P. A. Taylor, J. S. Nelson, and B. W. Dodson, *Phys. Rev. B* **44**, 5834 (1991).
- [35] R. M. Lynden-Bell, *Surf. Sci.* **244**, 266 (1991).
- [36] J. S. Nelson, B. W. Dodson, and P. A. Taylor, *Phys. Rev. B* **45**, 4439 (1992).
- [37] M. Lupkowski and J. F. Maguire, *Phys. Rev. B* **45**, 13733 (1992).
- [38] B. S. Good and A. Banerjea, *J. Phys. Condens. Matter* **8**, 1325 (1996).
- [39] J. K. Gimzewski and R. Möller, *Phys. Rev. B* **36**, 1284 (1987).
- [40] U. Dürig, O. Züger, and D. W. Pohl, *Phys. Rev. Lett.* **65**, 349 (1990).
- [41] P. Zeppenfeld, C. P. Lutz, and D. M. Eigler, preprint (unpublished).
- [42] N. Agraït, J. G. Rodrigo, and S. Vieira, *Phys. Rev. B* **47**, 12345 (1993).
- [43] N. Agraït, J. G. Rodrigo, C. Sirvent, and S. Vieira, *Phys. Rev. B* **48**, 8499 (1993).
- [44] A. Stalder and U. Dürig, *J. Vac. Sci. Technol. B* **14**, 1259 (1996).
- [45] J. M. Krans *et al.*, *Phys. Rev. B* **48**, 14721 (1993).
- [46] J. M. Krans and J. van Ruitenbeek, *Phys. Rev. B* **50**, 17659 (1994).
- [47] C. J. Muller, J. M. Krans, T. N. Todorov, and M. A. Reed, *Phys. Rev. B* **53**, 1022 (1996).
- [48] J. Voets, R. J. P. Keijsers, O. I. Shklyarevskii, and H. van Kempen, *Phys. Rev. B* **53**, 1072 (1996).
- [49] D. P. E. Smith, *Science* **269**, 371 (1995).
- [50] N. D. Lang, *Phys. Rev. B* **36**, 8173 (1987).
- [51] L. Kuipers and J. W. M. Frenken, *Phys. Rev. Lett.* **70**, 3907 (1993).
- [52] L. Kuipers, M. S. Hoogeman, and J. W. M. Frenken, *Surf. Sci.* **340**, 231 (1995).
- [53] M. R. Sørensen, K. W. Jacobsen, and H. Jónsson, submitted to *Phys. Rev. Lett.* (unpublished).
- [54] J. Ferrer, A. Martín-Rodero, and F. Flores, *Phys. Rev. B* **38**, 10113 (1988).



## Chapter 6

# Quantized Conductance

### 6.1 Introduction

In 1987 van Wees *et al.* [1] and Wharam *et al.* [2] independently discovered a sequence of steps in the conductance of a point contact as its width was varied. Ever since, a large theoretical and experimental effort has been put in the subject. The experimental work has mainly concentrated on the conductance of a two-dimensional electron gas (2DEG), confined in a semiconductor heterostructure at 4.2 K or below (see Ref. [3] for a review). There are several reasons why semiconductors are a natural choice in these experiments. First, the dimensions of the conductor have to be small compared to the mean-free path of the electrons, which implies that scattering will predominantly take place at the boundaries of the conductor, i.e., the transport is ballistic. In semiconductors, a mean-free path of several micrometers can be achieved, turning ballistic transport into an almost macroscopic phenomenon. In comparison, the mean-free path in metals is of the order of 100 Å. A further constraint is that, in order to observe quantization, the conduction should be confined within a constriction of width comparable to an electronic wavelength. Since the Fermi wavelength of a semiconductor system is  $\approx 400$  Å, while it is typically  $\approx 5$  Å in a metal, the restrictions on the contact dimensions are much more severe in the case of a metal, where atomic scale contacts are needed.

Semiconductor systems have the additional advantage that it is possible to fabricate devices with voltage-controllable contact widths — by applying a voltage to a split gate, the 2DEG regions under the gate are depleted, leaving a narrow path undepleted. In this way, it is not neces-

sary to have any kind of mechanical movement in the system, however, as a direct consequence of the relatively large dimensions of the constricted conductor ( $\approx 100 \text{ nm} - 1 \mu\text{m}$ ), this method requires temperatures at 4 K or below due to the smearing of the Fermi distribution at higher temperatures.

As already described in the previous chapters, nanowires can be made by indenting the tip of an STM into a metallic sample. During the subsequent withdrawal, the nanowire is stretched and thinned until the point, where the strain gets too large, and disruption inevitably results. The atomic dimensions of such nanowires may facilitate observations of the quantized nature of conductance, despite the small metallic Fermi wavelength. Furthermore, these experiments do not require very low temperatures, rather, they can be carried out at RT.

This is the topic of the present chapter, which, from an experimental point of view, is an extension of the publications I and III. A slightly reformulated version of the theoretical part is also included, which enables a discussion of the experimental findings. The outline is as follows: First, an introduction to the theoretical background necessary for an understanding of the physics behind conductance quantization will be given. Here, it will also be discussed why a large controversy exists in relation to conductance quantization in metallic systems. Then a review of works in the field of metallic nanowire conductance follows in section 6.3. In section 6.4 the experimental results will be presented, revealing the outstanding properties of Au nanowires. A theoretical description, which can account semi-quantitatively for several of the observed effects for Au, is introduced in section 6.5, while further discussions can be found in section 6.6. Finally, the last section contains a brief summary.

## 6.2 Theoretical Background

Consider a metallic rod of length  $l$  and radius  $a$  corresponding to a circular cross-sectional area  $A$ . If a bias positive voltage  $V_b$  is applied to the left-hand end of the rod, while the other end is grounded, a current will flow towards the right-hand side. In the Maxwellian diffusive regime, the conductance of the rod is given by

$$G_{dif} = I/V_b = \frac{A}{l} \sigma = \pi \frac{a^2}{l} \sigma, \quad (6.1)$$

where  $\sigma$  is the material-dependent conductivity. Even though  $G_{dif}$  is inversely proportional to  $l$ , this does not mean that  $G_{dif}$  increases towards

infinity as  $l$  shrinks towards zero. Under these circumstances, Eq. (6.1) is not valid, instead the conductance will asymptotically reach a value given by  $G_{dif} = 2a\sigma$ . This result can be found by solving the Laplace equation in oblate spheroidal coordinates with the proper boundary conditions [4]. Note that  $G_{dif}$  still depends on the conductivity, and rather than being proportional to  $a^2$ , it is now linear in  $a$ .

By decreasing the width of the conductor to a few hundred ångströms, the transport becomes ballistic, and Eq. (6.1) no longer applies. However, a ballistic transport equation can easily be derived in a free-electron model. If  $V_D$  is the volume of the unit sphere in  $D$  dimensions, then the density of electrons with one-electron energies less than  $E = \hbar^2 k^2 / 2m$  becomes

$$n(k) = 2 \left[ \frac{V_D k^D}{(2\pi/L)^D} \right] / L^D = 2 V_D \left( \frac{k}{2\pi} \right)^D, \quad (6.2)$$

where the factor of two accounts for spin,  $V_D k^D$  is the volume of the  $D$ -dimensional  $k$ -space sphere,  $(2\pi/L)^D$  is the  $k$ -space volume per  $k$  vector, and  $L^D$  is the real-space volume. This gives a density of one-electron states per unit volume,

$$\rho(k) = \frac{dn}{dE} = \frac{dn}{dk} \left( \frac{dE}{dk} \right)^{-1} = \frac{2 D V_D k^{D-2} m}{(2\pi)^D \hbar^2}. \quad (6.3)$$

The current through the conductor can be written as the product of the electronic charge  $e$ , the average transport velocity parallel to the conductor  $\langle v_{\parallel} \rangle$ , the cross-sectional area  $A$ , and the effective density of electrons taking part in the transport process  $n_{tr}$ , that is,  $I = e \langle v_{\parallel} \rangle A n_{tr}$ . In the limit of vanishing  $V_b$  and zero temperature,  $\langle v_{\parallel} \rangle$  will be the parallel component of the Fermi velocity  $v_F$  averaged over the left-hand half of the Fermi sphere (the electrons are moving from right to left),

$$\langle v_{\parallel} \rangle = \frac{1}{2\pi} \int_0^{2\pi} d\phi \int_0^{\pi/2} (v_F \cos \theta) \sin \theta d\theta = v_F / 2 = \frac{\hbar k_F}{2m}. \quad (6.4)$$

Exploiting the symmetry of the Fermi sphere, the density of left-moving electrons in the energy interval from  $E_F$  to  $E_F + eV_b$  can be written as  $n_{tr} = [\rho(k_F)/2] eV_b$ , where  $\rho(k_F)$  is to be evaluated in three dimensions. Finally, the expression for the ballistic conductance can be found,

$$G_S = I/V_b = \frac{2e^2 k_F^2}{h} \frac{A}{4\pi} = \frac{2e^2 k_F^2}{h} \frac{a^2}{4}. \quad (6.5)$$

This is the Sharvin expression for ballistic conductance [5,6]. Although not reflected by the derivation, it describes pure classical electron transport in the absence of bulk scattering<sup>1</sup>. In this regime, the conductance is totally independent of material properties — it only depends on the electron density [via  $k_F$ , see Eq. (6.2)] and the geometry of the sample (here specified by  $a$  or  $A$ ).

Reducing the size of the metallic “rod”, or nanowire, even further, the conductance may eventually turn quantized when the width becomes comparable to the Fermi wavelength, i.e., when the atomic scale is reached. The transport problem then changes from being three-dimensional to being quasi one-dimensional, that is, the equation of motion can be separated into one equation describing the motion along the wire ( $z$ ) and another describing the perpendicular motion ( $xy$ ). Assume for the moment that the motion is purely one-dimensional. Proceeding very much in the same way as for the Sharvin conductance above, the infinitesimal current contribution  $dI_l$  from left-moving electrons in the energy interval from  $E = \hbar^2 k^2/2m$  to  $E + dE$  can be written as the product of the electronic charge, the group velocity  $\hbar k/m$ , and the number of left-moving states per unit length  $[\rho(k)/2]dE$ , where  $\rho$  now is to be evaluated in one dimension,

$$dI_l = e \frac{\hbar k}{m} \frac{\rho(k)}{2} dE = e \frac{\hbar k}{m} \frac{m}{\pi \hbar^2 k} dE = \frac{2e}{h} dE. \quad (6.6)$$

Only left-moving states with energy between  $E_F$  and  $E_F + eV_b$  will contribute to the total current, which then becomes

$$I = \frac{2e}{h} \int_{E_F}^{E_F + eV_b} dE = \frac{2e^2}{h} V_b \Rightarrow G = \frac{2e^2}{h}. \quad (6.7)$$

This equation states that the conductance for a perfect homogeneous one-dimensional conductor at zero temperature is equal to  $2e^2/h$ , that is, one quantum unit of conductance ( $G_0$ ). If a barrier is introduced somewhere in the conductor, then  $G$  will depend on the probability for passing that barrier, i.e.,  $G = (2e^2/h) \mathcal{T}$ , where  $\mathcal{T}$  is the transmission.

The relevance for the real three-dimensional nanowire will become clear after the wave function of the system has been examined. If the  $xy$  behavior varies sufficiently slowly with  $z$ , then the two-dimensional

---

<sup>1</sup>The Sharvin conductance can also be derived directly from the Drude theory, where it has the form  $G_S = 3A\sigma/4l_m$ , where  $l_m$  is the mean-free path. Using Eq. (6.2),  $\sigma = ne^2\tau/m$ , and  $l_m = \tau v_F$ , where  $\tau$  is the relaxation time, it is easy convert back to Eq. (6.5) by insertion.

Schrödinger equation in  $x$  and  $y$  can be solved for each  $z$ , resulting in two-dimensional wave functions  $\chi$ . Using these as a basis, the full three-dimensional wave function  $\psi$  can be expanded as

$$\psi(x, y, z) = \sum_n \chi_{z,n}(x, y) \phi_n(z), \quad (6.8)$$

where  $\chi_{z,n}$  are the solutions to

$$\left[ -\frac{\hbar^2}{2m} \left( \frac{\partial^2}{\partial x^2} + \frac{\partial^2}{\partial y^2} \right) + V(x, y, z_0) \right] \chi_{z_0,n}(x, y) = E_n^\perp(z_0) \chi_{z_0,n}(x, y), \quad (6.9)$$

and  $\phi_n$  are the  $z$ -dependent expansion coefficients.

The equation for the  $z$  motion is obtained by inserting  $\psi(x, y, z)$  in the full three-dimensional Schrödinger equation, which gives

$$\left( -\frac{\hbar^2}{2m} \frac{\partial^2}{\partial z^2} + E_n^\perp(z) \right) \phi_n(z) + \sum_m \hat{F}_{nm}^{coupling} \phi_m(z) = E_F \phi_n(z), \quad (6.10)$$

where the electron energy is set to  $E_F$  since only electrons in a narrow region around the Fermi energy contribute to the current. The operators  $\hat{F}_{nm}^{coupling}$  couple the different  $z$  solutions  $\phi_n$ ,

$$\hat{F}_{nm}^{coupling} = -\frac{\hbar^2}{2m} \left( \left\langle \chi_n(z) \left| \frac{\partial^2}{\partial z^2} \chi_m(z) \right. \right\rangle + 2 \left\langle \chi_n(z) \left| \frac{\partial}{\partial z} \chi_m(z) \right. \right\rangle \frac{\partial}{\partial z} \right). \quad (6.11)$$

Here is the motivation for the particular choice of expansion: If the variation of  $\chi_n$  with  $z$  in Eq. (6.8) is sufficiently slow, the *adiabatic* case, then the coupling between equations with different  $n$  by  $\hat{F}_{nm}^{coupling}$  can be neglected. In this case, Eq. (6.10) will, for each  $n$ , reduce to an isolated equation which has the form of a *one-dimensional* Schrödinger equation in  $z$  with the *effective potential barrier*  $E_n^\perp(z)$ .

Now the connection with Eq. (6.7) has been established. Each mode, or channel, characterized by the transverse quantum number  $n$ , gives a contribution  $(2e^2/\hbar) \mathcal{T}_n$  to the total conductance of the nanowire, that is,

$$G = \frac{2e^2}{h} \sum_n \mathcal{T}_n. \quad (6.12)$$

This is the Landauer expression for conductance in the quantum regime [7,8]. Strictly speaking, Eq. (6.12) is only valid at zero temperature. At

finite temperatures, a smearing of the Fermi function has to be accounted for. However, as will become evident later, this effect is not important at RT for ordinary metallic systems with a Fermi wavelength  $\approx 5 \text{ \AA}$ .

According to Eq. (6.12), the conductance will be determined by the transmission coefficients  $\mathcal{T}_n$  for the effective barriers  $E_n^\perp(z)$ . The general behavior of  $E_n^\perp(z)$  can be found by solving Eq. (6.9) within a simple model. Assume that the free-electron motion is confined by hard walls at the boundaries of the conductor which has a rectangular cross section with side lengths  $L_x(z)$  and  $L_y(z)$ . Then a solution fulfilling the boundary conditions  $\chi(\pm L_x/2, y) = \chi(x, \pm L_y/2) = 0$  can be written<sup>2</sup>:

$$\chi_{z,n}(x, y) = \frac{2}{\sqrt{L_x(z)L_y(z)}} \times \sin\left(\frac{n_x\pi}{L_x(z)}x - \frac{n_x\pi}{2}\right) \sin\left(\frac{n_y\pi}{L_y(z)}y - \frac{n_y\pi}{2}\right). \quad (6.13)$$

An expression for  $E_n^\perp(z)$  can now be found by inserting  $\chi_{z,n}(x, y)$  into Eq. (6.9),

$$E_n^\perp(z) = \frac{\pi^2\hbar^2}{2m} \left( \frac{n_x^2}{L_x(z)^2} + \frac{n_y^2}{L_y(z)^2} \right). \quad (6.14)$$

A similar behavior will be seen with other shapes of the confining potential, i.e.,  $E_n^\perp$  increases with increasing quantum numbers and with decreasing width of the conductor in a way very similar to Eq. (6.14). The conditions for adiabaticity now correspond to sufficiently slow variations in  $L_{x,y}$  as a function of  $z$ . Under these circumstances, the coupling between channels can be neglected, and each channel is described by an ordinary one-dimensional Schrödinger equation with a potential barrier  $E_n^\perp$ . In the simplest case, where the  $z$  variation is so slow that neither tunneling through the barrier nor reflection above it occurs, it can be assumed that a channel  $n$  is open ( $\mathcal{T}_n = 1$ ) if the top of the barrier  $E_n^\perp(z)$  is below  $E_F$  and closed ( $\mathcal{T}_n = 0$ ) otherwise. This gives the first crude approximation to the experiment: As the tip retracts and the nanowire is being pulled, it becomes more and more narrow, the barriers increase [see Eq. (6.14)], and one by one they pass through the Fermi level and close the corresponding channel. Each time a channel is closed, the conductance drops by  $2e^2/h$ . This is illustrated in Fig. 6.1 which visualizes the origin of the effective barrier. In the narrow part of the conductor, the transverse mode will

---

<sup>2</sup>Now,  $n$  is a shorthand notation for the two independent quantum numbers  $n_x$  and  $n_y$ .

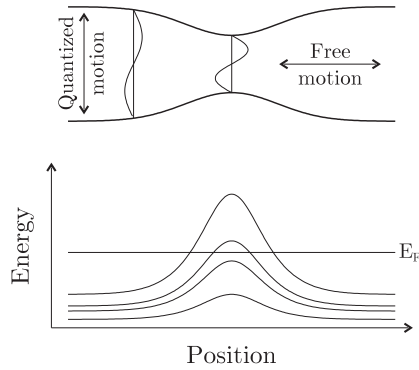


Figure 6.1: Conductance quantization can be explained as a consequence of the quantization of the transverse electronic motion in a smooth constriction. The energy of the transverse mode corresponds to an effective potential barrier for the longitudinal motion, due to energy conservation. Each of a finite number of modes with barriers below  $E_F$  will contribute with an amount  $2e^2/h$  to the total conductance.

be “squeezed” towards a shorter wavelength, that is, higher energy, and consequently, less energy will be available for the longitudinal motion.

Here, it is important to point out that, due to the smearing of the Fermi function, the steps in conductance will only be observed if the energy difference between the potential curves in Fig. 6.1 is large compared to  $kT$ . A simple example will show that this is indeed the case, even at RT. If, for example, the most narrow part of the conductor has dimensions  $L_x = 10 \text{ \AA}$  and  $L_y = 10 \text{ \AA}$ , then  $E_{1,1}^\perp = 0.75 \text{ eV}$ , while  $E_{2,1}^\perp = E_{1,2}^\perp = 1.9 \text{ eV}$ . In other words, the difference between two adjacent barriers is of the order 1 eV, which corresponds to a temperature above<sup>3</sup> 10 000 K. At RT, thermal excitation is only appreciable in a range of 0.025 eV around the Fermi level, and, consequently, it should be possible to observe conductance quantization at RT.

Apart from the necessity of atomic dimensions in metallic systems, there is one further complication that certainly has induced discussions in the literature. The problem can be illustrated by evaluating the cross-sectional area  $A$  of a constriction with a Sharvin conductance corresponding

<sup>3</sup>These large barrier spacings are a direct consequence of the atomic dimensions of the nanowire. In semiconductor split-gate devices the dimensions are two orders of magnitude larger, which results in barrier spacings of  $\approx 0.1 \text{ meV}$ , or  $\sim 1 \text{ K}$ .

to one quantum. If Au is used as an example then  $A$  can be found by setting  $k_F^2 = 2mE_F/\hbar^2 = (2m/\hbar^2) \times 5.5$  eV in Eq. (6.5). The result is  $A \approx 9 \text{ \AA}^2$ , which is very close to the cross section of a single atom. Envisage now a Sharvin conducting nanowire that undergoes the smallest restructuring possible, i.e., displacement of a single atom. If this atom is moved to or from the most narrow part of the nanowire, then the conductance will change by an amount which is the same order of magnitude as the fundamental quantum. So, even if conductance steps are detected, it is not necessarily an evidence for quantization.

### 6.3 Review

In 1992, Muller *et al.* reported results from experiments on a Pt sample carried out with the mechanically controllable break-junction (MCB) technique at 1.2 K [9], where steps in the conductance of an atomic-size metallic contact were observed as its width was varied. The size of the steps was of the order of  $2e^2/h$ , and by tuning the contact to coincide with a step, conductance fluctuations between two levels resulted, which were interpreted as a switching of a defect between two metastable positions in the constriction. Furthermore, as the steps were not exactly equal to  $G_0$ , it was concluded that they were caused by an atom-by-atom change in the size of the constriction.

Less than a year later, similar results were obtained on Au by Agraït *et al.* with an STM setup operating at 4.2 K [10]. In this case, however, the conductance always attained a value very close to one quantum unit immediately after the formation of a contact, and this was attributed to an opening of the first ballistic channel. Although not as sharp as the first step, steps possibly related to the second and third ballistic channel were also observed. It is worth noting that Agraït *et al.* associated the channel-opening process to atomic rearrangements in the contact, i.e., it was not considered whether conductance steps could arise in a contact which is elastically stretched or compressed.

Approximately at the same time, Todorov and Sutton made a tight-binding calculation of the conductance in a point contact between a tip and a surface [11]. The atomic evolution of the contact was obtained from dynamic simulations, revealing a series of mechanical instabilities as crystal planes were squeezed out/introduced during the tip advance/withdrawal. As a consequence, the cross-sectional area of the contact changed, causing a step in the conductance. In general, the conductance per atom was found

to be less than  $G_0$  ( $0.93 G_0$ ,  $0.69 G_0$ , and  $0.61 G_0$  for the first, second, and third step, respectively), which means that  $G$  was not simply proportional to the size of the contact.

Pascual *et al.* were the first to carry out an experiment at RT and ambient conditions [12]. Here Au contacts were formed by applying a voltage pulse to the junction. During the subsequent withdrawal of the tip, steps were observed in the conductance. The last steps before disruption of the contact could be interpreted as an integer number of conductance quanta. Similar results could be obtained at RT under clean conditions in UHV, as shown in publication I. Here the contact was formed by indenting the STM tip into Ni, Cu, and Pt surfaces. Furthermore, molecular-dynamics simulations of the stretch of nanowires were presented together with the corresponding conductance evolution, calculated in a free-electron model using the Landauer formalism [7,8]. It was found that the simple theoretical model was indeed able to reproduce the main features of the experimental observations. Within the model, it was also possible to explain degeneracies of conductance channels, that is, channels that close at the same time, giving rise to steps of two quanta or more. This effect was demonstrated by an experimental example.

This interpretation was at variance with a new MCB experiment by Krans *et al.* carried out at 4.2 K or below [13]. For Cu and Al, it was found that the conductance for a one-atom contact was very close to  $2e^2/h$ , whereas Pt gave values closer to  $1.5 G_0$ . Moreover, higher conductance plateaus, not in accordance with an integer number of quanta, were also observed, and it was concluded that the observations to a great extent corroborated the theoretical findings of Todorov and Sutton.

The effect of constriction geometry was investigated in a study of Torres *et al.* [14,15]. Here it was shown that large opening angles of the constriction would spoil the quantization, and furthermore, it was pointed out that a perimeter correction, due to the quantum uncertainty, had to be included in the expression for the Sharvin conductance for these atomic-sized constrictions. Torres *et al.* also addressed the question whether or not quantization could be observed experimentally. Even though the conductance per atom is of the order of a quantum, it is not constant as the width of the constriction changes. Consequently, it was concluded that *for small angles, where the conductance is quantized, the jumps must be in the form of integer multiples of  $2e^2/h$ , independently of the number of atoms forming the narrow constriction structure. Notice that in this case, the number of quantum channels is directly related not to the number of atoms but to the number of propagating modes: An atomic change of*

*the constriction cross section does not necessarily imply a change in the conductance.*

To provide good evidence for contact-area effects, Krans *et al.* also reported low-temperature results from experiments on the semimetal Sb which has a large Fermi wavelength ( $\approx 55 \text{ \AA}$ ) [16]. The conductance per atom will thus be much smaller than a quantum, facilitating a distinction of steps caused by atomic rearrangements. Indeed, subquantum steps of the order of  $0.01 G_0$  were observed, which demonstrates the discrete atomic nature of the contact. It was argued that *this strongly supports the idea that also the origin of the abrupt conductance steps observed in metals is purely geometrical.* Further support for this idea came from Dremov *et al.* [17] who made STM experiments on Au in air. Here steps were observed during tip approach and withdrawal. The authors argue that the neck formed between tip and surface is a strongly disordered system, which should prevent ballistic transport. Dremov *et al.* also did I-V measurements on stable point contacts formed between the W tip and the Au surface [18]. The results demonstrated changes in the differential conductance corresponding to  $e^2/h$  rather than to  $2e^2/h$ . It was suggested that this could be a manifestation of a lifting of the spin degeneracy in the W tip.

The divergence concerning the interpretation of the observed conductance steps induced a comment on publication I. Krans *et al.* pointed out that atomic rearrangements could not be excluded as a possible origin of the steps [19]. This statement was supported by measurements of their own, showing that non-integer conductance values could be observed, although, exceptionally, integer-value curves were also obtained. Furthermore, it was argued that the free-electron model employed in publication I was bound to result in conductance quantization, whereas it could not describe atomic rearrangements. Publication II was the reply to this comment. Here it was realized that a single measurement could not provide convincing evidence for, or against, conductance quantization. Since each point contact is individual and evolves in its own characteristic way during thinning, it may not reflect the overall properties of the constrictions. Consequently, a statistical treatment was employed instead, resulting in a histogram showing the distribution of conductance values measured in 59 indentations on Pt(100). In this way, data points were seen to gather around integer numbers of conductance quanta, supporting the original conclusion of quantization effects. This also demonstrated that the free-electron model was indeed a natural starting point for a theoretical discussion of the general conductance behavior in these metallic constrictions.

tions.

Approximately three month later, and after the results of the forthcoming publication III had been presented at the Second International Conference on Point-contact Spectroscopy held in Nijmegen in 1995, Krans *et al.* reported new results from measurements on Na and Cu at 4.2 K [20]. Here the authors state: *The conductance steps reported in the(se) earlier experiments might be attributable to discrete rearrangements of the atomic structure of the contact, rather than true conductance quantization. Here we use the fact that the degeneracy of the conduction modes of a three-dimensional point contact should result in a characteristic sequence of conductance values (some integer multiples of  $2e^2/h$  are excluded) to distinguish the effects of conductance quantization from those of discrete variations in contact size in a break-junction experiment, confirming that conductance quantization does indeed occur.* This rather sudden change in opinion was based on a statistical histogram analysis analogous to the one in publication II.

In a combined experimental and theoretical paper, Pascual *et al.* found that conductance steps often were accompanied by small dips before plateaus at an integer number of quantum units evolved in a Au contact in air [21]. This was interpreted as quantization, and the dips were attributed to enhanced scattering in the contact when it undergoes an order-disorder-order transition during yielding between two elastic stages. Agraït *et al.* also investigated the evolution of the contact during stretching [22,23]. Here focus was put on large conductance steps, corresponding to 10–20  $G_0$ , in contacts of Pb and Au at 4.2 K. In the latter case, both the conductance and the force were measured, revealing a series of elastic and yielding stages during elongation. Plateaus in the conductance were found to be correlated with elastic deformations, in which the mechanical force increases linearly as a function of displacement. Conductance steps between two plateaus were associated with a sudden decrease in the mechanical force, that is, a relief of the strain in a yielding process.

An possible explanation for many of the discrepancies between RT experiments and experiments carried out at 4.2 K or below was provided by Bratkovsky *et al.* [24]. They calculated the conductance of a constriction both in a free-electron model (FE) and in a tight-binding scheme (TB) for three different temperatures: 10 K, 150 K and 250 K. At low temperatures, only the FE model shows any sign of quantization, and this at the very last stage of neck elongation before the final disruption. In clear contrast to this were the RT results, where both models demonstrate quantization. The reason for this temperature effect is to be found in the

geometry and the atomic structure of the constriction. At low temperatures, the neck is “frozen” in unfavorable configurations with a rough boundary and internal disorder. This causes a high electron backscattering which destroys the well defined conductance steps. On the contrary, at RT, the atoms have a kinetic energy which enables the contact to minimize its surface free energy and obtain a high degree of crystalline structure. As a result, the contact becomes very smooth, and backscattering is reduced substantially. In other words, the rather remarkable conclusion is that in order to observe conductance quantization in metallic systems, high temperatures are needed, the reason being that mechanical properties of the contact are the limiting factors.

In September 1995 was publication III released. Here, the Pt results in publication II were substantiated by measurements on Au, showing clear evidence for conductance quantization at RT. A very good agreement between the experimental results and a theoretical free-electron model, which includes scattering at the boundaries of the conductor, was found. These results, among others, will be presented in this chapter.

Later, the findings of conductance quantization at RT have been confirmed [25,26], although the discussion concerning an interpretation in terms of quantization or cross-sectional jumps has continued [27–29]. Most excitingly, it has also been found that quantization can be observed at RT and ambient conditions with macroscopic wires [30–32].

## 6.4 Experimental Results

The conductance evolution during the final stages of neck elongation is shown in Fig. 6.2(a) for six *randomly* selected indentations on Pt(100) at RT. Some of the curves are characterized by one or several conductance drops followed by plateaus or more moderate decreases. However, it is not at all evident from Fig. 6.2(a) whether quantization is present, as the plateaus, or slowly declining sections, are not very well defined, and moreover, the distribution of plateaus does not indicate a preference for integer numbers of quantum units. Even though it is possible, from a large data set, to find examples with rather well defined steps at integer multiples of  $G_0$ , these do obviously not represent the general behavior, and, as indicated in the last paragraph of section 6.5, such steps are not necessarily evidence for quantization.

The notion of an even distribution of steps is verified from the continuous conductance histogram shown in Fig. 6.2(b) (for a detailed descrip-

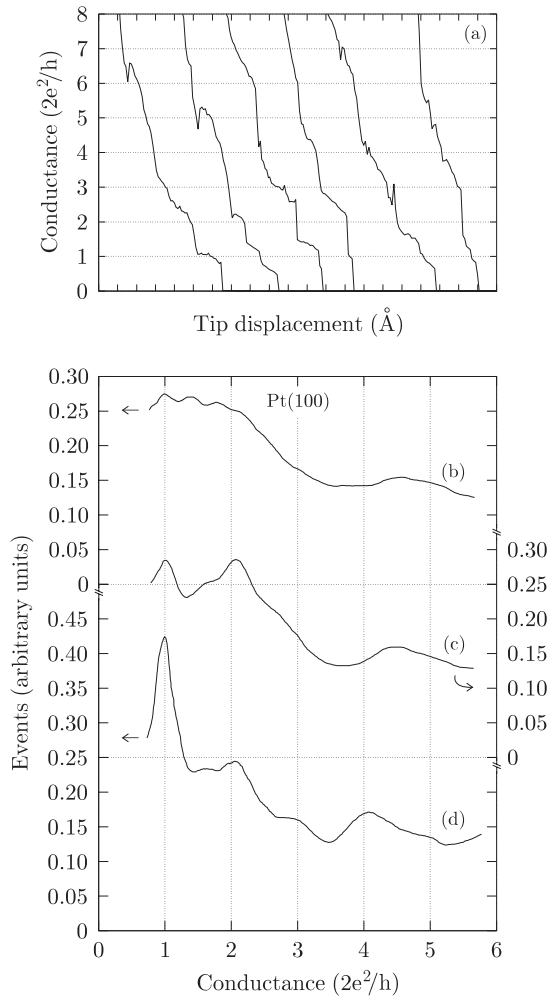


Figure 6.2: Upper panel: Six randomly selected examples of the conductance measured during the last part of the neck-elongation process for indentations on Pt(100) at RT (a). The curves have been displaced along the horizontal axis for clarity. Lower panel: Continuous conductance histograms for Pt(100) at RT, including all indentations (b), indentations with a neck length larger than  $8 \text{ \AA}$  (c), and ditto with the additional constraint that no non-metallic plateaus should be observed (d). The number of indentations included is 155 (b), 97 (c), and 43 (d). See text for further details.

tion of histograms see section B.3 on page 155). No significant features are seen, rather a slowly varying function with a broad maximum located around  $1-2 G_0$  is observed. From these data, it can immediately be concluded that quantization, if present at all, must be a minor effect which is not resolved in (b). This observation induces the following question: Are there any circumstances which will tend to favor quantization and make it observable? One way to answer this question is to make histograms of appropriate subsets of the data included in Fig. 6.2(b). From theoretical studies, showing that large opening angles of the constriction can destroy well defined quantum steps [33,14,15,34], it is expected that the length of the neck may be an important parameter in this connection. Consequently, in Fig. 6.2(c) is shown a histogram made from the same data set as in (b), except that only the conductance of nanowires attaining a length larger than  $8 \text{ \AA}$  is included. As a result, the broad maximum in (b) has separated into two peaks centered around  $1 G_0$  and  $2 G_0$ , respectively.

A further constraint can be invoked from the observation that frequently anomalously low conductance plateaus (less than  $0.1 G_0$ ) are present in measurements on Pt. These plateaus can only be explained as a consequence of a non-metallic mechanical contact<sup>4</sup>, that is, a contact which probably contains impurities. Motivated by these considerations, indentations with anomalously low conductance plateaus have been left out in the histogram shown in Fig. 6.2(d). Now, a prominent peak at  $1 G_0$  is seen, and furthermore, minor peaks at two, four, and maybe even three quantum units are identified.

Random examples of conductance evolutions measured on Ni(111) at RT are displayed in Fig. 6.3(a). In many ways, these curves are similar to those measured for Pt(100) [Fig. 6.2(a)], i.e., conductance plateaus and subsequent drops can be distinguished, albeit no clear preference for specific values is revealed. Again, it should be emphasized that it is possible to pick out single curves which apparently are in agreement with conductance quantization, although the picture in Fig. 6.3(a) is more blurred.

A continuous histogram for Ni(111) including all indentations is shown in Fig. 6.3(b). Unlike the Pt histogram in Fig. 6.2(b), there is a strong decrease from the maximum at  $\approx 1.8 G_0$  towards lower conductances, which means that the probability for measuring a value of  $1 G_0$  is small.

---

<sup>4</sup>During neck elongation, a large strain is built up in the contact. When disruption takes place, this strain is relieved by a fast relaxation of neck atoms towards the electrodes. This is the reason why the conductance usually drops all the way to the detection limit rather than ending up in the tunneling regime. If, however, the conductance drops to an anomalously low value, then no strain relief has taken place, i.e., there is still a mechanical contact between tip and sample.

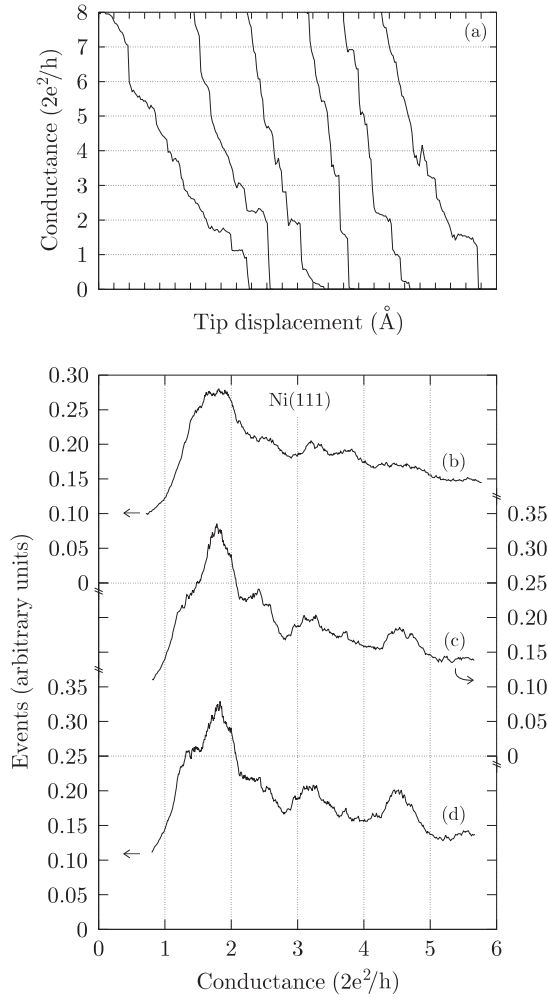


Figure 6.3: Upper panel: Six randomly selected examples of the conductance measured during the last part of the neck-elongation process for indentations on Ni(111) at RT (a). The curves have been displaced along the horizontal axis for clarity. Lower panel: Continuous conductance histograms for Ni(111) at RT, including all indentations (b), indentations with a neck length larger than  $10 \text{ \AA}$  (c), and ditto, with the additional constraint that no non-metallic plateaus should be observed (d). The number of indentations included is 360 (b), 60 (c), and 48 (d). See text for further details.

Apart from the broad peak just below  $2 G_0$  and some minor bulges in the intervals  $3-4 G_0$  and  $4-5 G_0$ , no characteristics are revealed. Histograms based on restricted subsets of the indentations included in (a) are shown in (b) and (c). However, in this case, the only effect of the constraints is a sharpening of the features already present in (a), resulting in peaks at approximately  $1.8 G_0$ ,  $3.2 G_0$ , and  $4.5 G_0$ .

Results from indentations on Cu(100) are shown in Fig. 6.4. The randomly selected examples displayed in (a) exhibit very few well defined conductance plateaus. Instead, a large number of oscillatory behaviors are present, i.e., conductance drops are immediately followed by increases of  $0.5-1 G_0$  which, in turn, are succeeded by larger drops, resulting in a steep overall conductance decrease as the nanowires are stretched. In fact, the Cu necks do not withstand very large tip displacements — the degradation and final disruption is rather abrupt and takes place within an elongation of  $2-3 \text{ \AA}$  from the position characterized by a conductance of  $8 G_0$ . This is approximately a factor of two lower than that observed for Ni and Pt.

Histograms for Cu, including all indentations carried out at 390 K, RT, and 170 K, are shown in Fig. 6.4(b), (c), and (d), respectively. The results for negative and positive polarity have been shown separately, as they do not coincide. In general, a peak centered at  $1-1.5 G_0$  is recognized<sup>5</sup> along with a broader peak in the vicinity of  $G = 3 G_0$ . This picture is not changed by data-set restrictions analogous to the ones employed in the case of Pt. A close inspection of the lower panel in Fig. 6.4 reveals that while the peak positions are coinciding at RT, the negative-polarity histogram is shifted towards higher/lower conductance values at 390 K/170 K relative to the histogram for positive polarity. This is a strong indication of a thermovoltage effect inside the UHV chamber<sup>6</sup> (see section B.1 in appendix B for details). However, no correction has been made, as the histograms are not simply phase-shifted replica of each other. For example, the significant peak at  $4.5 G_0$  observed for positive polarity at 390 K apparently does not have a match at negative polarity.

Random examples of the conductance evolution in Au necks are shown in Fig. 6.5(a). Unlike the situation for Ni, Cu, and Pt, the general trend for Au is very clear: As the neck is elongated, the conductance decreases in steps of one, two, or three quantum units. In between steps, the conduc-

---

<sup>5</sup>At 170 K and negative polarity, no peak is observed in the vicinity of  $1 G_0$ . However, a strong increase for decreasing conductances is revealed, and this is likely to be the tail of a peak lying just outside the range of the histogram.

<sup>6</sup>Since both tip and sample consist of Cu in these experiments, this observation suggests that the thermo voltage is not lying across the junction, as was first anticipated.

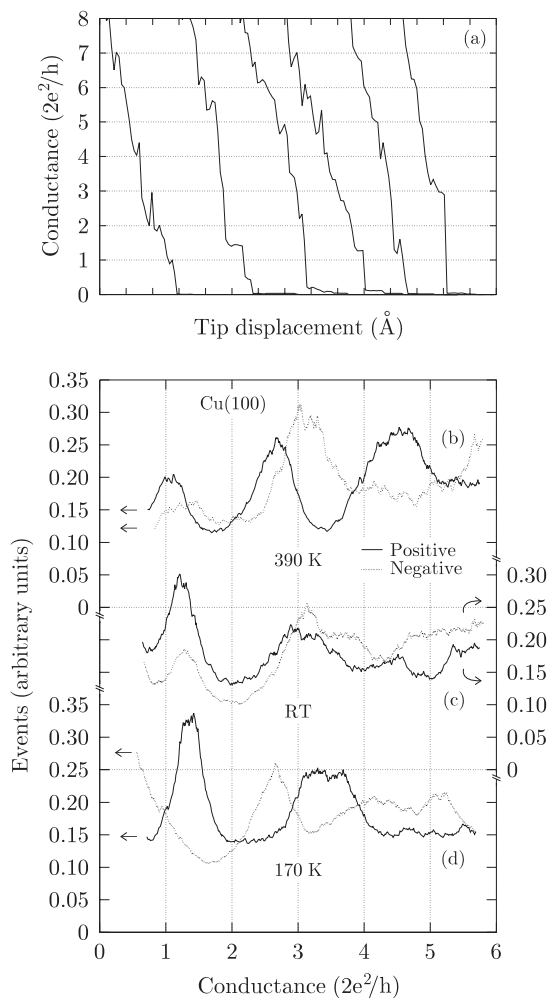


Figure 6.4: Upper panel: Examples picked at random, showing the conductance during the last part of the neck-elongation process for indentations on Cu(100) at RT (a). The curves have been displaced along the horizontal axis for clarity. Lower panel: Conductance histograms including all indentations (more than a hundred in each case) measured at 390 K (b), RT (c), and 170 K (d). The histograms for positive and negative polarity do not coincide and are therefore both shown. See text for further details.

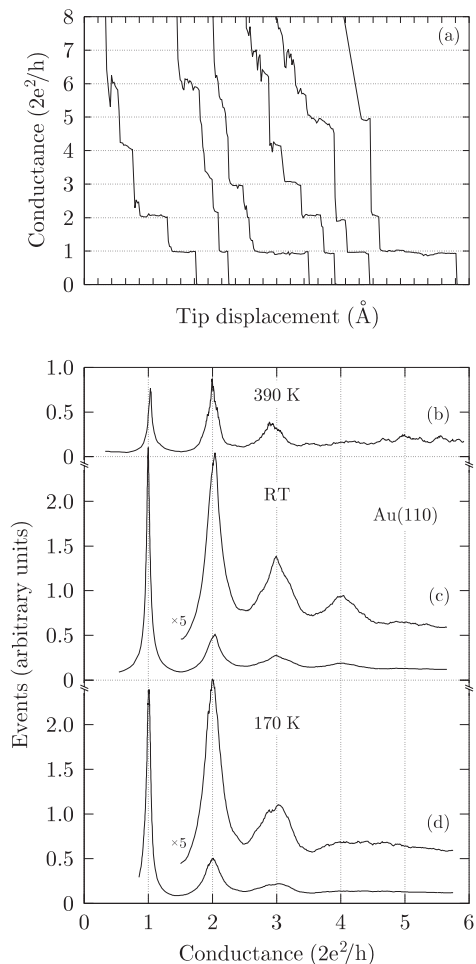


Figure 6.5: Upper panel: Examples picked at random, showing the conductance during the last part of the neck-elongation process for indentations on Au(110) at RT (a). The curves have been displaced along the horizontal axis for clarity. Lower panel: Conductance histograms including data points from all indentations (more than a 350 in each case) in series of measurements carried out at 390 K (b), RT (c), and 170 K (d). The data have been corrected for thermovoltages [ $150 \pm 10 \mu\text{V}$  (b),  $-10 \pm 2 \mu\text{V}$  (a)+(c), and  $-165 \pm 2 \mu\text{V}$  (d)] and tip resistances [ $200 \pm 50 \Omega$  (b),  $230 \pm 50 \Omega$  (a)+(c)+(d)]. For a further discussion of thermovoltages and tip resistances, consult section B.1 in appendix B.

Table 6.1: Conductance at the center positions of the histogram peaks shown in Fig. 6.5 obtained by fitting to Lorentzian functions with linear backgrounds. The stated uncertainties reflect the uncertainties of the thermo-voltages and the tip resistances (see caption of Fig. 6.5).

Temperature	Conductance at histogram peaks ( $2e^2/h$ )			
390 K	$1.03 \pm 0.01$	$2.00 \pm 0.02$	$2.92 \pm 0.07$	—
RT	$0.997 \pm 0.004$	$2.02 \pm 0.02$	$3.01 \pm 0.04$	$4.02 \pm 0.07$
170 K	$1.006 \pm 0.008$	$2.00 \pm 0.02$	$3.01 \pm 0.04$	—

tance stays fairly constant at plateaus corresponding to an integer number of  $G_0$ . The widest and most well defined plateaus are found at one, two, and three quanta, and, rather remarkably, the conductance can stay constant at  $G = G_0$  for a tip displacement as long as 5 Å, that is, a displacement much larger than a typical metallic bond length. These general observations are also reflected in the histograms shown in Fig. 6.5(b), (c) and (d), which are based on the entire data sets from series of measurements at 390 K, RT, and 170 K, respectively<sup>7</sup>. Immediately apparent are the prominent peaks at one, two, three, and four (RT) quantum units. The peak positions listed in Table 6.1 have been found by fitting each individual peak to a Lorentzian function with a linear background.

The stability of Au nanowires with a conductance of one quantum unit is further demonstrated in Fig. 6.6. Here the time evolution of a one-quantum contact was measured at 170 K. This was accomplished by continuously monitoring the conductance during a tip retreat sequence. As soon as a value lower than  $2 G_0$  was detected, an interruption of the tip movement was effectuated by “freezing” the voltage on the  $z$  piezo element. Then, during a time period of 33 ms, the conductance was recorded at a fixed tip-sample separation (shown in insert). Finally, the tip retraction was resumed, forcing a disruption of the contact. The resulting conductance curve shown in Fig. 6.6 reveals that the one-quantum contact does not undergo any degradation on a millisecond time scale, and furthermore, when retraction is continued, the nanowire withstands an elongation of 3 Å.

<sup>7</sup>In publication III the experimental histogram was subject to restrictions analogous to the ones employed for Pt. However, it has turned out that for Au, the restrictions are essentially without any effect.

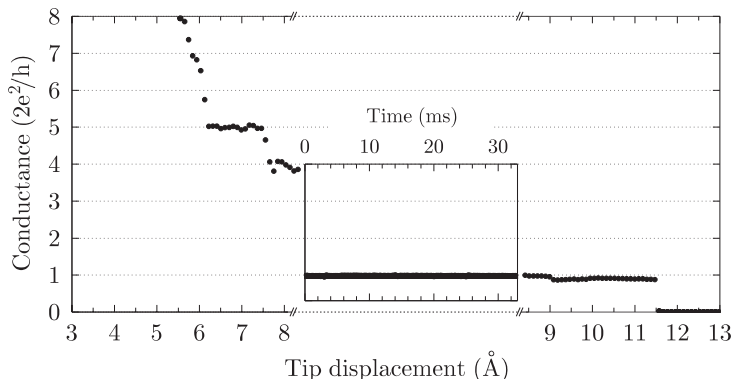


Figure 6.6: Conductance measured as a function of tip displacement and time (insert) at 170 K. During tip withdrawal, the conductance was continuously monitored. As soon as it dropped below a preset value of two quantum units, the tip motion was stopped by “freezing”  $V_z$ . Then, throughout a time period of 33 ms, the conductance was measured 512 times at a fixed tip-surface distance (insert) before the retraction was resumed.

## 6.5 Discussion of the Ideal Case — Gold

In the last paragraph of section 6.2, it was shown that the Sharvin conductance of a single atom is of the order of one quantum<sup>8</sup>. A displacement of a single atom in a nanowire can thus give rise to a conductance jump comparable to  $G_0$ . However, there is no reason to expect that the two quantities will be exactly equal, and, consequently, it is very unlikely that the peaks observed in the Au conductance histograms, which, within very small uncertainties, are lying at integer numbers of  $G_0$ , are caused by a Sharvin behavior. Furthermore, it is very difficult, within a Sharvin picture, to explain how conductance plateaus corresponding to  $1 G_0$  can stay unperturbed during a tip retraction of 3–5  $\text{\AA}$  since atomic rearrangements in the nanowire are bound to take place. It can therefore be concluded, based on the results presented in Fig. 6.5 and 6.6, that the conduction in atomic-sized Au nanowires drawn between an STM tip and a Au surface in UHV proceeds via modes, or channels, defined by the quantized motion of electrons in the transverse directions of the wire.

<sup>8</sup>Whether or not this description is reasonable will be briefly touched upon in section 6.6.

The remainder of this section is devoted to a theoretical modeling of the neck evolution and the corresponding conductance of Au nanowires during the stretching process at RT. Based on the modeling, a discussion of the experimental findings will be given, and in particular, the scaling of the areas and widths of the histogram peaks with  $G$  will be focused on. The theoretical description consists essentially of two parts; the instantaneous configuration of a nanowire at a particular point of elongation is found from molecular-dynamics simulations<sup>9</sup>, while the conductance is calculated in a free-electron model which includes scattering at the boundaries of the conductor<sup>10</sup>.

The molecular-dynamics simulations have been performed by using an interaction potential derived from the effective-medium theory [35]. As discussed in chapter 3, it is assumed that the surface metal wets the tip, resulting in contacts consisting of the surface metal only. In the simulations, a sharp pyramid-shaped tip is brought into contact with a surface, see Fig. 6.7. At RT, diffusion processes will take place on the time scale of the experiment (ms), and this will influence the shape of the contact. However, the time scale of the simulation (ns) is much too short to allow for diffusion to occur. In order to compensate for this, the atomic mobility has been enhanced by annealing the tip to 1050 K for 270 ps. During the annealing, atoms migrate towards the lower substrate, and this leads to the formation of a neck with a structure which is significantly different from the original one.

After the annealing process, the tip is retracted. The temperature of the system is kept at 300 K by imposing corresponding fluctuating and frictional forces on the atoms in one layer at the bottom of the lower substrate. Figure 6.7(a) shows the evolution of the neck during stretching until it finally breaks. As a consequence, an island of material is left on the surface, just like in the experiment. From Fig. 6.7(a) it can also be seen that the central part of the neck can be viewed as a thin, metallic wire with a constriction. This can be utilized by replacing the “real” neck in (a) by the nanowire shown in (b). During stretch, the wire develops a constriction just like the neck, and the area-*versus*-stretch functions for the nanowires are found to be very similar to those for the “real” neck for constrictions smaller than about five atoms. For simplicity, nanowires are used in the following.

In order to make a statistical analysis of the “computer experiments” in analogy with the treatment of the experimental results in section 6.4,

---

<sup>9</sup>Performed by M. R. Sørensen.

<sup>10</sup>Performed by M. Brandbyge.

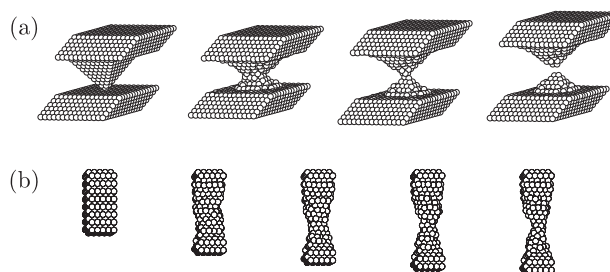


Figure 6.7: (a) Simulation of a tip indentation. Due to diffusion processes, a smooth connective neck is formed between tip and surface. The subsequent tip retraction leads to a neck evolution which closely resembles the stretch of a thin metallic wire. (b) Snapshots from a simulation of a stretching nanowire with a  $5 \times 5 \times 16$  structure along the  $[100]$  direction.

simulations of the stretch of 12 different Au wires have been performed. Starting configurations with 8 to 25 atoms in cross section and a length of 16 atomic layers arranged in one of three different structures ( $[100]$ ,  $[110]$  or  $[111]$  along the direction of the wire) with varying ratio of side lengths have been chosen. These simulations are used as the input to the conductance calculation discussed in the following.

Before a more elaborate version of the free-electron model presented in section 6.2 is introduced, it is worthwhile to consider whether such a model is appropriate for Au. First of all, it can be noted that, although bulk-Au has  $d$  bands, the transport properties are dominated by free-like carriers. This is reflected in the shape of the Fermi surface which is well described by the free electron sphere with some minor bulge-outs in the  $\langle 111 \rangle$  directions [36]. This shows that the ion potential for Au does not scatter the electrons at the Fermi surface considerably, and it is thus reasonable, for a semi-quantitative discussion of the possibilities for conductance quantization, to neglect scattering inside the nanowire due to single ions. In other words, it is reasonable to employ a free-electron picture.

While maintaining the “box-model” introduced in section 6.2, the adiabatic free-electron model will be elaborated on in two respects: Scattering at the boundary of the conductor will be included along with a better description of the electron potential. This is done as follows: For a given

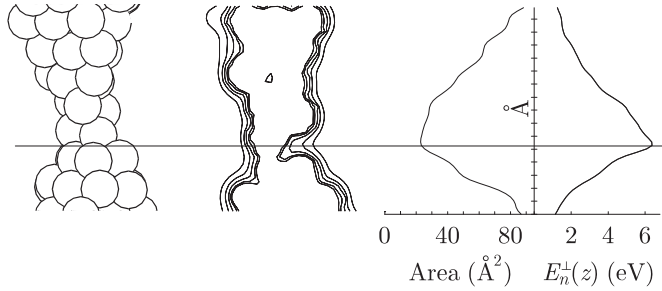


Figure 6.8: A simulated nanowire and the corresponding potential contour in a cross section. The last contour is the classical turning point. The derived area and potential  $((n_x, n_y) = (1, 1))$  are shown.

configuration of the wire, the one-electron potential is calculated within the local-density approximation. Then a “hard-wall” boundary is defined to be located at the classical turning point, that is, at the position where the one-electron potential is equal to the Fermi energy of Au ( $\approx 5.5$  eV). In this way, the free-electron cross-sectional area can be determined as a function of  $z$ . This procedure is illustrated in Fig. 6.8 which depicts an atomic configuration and the corresponding one-electron potential and the cross-sectional area along the wire. In analogy with Eq. (6.14), the effective potential is now defined as

$$E_n^\perp(z) = \frac{\hbar^2 \pi^2}{2m A(z)} \tilde{n}^2, \quad (6.15)$$

where

$$\tilde{n}^2 = \alpha(z) n_x^2 + \alpha(z)^{-1} n_y^2, \quad \alpha(z) = \frac{L_y(z)}{L_x(z)}, \quad (6.16)$$

and  $A(z)$  is the cross-sectional area of the wire. Both  $A(z)$  and  $\alpha(z)$  (the eccentricity) are extracted from the simulations. Enforcing a box geometry is, of course, a crude approximation to a real wire, and  $\alpha(z)$  is therefore not very well defined from the simulations. Consequently, the conductance calculation is carried out for both  $\alpha$ ,  $\alpha \pm 0.05$  and  $\alpha \pm 0.1$ , and all results are included in the final statistics. In this way, the dependence of the specific definition of  $\alpha$  is weakened.

Examples of the effective one-electron potentials, for specific constriction geometries obtained in the simulation, are plotted in Fig. 6.9. The potential-barrier landscape at a fixed point in time is shown in (a). Here it

is seen that  $E_{n_x, n_y}^\perp(z)$  for  $n_x, n_y > 1$  is not simply equal to a constant times  $E_{1,1}^\perp(z)$ . This is because  $\alpha$ , and thus  $\tilde{n}$ , depends on the position along the wire. In (b)  $E_{1,1}^\perp(z)$  is depicted at different stages of the stretching process. As the wire gets longer,  $E_{1,1}^\perp(z)$  increases, and the corresponding conduction mode is pinched off when the top of the barrier passes the

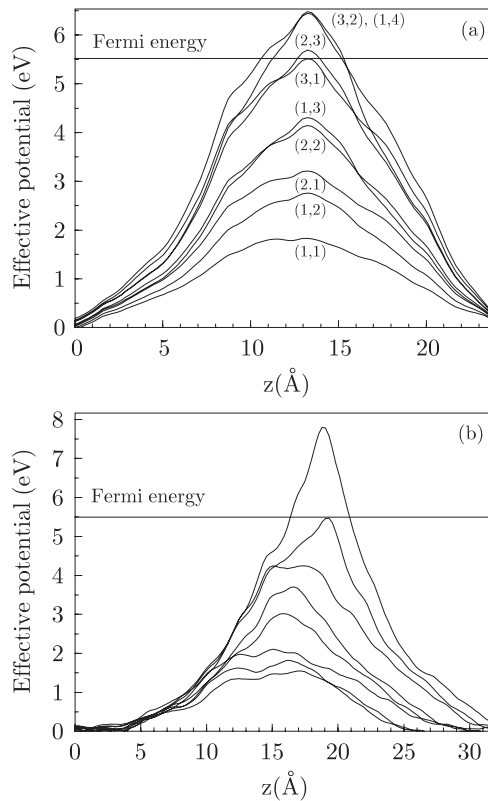


Figure 6.9: An example of potentials for different  $n_x$  and  $n_y$  along the wire is shown at a particular time during the stretch (a). Tunneling and reflectance above the barrier are present for  $(n_x, n_y) = (3, 2), (1, 4)$  and  $(n_x, n_y) = (3, 1), (2, 3)$  respectively, whereas the transmission is either very close to 1 or 0 for the rest. Successive  $n_x = n_y = 1$  potential-curves during stretch are shown in (b). The potential includes both the effect of changes in shape and the mean cross-sectional potential.

Fermi energy.

Up till now, the effect of a non-constant potential inside the wire has been neglected. When the wire is stretched, the mean potential in a cross section of the wire grows because there are fewer atoms present in the cross section, and the surface part of the potential therefore becomes relatively larger. This effect is included by adding to  $E_n^\perp(z)$  the change in the cross-sectional mean of the potential along the wire (zero chosen at the entrance/exit of the wire). Corrugations in this potential due to single Au ions are averaged out by taking a mean over several inter-atomic distances. The motivation for this is that scattering due to the single Au ion can be neglected, as argued previously. As a consequence of this additional contribution to the effective potential, the last channel will close somewhat earlier in the stretching process. Variations in the mean potential have been included in Fig. 6.9(b).

## Scattering

The relevance of the adiabatic approach is not at all obvious in this case, where the potential is corrugated on the scale of the Fermi wavelength. In the following, this point will be elaborated on to substantiate that an adiabatic approach in fact can be used.

From Fig. 6.9 it can be seen that the topmost part of the barrier is nearly a parabola in the last part of the stretching process where the conductance is less than about five quanta. Therefore, as a first estimate of the transmission, scattering from a single parabola-shaped potential is considered,

$$V(z) = V_{max} - \frac{1}{2}K(z - z_0)^2. \quad (6.17)$$

An *exact* expression for the transmission above and through a parabolic barrier was given in Eq. (2.10), which, in the tunneling regime, can be rewritten as

$$\mathcal{T} = \frac{1}{1 + \mathcal{T}_{WKB}^{-1}}, \quad (6.18)$$

where  $\mathcal{T}_{WKB}$  is given by Eq. (2.18). This holds for all  $V(z) > E_F$  in the parabola case. For the real potential, Eq. (6.18) provides a smooth *interpolation* between the regime where a parabola fit to the topmost part of the potential is a good estimate ( $V_{max} \approx E_F$ ), and the regime where  $\mathcal{T}_{WKB} \ll 1$ , i.e.,  $V_{max} \gg E_F$ . Strictly speaking, the WKB approximation is not valid here, as the potential is corrugated on a length scale com-

parable to the electronic wavelength<sup>11</sup> (see discussion on page 24). The argument for using Eq. (6.18) anyway goes as follows: For a parabolic barrier, Eq. (6.18) is exact, and it will therefore be a good approximation for a barrier that just cuts through the Fermi level. If the top of the barrier is well above  $E_F$ , then an expression, which takes deviations from a parabola into account, is needed, that is, if the barrier is wider than the parabola, then  $\mathcal{T}$  should be smaller and *vice versa*. Since  $\mathcal{T}_{WKB}$  is found by integrating over the barrier, this is precisely the result of Eq. (6.18) which certainly is not exact in this case, but it includes deviations from a parabola in a reasonable way.

For effective potentials with  $V_{max} < E_F$ , the transmission cannot be calculated directly. However, in the parabolic case, Eq. (2.10) is still valid, and it can be rewritten as

$$\mathcal{T} = \frac{1}{1 + [\exp(2\tilde{\epsilon})]^{-1}}, \text{ where } \tilde{\epsilon} = \frac{\pi}{\hbar} \sqrt{\frac{m}{K}} (E - V_{max}). \quad (6.19)$$

Note that  $\tilde{\epsilon} = -\epsilon$  is positive for  $V_{max} < E_F$ . In analogy with Eq. (6.18), where  $\exp(2\epsilon)$  was substituted by  $\mathcal{T}_{WKB}^{-1}$ , the term  $\exp(2\tilde{\epsilon})$  can now be substituted by  $\tilde{\mathcal{T}}_{WKB}^{-1}$ , where  $\tilde{\mathcal{T}}_{WKB}$  is equal to  $\mathcal{T}_{WKB}$  except that  $V_{max}$  and  $E_F$  have been interchanged. For  $V_{max} < E_F$ , the transmission in the parabolic case can thus be written as

$$\mathcal{T} = \frac{1}{1 + [\tilde{\mathcal{T}}_{WKB}^{-1}]^{-1}} = 1 - \frac{1}{1 + \tilde{\mathcal{T}}_{WKB}^{-1}}. \quad (6.20)$$

Like above, it is reasonable to use this expression also in the case of a general potential barrier. A similar approach was employed in the two-dimensional case by Glazman *et al.* to express the shape of a conductance step [37]. This can also be done in three dimensions, and for a rectangular cross section and a parabolic-shaped potential, the “smearing”  $\delta G$  of the conductance quantum step  $N$  is given by

$$\delta G(\gamma) = \frac{2e^2}{h} \left[ 1 + \exp \left( -\gamma 2\pi^2 \sqrt{\frac{2R}{A^{\frac{3}{2}} k_F^2}} \right) \right]^{-1}, \quad (6.21)$$

where

$$\gamma = \frac{k_F^2 A}{4\pi} - N \quad (6.22)$$

is a measure of the “distance” to a step, and  $R$  is the radius of curvature of the constriction. In the general case, Eqs. (6.18) and (6.20) lead to

<sup>11</sup>In fact, the width of the barrier is comparable to the electronic wavelength.

the same expression with an *effective* radius of curvature  $R_{eff}$  depending on where the potential is intersected by the Fermi level, and therefore it depends on the transverse mode under consideration. The width of the transition region between two conductance plateaus is seen to be given by

$$\Delta \sim \frac{1}{2\pi^2} \frac{A^{0.75} k_F}{\sqrt{2R_{eff}}} . \quad (6.23)$$

This result shows that the leading correction to the reflections *within each channel* is exponentially small in the “smoothness parameter”  $1/\Delta$ . In the two-dimensional case, it has been shown that the leading corrections to the *inter-channel* reflections are exponentially small in basically the same “smoothness parameter” as the within-channel reflections [38]. Intuitively, this can be understood since the intra-channel scattering is determined by the curvature of the top of the potential which depends on how rapidly  $L_{x,y}$  changes with  $z$ . This is also the factor that determines the mixing of channels, as discussed on page 103. It is therefore reasonable to estimate the total effect of scattering by the intra-channel part, as done above. From Eq. (6.23), it can thus be concluded that at high conductance levels, where  $A$  is large and  $R_{eff}$  small, the steps will be smeared out. However, as  $R_{eff}$  increases and  $A$  decreases during the stretching process, the conductance steps gets sharper. This is indeed what is observed experimentally [see Fig. 6.5(a)].

## Simulation Results

In Fig. 6.10 results from the simulation and subsequent conductance calculation are shown. The lower panel displays the conductance during neck elongation, and features quite similar to the experimental observations are readily identified. It is seen that the curves “slip through” the higher conductances until they develop plateaus during the last part of the stretch. These are seen mainly at  $G = 1, 2,$  and  $3$  quantum units. Often jumps from  $3$  directly to  $1$ , or only plateaus at  $1$  or  $1$  and  $2$ , are seen, like in the experiment. This is in the simulation controlled by the evolution of both the eccentricity and the area of the wire.

In Fig. 6.11, the theoretical histogram is shown. The conductance has been sampled at a fixed frequency during the stretching process. A comparison of the peak areas and widths obtained experimentally and theoretically is presented in Fig. 6.12. Here it is seen that the scaling of the area with  $G$  is in reasonable agreement with the experiment. The number of data points in the theoretical peak at  $G = 2 G_0$  is less than seen

in the experiment, whereas the peaks at three have identical areas. A very good agreement is found when comparing the widths of the peaks. The theoretical values are, within the uncertainties, equal to the widths found in the experimental histogram, except for  $G = G_0$ , where the theoretical peak is seen to be slightly sharper.

The difference in areas for the peaks at two quantum units may be explained as being a consequence of a lifted degeneracy. From Eqs. (6.15)

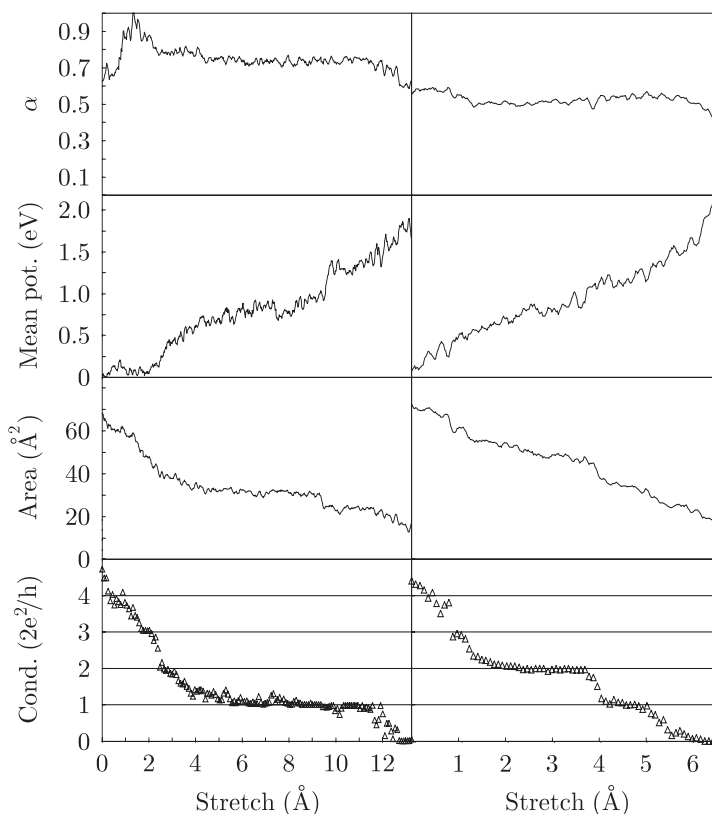


Figure 6.10: (a) Two “indentation curves” from the simulation series. The evolution of shape, change in mean potential (due to the increasing surface part of the potential with stretch) and the minimum area at the constriction are shown in the top most panels. It is seen how changes in these quantities influence the conductance displayed in the lower panel.

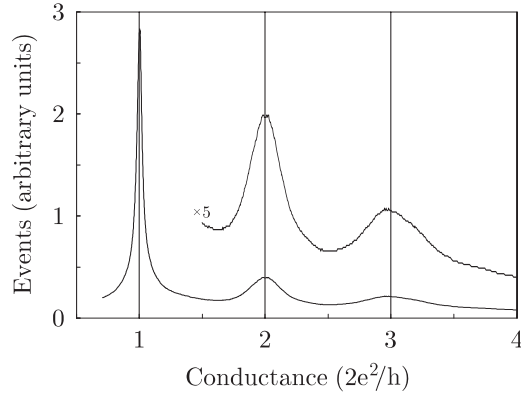


Figure 6.11: Theoretical histogram including conductance values from calculations with  $\alpha$ ,  $\alpha \pm 0.05$  and  $\alpha \pm 0.1$  for each simulation. The bin width to number of points sampled is chosen to be the same as in the experimental histogram.

and (6.16), it is seen that if the cross section of the nanowire is square-like ( $\alpha = 1$ ), then  $E_{1,2}^\perp = E_{2,1}^\perp$ , which means that the two effective barriers will cross the Fermi level simultaneously, causing a conductance jump from  $3 G_0$  to  $1 G_0$  [see Fig. 6.9(a)]. In this case, there will be no (or very little) contribution to the histogram peak at  $2 G_0$ , which will only incorporate data points from rectangular-like wires. Now, if there is a preference for such wires in the experiments, then this will result in an enhanced peak at  $2 G_0$  compared to the theoretical histogram, which is based on a set of “randomly” selected geometries. Experimental observations do indeed indicate that asymmetrical wires were favored<sup>12</sup>.

## Conclusion

In an adiabatic model, where the cross section of the nanowire varies slowly along the wire, the quantization of the electron motion perpendicular to the wire naturally leads to a quantization of the conductance in units of  $2e^2/h$ . This picture has in the present study been extended by in-

<sup>12</sup>It is often observed that the protrusions made by indentations on Au(110) are very elongated in the  $[1\bar{1}0]$  direction corresponding to  $\alpha = 3-10$ . Since a series of indentations results in similar shaped protrusions with the same characteristics, this is believed to be a consequence of the neck geometry, which, in turn, is determined by the tip geometry. It can be speculated that, after many indentations, such asymmetrical tips may form because of anisotropic diffusion (fastest in the  $[1\bar{1}0]$  direction) on Au(110).

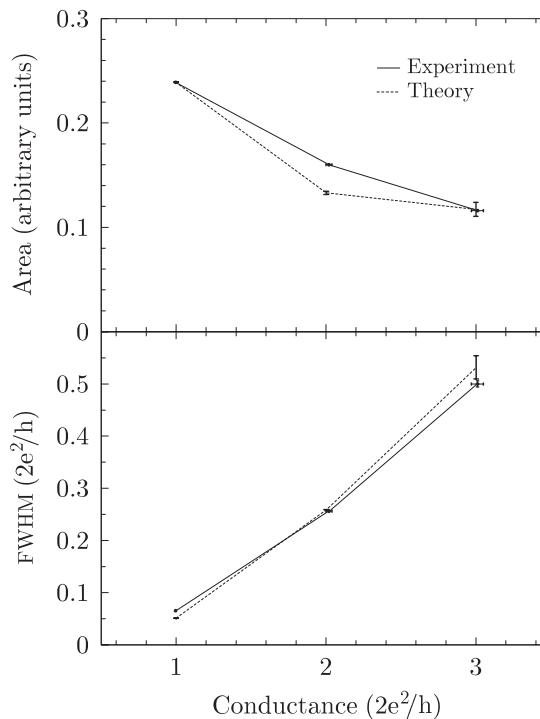


Figure 6.12: The area (a) and full width at half maximum (b) of the first three peaks in the experimental and theoretical histograms. The latter has been scaled so that the area of the peak at one conductance unit is the same as in the experimental histogram.

cluding the elastic scattering from the boundary of the constriction in a free-electron model. In this way, it has been shown that the experimentally observed conductance histogram can be accounted for theoretically, both with respect to the relative intensities of the observed peaks and to the increase of the widths for higher numbers of conductance quanta. This increase of the widths is argued to be determined by two factors, namely the cross-sectional area and the effective radius of curvature at the constriction.

The reason why scattering from the boundary does not completely destroy the quantization of the conductance is that the boundary is quite smooth — the typical effective radius of curvature is about five times the

atomic radius. However, it is also clear from the modeling that only a small increase in the scattering will cause the integer steps in the conductance curves to disappear. If, for instance, the system has scattering centers around the constriction with a typical length scale which is more like an atomic radius, then tunneling and reflection will be dominating, and the quantized conductance will vanish. In that case, the conductance is found always to reflect variations in the cross-sectional area of the constriction, and the conductance jumps are closely related to the mechanical instabilities observed in the simulations. This may still lead to conductance plateaus, but now there is no reason why they are at integer values of  $2e^2/h$ . This is the behavior expected for high conductances, where scattering is dominating, even for constrictions with effective radii of curvature equal to the ones found for the Au wires.

The close relation between conductance jumps and mechanical instabilities exists to a certain extent also in the quantized regime. Here, the conductance is still related to the cross-sectional area, albeit not in a smooth, monotonic way. Large changes in the area are bound to give changes in the conductance, as observed in Fig. 6.10. The main difference between the scattering-dominated and the quantized regimes is that in the latter case, the conductance plateaus are fixed at integer values of the quantum-conductance unit, whereas there is no reason why that should be the case in the other regime. It is therefore not surprising that both calculations [11,29] and experiments [23,28] show a correlation between mechanical instabilities and the conductance.

## 6.6 Further Discussion

With the ideal quantization in Au nanowires as a starting point, it can be questioned why Ni, Cu, and Pt behave differently. If the metals were free-electron-like to the same degree and the geometrical evolution of the necks were the same, then, in the ballistic regime, the overall conductance behavior would be the same for all the metals, as shown in section 6.2. From the experimental results, it is clear that this is certainly not the case. Here it is instructive to start out with a comparison of the noble metals Cu and Au which have very similar band structures [36]. Consequently, it is expected that a free-electron description can be applied, not only for Au but also for Cu. It is therefore natural to pay attention to the geometrical and structural properties of the necks when trying to resolve the remarkable differences between the corresponding histograms.

From Fig. 6.4(a) and 6.5(a), it is seen that the disruption of Cu necks is much more abrupt than observed for Au. At a conductance of  $8 G_0$ , the tip displacement needed to break the contact is typically a factor of three larger for Au than for Cu. Furthermore, one-quantum contacts of Cu spontaneously disrupt within  $\approx 1$  ms, even at 170 K, which also is in contrast to the findings for Au, where time sequences as long as  $\approx 30$  ms are observed without disruption (Fig. 6.6)<sup>13</sup>. This strongly indicates that thin Cu necks do not reach a metastable state in the same way as Au necks, and it is therefore plausible that Cu nanowires, from a structural point of view, are less perfect than their Au counterpart.

The Pt histograms shown in Fig. 6.2(b) and (c) provide further evidence for the importance of geometrical/structural effects. When only nanowires with a length longer than  $8 \text{ \AA}$  are taken into account, the characteristics of conductance quantization becomes apparent as peaks at 1 and  $2 G_0$ , i.e., the conductance of short Pt necks is not quantized and tends to smear out the peaks originating from long necks. The last constraint employed in Fig. 6.2(c) makes the peaks at integer conductance units become even more pronounced. As argued in footnote 4 on page 112, this constraint sorts out nanowires that loses their electrical contact before a mechanical disruption sets in, which is attributed to impurities in the neck. Albeit the experiments are carried out in UHV, impurities may be present in the neck. They can either be adsorbed from the gas phase or diffuse towards the junction from the surface or from the shaft of the tip. Here a major difference between the metals comes into play: Gold is the noblest of all metals [39], and the risk of impurity-related effects is therefore minimized<sup>14</sup>. However, for a large fraction of the Pt necks, there seemingly is an influence of impurities. Figure 6.4(a) indicate that this is also the case for Cu since, for at least three of the indentation curves shown, a conductance plateau at a fraction of  $G_0$  can be identified in the final part of the curves. The Ni histograms in Fig. 6.3 do not exhibit any pronounced effects of the constraints, and it can thus be concluded that either are

---

<sup>13</sup>These findings are at strong variance with the results found at RT by Muller *et al.* [25]. Here both Cu and Au contacts were found to degrade very slowly with time, that is, on a time scale of seconds. Their histograms also deviate from the ones showed in Fig. 6.4 and 6.5, as the Cu and Au histograms are essentially identical, and furthermore, the scaling of the peaks does not agree with the results of sections 6.4 and 6.5. For example, the area of the peak at  $G = G_0$  is smaller than the areas of the peaks at  $G = 2, 3,$  and  $4 G_0$ . It is not clear whether this discrepancy is caused by the different geometries employed (tip and flat *versus* tip and tip).

<sup>14</sup>This is also illustrated by the fact that it is possible to acquire STM images of an apparently clean Au surface after three days of exposure to UHV.

the histograms representative for an intrinsic conductance behavior in Ni necks, or another constraint has to be employed in order to remove possible “noise” that tends to smear out the underlying structure. However, other reasonable constraints are not easily found, and hence, the most likely explanation is that the histograms do indeed describe the general conductance behavior in Ni necks, which possibly is governed by geometrical and/or structural properties.

A change in temperature does not influence the Au histogram very much (Fig. 6.5), which is in agreement with the findings of Sirvent *et al.* [27]. However, at 390 K, the roles of the peaks at 1 and 2  $G_0$  have been interchanged, that is, the peak at 2  $G_0$  is now the larger. So, if the temperature is increased, the stability of one-quantum contacts is decreased. This may be explained as a consequence of thermal excitation since the neck configuration is metastable, that is, by breaking one or a few metallic bonds, a barrier is overcome, and a lower energy configuration is achieved during the relaxation of neck atoms towards the electrodes. For Cu, a remarkable effect of temperature is seen. At positive polarity, the peak at  $\approx 1 G_0$  increases for decreasing temperature, while the peak between 4 and 5  $G_0$  disappears. Although not as clear, there is a tendency to exactly the opposite behavior for negative polarity, i.e., the peak at 1  $G_0$  disappears for decreasing temperature, whereas a broad bump evolves in the range from 4 to 5  $G_0$ . The origin of these effects is not known at present, but it is very likely to be related to the polarity effects described in chapter 5.

Finally, it is noted that the discussion about conductance quantization *versus* conductance per area or per atom of the contact can turn out to be rather academic, especially because it has not really been defined rigorously what is meant by “quantization” in this case. At least two reasonable definitions can be put forth:

- The conductance is quantized whenever steps in the conductance of exactly one quantum  $= 2e^2/h$  are observed.
- The conductance is quantized whenever the electron transport is quantized into different transverse modes, that is, whenever the wave functions can be assigned transverse quantum numbers like  $n_x$  and  $n_y$  [40].

Arguments in favor of one or the other definition can be adduced: The first definition is very appealing from an experimental point of view since it facilitates an easy experimental test, in contrast to the latter definition. On the other hand, it is reasonable to talk about conductance quantization in situations where steps caused by opening or closing modes are

observed. In fact, it has recently been shown by Brandbyge *et al.* [41] that scattering centers in the constriction may cause a shift of the peaks in conductance histograms rather than a total smearing out. According to the latter definition, this is conductance quantization.

## 6.7 Summary

The present chapter has been concerned with electronic transport in atomic-sized metallic wires drawn between a tip and a single-crystalline surface. Deviations from macroscopic transport occur at two successively decreasing length scales. The ballistic regime is characterized by dimensions which are comparable to, or less than, the mean-free path of the conduction electrons. In this case, scattering will predominantly take place at the boundary of the conductor, and the transport properties then become independent of any material-dependent quantities, apart from the electron density. The quantized regime is reached by reducing the length scale to the order of an electronic wavelength, which, for ordinary metallic systems, is equivalent to atomic dimensions. If perfect quantization prevails, then the conductance will change abruptly in steps of the fundamental quantum unit  $2e^2/h$ . A theoretical background for these statements was given in section 6.2 which was followed by the experimental results in section 6.4. Here it was shown without ambiguity that the conductance of Au nanowires is quantized at the temperatures studied (170 K, RT, and 390 K). This is manifested as histogram peaks at one, two, three, and four conductance units. Long Pt necks ( $> 8 \text{ \AA}$ ), that do not show any sign of impurities, were also found to exhibit conductance quantization to some extent. In contrast, this was not the case for Ni and Cu. The Ni histograms, which did not depend on any of the constraints imposed, had a prominent broad peak at  $\approx 1.8 G_0$ , with a slow/fast decrease towards higher/lower conductances. For Cu the picture is rather messy as the histograms changed as a function of both temperature and polarity. In general, though, a peak around  $G = 3 G_0$  was observed along with a peak at 1.1–1.3  $G_0$ . A possible characteristic polarity-dependent shift of the peaks as a function of temperature, may be attributed to a thermo-voltage present in the UHV chamber.

In section 6.5, a theoretical modeling of the conductance in Au nanowires at RT was presented. Based on molecular-dynamics simulations of stretching Au nanowires, the conductance was calculated in a free-electron model which includes effects of scattering at the boundary of the conduc-

tor. By using various initial configurations of the nanowires, it was possible to mimic the experiments and the data analysis via histograms. In this way, the agreement was found to be very good, i.e., the decreasing areas and increasing widths of the histogram peaks for increasing conductances were reproduced to a high degree of accuracy. This model shows that the main factors determining the “washing-out” of peaks at higher conductances are the cross-sectional area and the effective radius of curvature of the constriction. The latter quantity was found to be about five times the atomic radius, which is the reason why scattering from the boundary is not strong enough to completely destroy the quantization.

Finally, it was discussed in section 6.6 what the origin of the differences between the metals were. By comparing Cu and Au, it was argued that the geometry and internal structure of the necks most probably were responsible. This conclusion is supported by the fact that for Pt, it is essential to exclude short necks when extracting histograms showing signs of conductance quantization. Yet another important factor for the quantization was found to be the presence of anomalously low conductance plateaus  $< 0.1 G_0$  which were interpreted as being a consequence of impurities in the junction. This may be an additional reason why Au apparently is the ideal case; since Au is the noblest of all metals, the risk of having impurities incorporated in the nanowire will be at a minimum for Au. In relation to the Ni histograms, it was concluded that they describe the general conductance behavior in Ni necks which possibly is governed by geometrical and/or structural properties.

## References

- [1] B. J. van Wees *et al.*, Phys. Rev. Lett. **60**, 848 (1988).
- [2] D. A. Wharam *et al.*, J. Phys. C **21**, L209 (1988).
- [3] C. W. J. Beenakker and H. van Houten, in *Solid State Physics*, edited by H. Ehrenreich and D. Turnbull (Academic Press, Inc, San Diego, 1991), Vol. 44, pp. 1–228.
- [4] G. Wexler, Proc. Phys. Soc. London **89**, 927 (1966).
- [5] Y. V. Sharvin, Zh. Exsp. Teor. Fiz. **48**, 984 (1965), [Sov. Phys. JETP **21**, 655 (1965)].
- [6] A. G. M. Jansen, A. P. Gelder, and P. Wyder, J. Phys. C **13**, 6073 (1980).
- [7] R. Landauer, IBM J. Res. Dev. **1**, 223 (1957).
- [8] M. Büttiker, Y. Imry, R. Landauer, and S. Pinhas, Phys. Rev. B **31**, 6207 (1985).

- [9] C. J. Muller, J. M. van Ruitenbeek, and L. J. de Jongh, *Phys. Rev. Lett.* **69**, 140 (1992).
- [10] N. Agraït, J. G. Rodrigo, and S. Vieira, *Phys. Rev. B* **47**, 12345 (1993).
- [11] T. N. Todorov and A. P. Sutton, *Phys. Rev. Lett.* **70**, 2138 (1993).
- [12] J. I. Pascual *et al.*, *Phys. Rev. Lett.* **71**, 1852 (1993).
- [13] J. M. Krans *et al.*, *Phys. Rev. B* **48**, 14721 (1993).
- [14] J. A. Torres, J. I. Pascual, and J. J. Sáenz, *Phys. Rev. B* **49**, 16581 (1994).
- [15] J. A. Torres and J. J. Sáenz, in *The Ultimate Limits of Fabrication and Measurement, NATO ASI Series E: Applied Sciences*, edited by J. K. Gimzewski, M. E. Welland, and C. Gerber (Kluwer Academic Publishers, Dordrecht, 1994).
- [16] J. M. Krans and J. van Ruitenbeek, *Phys. Rev. B* **50**, 17659 (1994).
- [17] V. V. Dremov, S. Y. Shapoval, and E. V. Sukhorukov, *Phys. Low-Dim. Struct.* **11/12**, 29 (1994).
- [18] V. V. Dremov and S. Y. Shapoval, *Pis'ma Zh. Éksp. Teor. Fiz.* **61**, 321 (1995), [*JETP Lett.* **61**, 336 (1995)].
- [19] J. M. Krans *et al.*, *Phys. Rev. Lett.* **74**, 2146 (1995).
- [20] J. M. Krans *et al.*, *Nature* **375**, 767 (1995).
- [21] J. I. Pascual *et al.*, *Science* **267**, 1793 (1995).
- [22] N. Agraït, J. G. Rodrigo, C. Sirvent, and S. Vieira, *Phys. Rev. B* **48**, 8499 (1993).
- [23] N. Agraït, G. Rubio, and S. Vieira, *Phys. Rev. Lett.* **74**, 3995 (1995).
- [24] A. M. Bratkovsky, A. P. Sutton, and T. N. Todorov, *Phys. Rev. B* **52**, 5036 (1995).
- [25] C. J. Muller, J. M. Krans, T. N. Todorov, and M. A. Reed, *Phys. Rev. B* **53**, 1022 (1996).
- [26] Z. Gai, Y. He, H. Yu, and W. S. Yang, *Phys. Rev. B* **53**, 1042 (1996).
- [27] C. Sirvent, J. G. Rodrigo, N. Agraït, and S. Vieira, *Physica B* **218**, 238 (1996).
- [28] G. Rubio, N. Agraït, and S. Vieira, *Phys. Rev. Lett.* **76**, 2302 (1996).
- [29] J. A. Torres and J. J. Sáenz, *Physica B* **218**, 234 (1996).
- [30] J. L. Costa-Krämer, N. García, P. García-Mochales, and P. A. Serena, *Surf. Sci.* **342**, L1144 (1995).
- [31] U. Landman, W. D. Luedtke, B. E. Salisbury, and R. L. Whetten, *Phys. Rev. Lett.* **77**, 1362 (1996).

- [32] K. Hansen, E. Lægsgaard, I. Stensgaard, and F. Besenbacher, to be published (unpublished).
- [33] É. N. Bogachek, A. N. Zagoskin, and I. O. Kulik, *Fiz. Nizk. Temp.* **16**, 1404 (1990), [*Sov. J. Low Temp. Phys.* **16**, 796 (1990)].
- [34] A. G. Scherbakov, E. N. Bogachek, and U. Landman, *Phys. Rev. B* **53**, 4054 (1996).
- [35] K. W. Jacobsen, J. K. Nørskov, and M. J. Puska, *Phys. Rev. B* **35**, 7423 (1987).
- [36] O. Jepsen, D. Glötzel, and A. R. Mackintosh, *Phys. Rev. B* **23**, 2684 (1981).
- [37] L. I. Glazman, G. B. Lesovik, D. E. Khmel'nitskii, and R. I. Shekhter, *Pis'ma Zh. Éksp. Teor. Fiz.* **48**, 218 (1988), [*JETP Lett.* **48**, 238 (1988)].
- [38] A. Yacoby and Y. Imry, *Phys. Rev. B* **41**, 5341 (1990).
- [39] B. Hammer and J. K. Nørskov, *Nature* **376**, 238 (1995).
- [40] K. W. Jacobsen and J. K. Nørskov, Definition of quantization, 1996, private communication.
- [41] M. Brandbyge, K. W. Jacobsen, and J. K. Nørskov, submitted to *Phys. Rev. B* (unpublished).



# Chapter 7

## Summary

The subject of the present thesis has been tunneling and contact phenomena taking place in the junction of a scanning tunneling microscope, which consists of two electrodes; a tip and a sample surface. Both electrical and mechanical properties of matter on the atomic scale are involved, and apart from being of interest to the STM community, new knowledge in the field may therefore also, on a longer time scale, have important implications for more practical-oriented fields like tribology and the development and production of VLSI circuits<sup>1</sup>.

Apart from a few standard surface-science techniques such as low energy electron diffraction (LEED) and Auger electron spectroscopy (AES), which have been used to characterize the single-crystalline surfaces [Ni(100), Ni(111), Cu(100), Pt(100), and Au(110)] during the initial cleaning processes carried out when they were introduced to the ultrahigh vacuum chamber, no experimental techniques other than STM have been employed. This is the natural consequence of the fact that the topics investigated from the very beginning were aimed directly at processes taking place in the STM. Furthermore, only very few techniques like other scanning probe methods or the break-junction technique manage to supplement the STM in a fraction of the experiments carried out. This truly demonstrates the unique possibilities of STM.

In the studies of the apparent barrier height (ABH), which is defined from the logarithmic derivative of the tunneling conductance with respect to gap width, it was found that the ABH stays constant all the way to the point where a contact is formed between tip and surface. Here it was

---

<sup>1</sup>VLSI: very large-scale integration.

shown that it is of crucial importance to include variations in the junction voltage as the gap resistance is changed; otherwise the erroneous conclusion of a collapsing barrier may result — a conclusion which indeed has been reported frequently in the literature. Furthermore, it was demonstrated that the collapse of the ABH, which has been predicted to occur for a static junction, is counteracted by a contribution caused by an accelerated decrease in gap width due to attractive tip-surface forces. The deduced values of the ABH were within 50–70% of the work function, i.e., no anomalously low values were found, and for both Cu and Au, it was observed to decrease with increasing temperature. In the experiments on atom-resolved, apparent barrier height, a variation of 15–25% perpendicular to the close-packed rows of the  $p(2 \times 1)$  reconstructed Au(100) was found for the three ways of measuring employed ( $z(I)$ ,  $z(V_b)$ , and ABH images). Again, no anomalously low values were found, however, ABH values deduced from measurements of  $z(V_b)$  were 30% lower than values based on measurements of  $z(I)$  and ABH images.

When the tunneling gap is diminished, a point contact may be formed in a process where considerable atomic rearrangements take place. For the temperatures investigated (170 K, RT, and 390 K), this phenomenon was found to take place on a millisecond time scale rather than the picosecond time scale expected for avalanche in adhesion. Prejumps that occur entirely within the tunneling regime were also observed along with contacts formed spontaneously in time. Based on these findings, it was concluded that the underlying mechanism is not avalanche in adhesion, rather, it agrees well with the diffusion-to-contact scenario proposed recently by Sørensen, Jacobsen, and Jónsson. A new polarity-dependent effect in contact formation was discovered for a Cu tip-sample system. When electrons are tunneling from the sample to the tip, a contact can develop at a larger gap width, compared to the opposite current direction. This effect was seen at 170 K, RT, and 390 K, and furthermore, at RT, it depended on the magnitude of the current. At RT, it was also observed that tunneling conductances as high as 5 quantum units could be reached without forming a contact. A reasonable explanation of these results could not be given, and it was concluded that further experiments are necessary to enlighten the matter.

After formation of a point contact, a connective neck between tip and sample can be formed upon subsequent withdrawal of the tip. As the tip is moved away from the surface, the neck will be stretched and thinned up to a point where the strain becomes too large and disruption inevitably occurs. At the last part of the stretch process, the cross section of the

wire consists of a single or a very few atoms. This should facilitate the observation of quantized conductance in metallic systems, despite the short metallic Fermi wavelength ( $\approx 5 \text{ \AA}$ ). For all four metals studied, it is indeed possible to pick out single conductance-*versus*-stretch curves which exhibit jumps in the conductance close to the fundamental quantum unit of  $2e^2/h$ . However, because of the intrinsic discreteness of the nanowire, a jump in the conductance will also be observed whenever the number of atoms in the smallest cross section is decreased as a consequence of a yielding event. Unfortunately, such conductance jumps will be of the same order of magnitude as the quantum unit. In order to provide good evidence for conductance quantization, a statistical analysis involving continuous conductance histograms has therefore been employed. Such an analysis demonstrated that the conductance is indeed quantized in Au necks. Long necks of Pt ( $> 8 \text{ \AA}$ ) also show signs of quantization, although not as perfect as for Au. For Ni and Cu, the picture is more blurred, and it was argued that the geometry and internal structure of the necks, rather than electronic effects, are most likely to be the reason. A theoretical model of the Au results was also presented, and very good agreement between experiment and theory was found. The model shows that the reason why conductance quantization can be observed in Au necks at RT is that the effective radius of curvature of the neck is about five times the atomic radius.



## Chapter 8

# Dansk resumé

Denne afhandling omhandler eksperimenter foretaget med et skannende tunnelerings mikroskop (STM), som i al væsentlighed består af to metal elektroder, hvoraf den ene er en meget skarp nål, mens den anden er en atomar flad enkeltkrystallisk overflade. Hvis nålen bringes meget tæt på overfladen (en milliontedel af en millimeter), så kan der trækkes en svag strøm (nanoampere) mellem nålen og overfladen ved pålægning af en lille spænding (millivolt), til trods for at elektroderne ikke rører hinanden. Dette fænomen er kvantemekanisk tunnelering, som ikke har nogen analogi i den klassiske fysik. I et STM udnyttes det, at tunneleringsstrømmen afhænger kraftigt af afstanden mellem elektroderne. Ved hjælp af en computer og et elektronisk styrekredsløb kan nålen flyttes hen over overfladen på en sådan måde, at strømmen holdes konstant, hvilket i en simpel fortolkning svarer til, at nålespidsen følger overfladens konturer i en fast afstand. Hvis denne bevægelse afbildes på en skærm, så opnåes et "billede" af overfladen. Det bemærkelsesværdige er, at forstørrelsesgraden kan være så stor som hundrede millioner, hvilket indebærer at de enkelte atomer i en overflade kan opløses.

På trods af at grundprincipperne i et STM er velkendte, så er der stadigvæk mange ubesvarede spørgsmål knyttet til de fysiske processer der forekommer i, og omkring, gabet mellem nålen og overfladen. Dette inkluderer både elektriske og mekaniske egenskaber på en atomar skala, og udover at være af stor betydning i forbindelse med udnyttelsen og forståelsen af STM, så kan ny viden muligvis have en indflydelse på andre grene af fysikken, som f.eks. tribologi (mekaniske egenskaber) og udviklingen af integrerede kredsløb (elektriske egenskaber).

Ud over nogle få standardteknikker til karakterisering af overfladernes beskaffenhed [lav energi elektron-diffraktion (LEED) og Auger elektron spektroskopi (AES)], så er STM den eneste teknik der har været anvendt. Dette skyldes, at målet med eksperimenterne hele tiden har været, at undersøge fysikken i selve mikroskopet, og at der kun eksisterer få teknikker, der tilnærmelsesvis kan supplere STM i denne sammenhæng, hvilket iøvrigt understreger de unikke egenskaber ved STM.

Det første emne der er berørt i denne afhandling, vedrører den såkaldte "tilsyneladende barriere højde" (TBH) i STM. Under specielle omstændigheder kan TBH sammenlignes med den gennemsnitlige højde af den potentialbarriere elektroner passerer i tunnelprocessen, omend nogen varsomhed er tilrådelig, idet denne sammenligning baserer sig på teoretiske tilnærmelser, som må anses for at være i grænsen af deres gyldighed. I modsætning til mange tidligere eksperimenter, hvor en aftagende TBH var observeret når gabet mellem nål og overflade reduceres, så blev det i de omtalte eksperimenter fundet, at TBH var konstant helt ind til det punkt, hvor kontaktdannelse mellem nål og overflade finder sted. I denne forbindelse blev det pointeret, at det er af afgørende betydning at kende den rigtige spænding mellem elektroderne. For det meste antages det, at spændingen er konstant, men i disse eksperimenter blev spændingen målt direkte, hvilket viste, at den aftager drastisk, når gabet reduceres. En sammenligning med en teoretisk behandling af emnet blev også foretaget. Teoretisk var det forudsagt, at TBH skulle aftage med aftagende elektrodeafstand. Overensstemmelse mellem denne teori og eksperimenterne kunne opnåes, hvis der blev taget højde for, at atomer i nålen og overfladen ikke sidder på statiske positioner, men tværtimod er påvirket af tiltrækkende kræfter fra den modstående elektrode. Derudover, blev der også præsenteret konsistente målinger af TBH med atomar opløsning på en guld (110) overflade, og der blev ikke i nogen af de tre anvendte målemetoder fundet en unormalt lav TBH, som det tidligere har været rapporteret.

Når elektrodeafstanden reduceres yderligere, så vil det føre til dannelsen af en punktkontakt. Denne proces finder sted i løbet af millisekunder og ikke picosekunder, som det er forventet i en adhæsions induceret kontaktdannelse. Det blev også observeret, at en kontakt kan dannes spontant uden at elektrodeafstanden ændres. Ud fra disse resultater blev det konkluderet at den underliggende mekanisme stemmer godt overens med nye teoretiske forudsigelser af en diffusion-til-kontakt proces. Under eksperimenterne blev der også observeret en ny effekt, som ikke har været omtalt tidligere i litteraturen. Elektrodeafstanden, ved hvilken kontaktdannelsen finder sted, afhænger af tunnelstrømmens retning for et system

bestående af en kobber nål og en kobber overflade. Desuden blev der ved stuetemperatur fundet en afhængighed af strømmens størrelse, mens dette ikke var tilfældet ved  $+120^{\circ}\text{C}$  og  $-100^{\circ}\text{C}$ . En nærmere forklaring på fænomenet kunne ikke gives på nuværende tidspunkt, og det blev konkluderet at yderligere eksperimenter var nødvendige.

Når nål og overflade er i kontakt, så kan der dannes en metaltråd ved tilbagetrækning af nålen. Denne tråd vil blive tyndere og tyndere, efterhånden som den bliver forlænget, og i den sidste del af strækningen inden tråden uundgåeligt knækker, da har den et tværsnit, der svarer til ganske få atomer. Under disse omstændigheder skulle det være muligt at observere kvantiseret konduktans. Det er imidlertid ikke indlysende, hvorledes dette påvises, idet flytninger af enkelte atomer i tråden vil give anledning til spring i konduktans, som er af samme størrelse som den fundamentale kvanteenhed. Ved at anvende en statistisk analyse af konduktansen i mange tråde blev det påvist at kvantisering kan observeres i guldtråde, der har en størrelse sammenlignelig med atomare afstande. Tilsvarende resultater blev fundet i lange tråde ( $> 8 \text{ \AA}$ ) af platin, omend effekten ikke er så udtalt som for guld. For tråde bestående af nikkel og kobber er resultaterne mindre entydige, og det blev foreslået, at geometrien og strukturen af tråden var af afgørende betydning for disse resultater. En teoretisk model for tråde af guld blev også præsenteret, og her blev fundet god overensstemmelse mellem teori og eksperiment. Ifølge modellen, så er det af afgørende betydning for kvantiseringen, at trådene har en krumningsradius, som er fem gange større end en atomar radius.



# Appendix A

## Electronic Details

### A.1 Preamplifiers

In Fig. A.1 the preamplifier setup is shown. It consists of two amplifiers (one for  $I$  and one for  $V_j$ ) and a correction circuit. The current amplifier is a special design with two amplification stages coupled in cascade. Each step has a gain of 31.6 giving a total gain of  $A = 1000$ . The feedback resistor  $R_{fb}$  determines the input impedance  $R_{in} = R_{fb}/A$  as well as the amplification and the range of the preamplifier. In the example shown in Fig. A.1 the output is 0.1 V/nA (50 nA range), that is,  $R_{fb} = 100 \text{ M}\Omega$ , and thus  $R_{in} = 100 \text{ k}\Omega$  (116 k $\Omega$  measured). By changing  $R_{fb}$  to 10 M $\Omega$  the output becomes 0.01 V/nA (500 nA range) and  $R_{in}$  is lowered to 10 k $\Omega$  (11 k $\Omega$  measured).

The effect of having two amplification steps, each with a low gain of  $\approx 30$ , is a flat frequency response up to 20 kHz, i.e., below 20 kHz the gain and  $R_{in}$  are independent of frequency. Here it should also be mentioned that the stray capacitance of  $\approx 1 \text{ pF}$ , can be corrected for by adjusting  $R_1$  in the low-pass filter.

As a voltage amplifier is used a standard instrumentation amplifier with a high input impedance ( $> 1 \text{ T}\Omega$ ). The bandwidth is limited to 2 kHz resulting in a noise level of only 3  $\mu\text{V}$ . The correction circuit compensates for a capacitance between tip and sample when  $V_b$  is ramped as, for example, is done in a measurement of  $z(V_b)$ . It consists of a negative unity amplifier with adjustable gain (adjusted by  $R_2$ ) and a 1 pF capacitor. The circuit is tuned to the capacitance in the STM by adjusting to minimum output on the current amplifier when a 5 kHz signal is used as  $V_b$ .

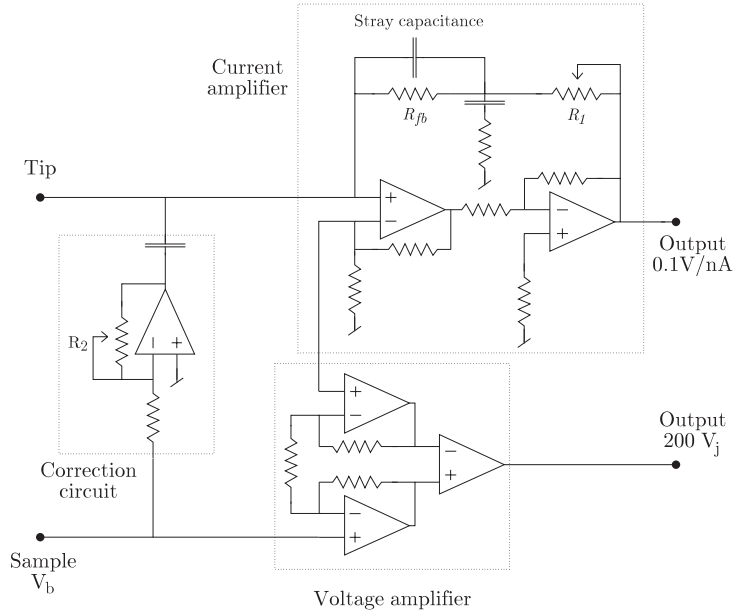


Figure A.1: Sketch of the current and voltage preamplifiers along with a correction circuit for tip-sample capacitances. A brief description can be found in the text while further details will appear in publication VII.

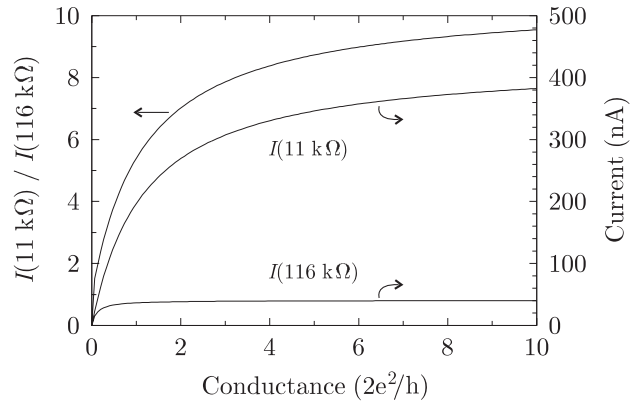


Figure A.2: Calculated currents for input resistances of 11 k $\Omega$  and 116 k $\Omega$  at a bias voltage of 4.7 mV (typical value in indentation experiments). The ratio of the two currents is also shown.

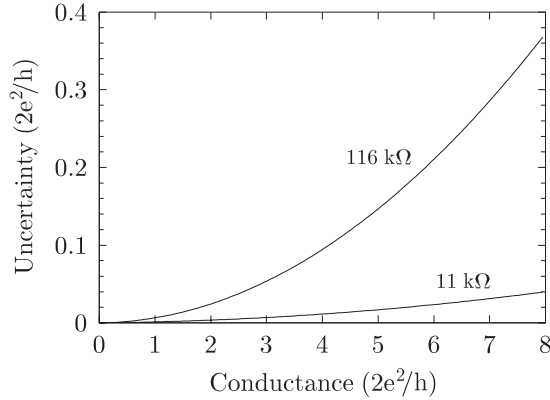


Figure A.3: Uncertainty in conductance measurement for two values of  $R_{in}$  calculated for  $V_j = 4.7$  mV.

## A.2 Current and Input Impedance

By adjusting the input resistance  $R_{in}$  of the current preamplifier, the maximum current flowing in the circuit can be controlled according to  $I_{max} = V_b/R_{in}$ . The real current  $I$  depends on the conductance of the junction  $G$ ,

$$I = \frac{V_b}{R_{in} + 1/G}. \quad (\text{A.1})$$

In Fig. A.2  $I$  is plotted as a function of  $G$  ( $V_b = 4.7$  mV) for the two input resistances used in the experiments, 11 k $\Omega$  and 116 k $\Omega$ . Also shown is the ratio of the curves. When the conductance in the junction attains a value of one quantum unit,  $I(11 \text{ k}\Omega)$  and  $I(116 \text{ k}\Omega)$  differs with a factor of 5.4.

## A.3 Precision of Conductance Measurement

The precision of the conductance measurement is determined by the preamplifier input resistance  $R_{in}$  and the critical noise level of  $3 \mu\text{V}$  in  $V_j$ . In Fig. A.3 is shown how the precision is increased by roughly an order of magnitude when the current limit is increased by decreasing  $R_{in}$  from 116 k $\Omega$  to 11 k $\Omega$ . In apparent barrier height measurements a value of  $R_{in} = 116 \text{ k}\Omega$  is preferred due to the smaller noise level in  $I$  (25 pA as opposed to 75 pA). This is of importance in the tunneling regime.

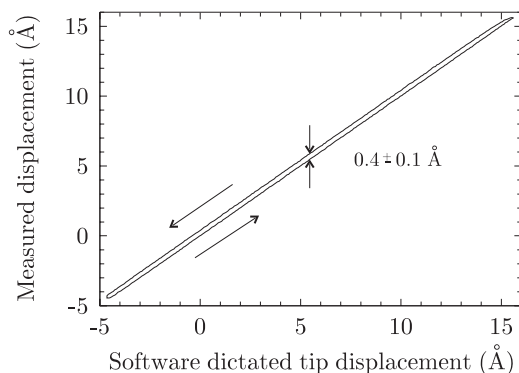


Figure A.4: Displacement corresponding to the piezo voltage measured during indentation, as a function of the software dictated displacement. The hysteresis in curve is caused by a delay in the electronics. It amounts to  $0.4 \text{ \AA}$  at the present indentation speed ( $295 \text{ \AA/s}$ ).

## A.4 Piezo Voltage Delay

When the STM controlling software directs the electronics to move the tip, the  $z$  piezo voltage  $V_z$  does not change instantaneously. This is revealed by measuring  $V_z$  during an indentation. In Fig. A.4 are the results from such a measurement shown. Here,  $V_z$  has been converted to a displacement according to the distance calibration. At an indentation speed of  $295 \text{ \AA/s}$ , the electronic time lag gives rise to a hysteresis of  $0.4 \pm 0.1 \text{ \AA}$ . In addition, hysteresis in the piezo-electric ceramics may cause a similar effect.

## A.5 Time Calibration

During data acquisition it is often important to have a relative measure of time. For example, the speed of indentations is determined by the sampling rate as the indentation displacement is preset, and the number of data points is fixed. Even though most computer systems have a built-in clock, it may not be updated as fast as desired, i.e., the smallest time period measurable is too long. Alternatively, a pure software “clock” can be used which is based on a knowledge of the time it takes to execute a certain sequence of commands (typically loops). However, this method has the obvious disadvantage that the time of execution depends on the speed

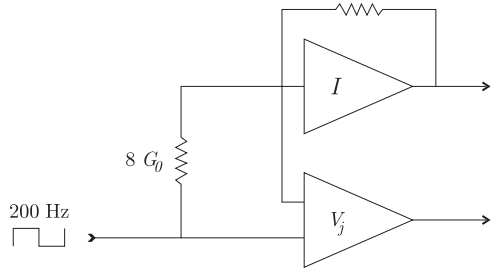


Figure A.5: Sketch of the setup used in the time-calibration measurement. The tunnel junction is substituted by a resistance of  $1.63 \text{ k}\Omega$  ( $\sim 8$  quantum units of conductance), and the bias voltage is a square 200 Hz signal with an amplitude of 5 mV.

of the controlling computer. In the present data-acquisition system, this is dealt with in a very elegant way — every time the software is started up, the speed of the computer is measured relative to a fixed standard. To test the accuracy of this method and to make an absolute time calibration, a simulated input was introduced into the input terminals of the preamplifiers, as sketched in Fig. A.5. A resistance corresponding to a conductance of eight quantum units ( $\sim 1.63 \text{ k}\Omega$ ) was substituted for the tunnel junction, and a 200 Hz square signal with an amplitude of 5 mV

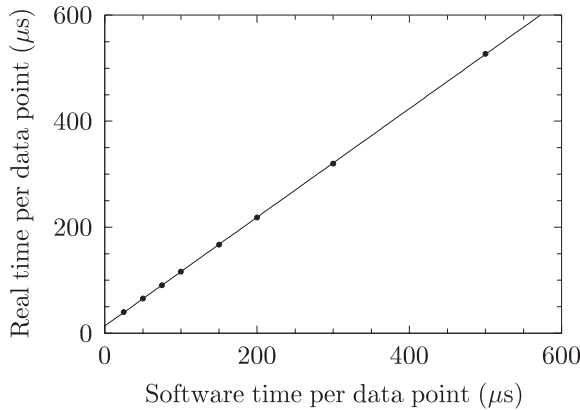


Figure A.6: Calibration curve relating software time to real time. The data have been fitted to a straight line given by  $y = 1.02x + 13.6$ .

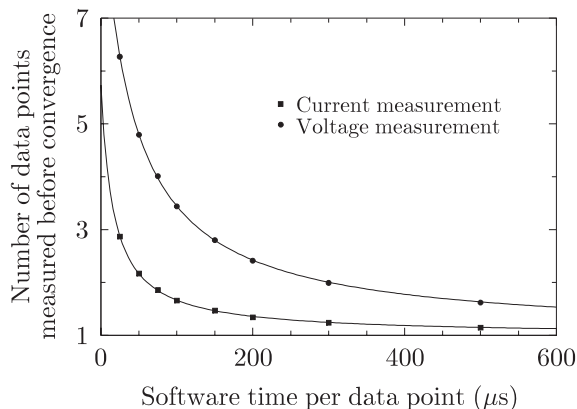


Figure A.7: Number of data points measured, after a change of polarity, before convergence to within 5% occurs.

was used as bias voltage.

With the setup shown in Fig. A.5, “indentation” measurements were made for different software time settings. From the known frequency of 200 Hz and the mean number of data points between a polarity change, the relationship between real time and software time could be found. The result is shown in Fig. A.6, where data points have been fitted to a straight line given by  $y = 1.02x + 13.6$ . It is seen that the software timing works remarkably well. All time-dependent data presented in the present thesis have been calibrated according to Fig. A.6.

Based on the same data set, it is also possible to test how fast the electronics can respond to a change in  $I$  and  $V_b$ . The ultimate change, a switch of polarity, is expected to result in an upper limit on the electronic response time. In Fig. A.7,  $n_c(\Delta t)$ , the resulting number of data points measured before convergence (to within 5%), is plotted as a function of the software time per data point ( $\Delta t$ ). The voltage measurement is seen to be a factor of 1.4 to 2.2 slower than the current measurement, however, as long as the time per data point is 200  $\mu\text{s}$  or more (in indentations, it is usually set to 250  $\mu\text{s}$ ), convergence occurs within two data points. It is expected that real time rather than the number of points measured is crucial for the response time, i.e., if  $\Delta t$  is doubled, then<sup>1</sup>  $n_c(\Delta t) - 1$  will be reduced by a

<sup>1</sup>Convergence cannot be detected without at least one data point ( $n_c(\Delta t) \geq 1$ ), which is the reason for the subtraction of 1.

factor of two or *vice versa*, that is,  $n_c(\Delta t) - 1 \propto (\Delta t)^{-1}$ . Consequently, the data have been fitted to functions of the form  $y = 1 + \alpha/(x + \beta)$ , which gives a very good agreement.



# Appendix B

## Data Analysis

### B.1 Thermo-voltages and Tip Resistances

Even though the conductance measurement has been calibrated against known resistances there are two further complications in the experiments. Due to temperature gradients in the UHV chamber, the voltage is slightly offset by a thermo-voltage  $V_{th}$ . Until recently, it was believed that  $V_{th}$  was located in the junction itself since the tip probably stays at RT when the sample is cooled/heated. However, the presence of a thermo-voltage in a Cu tip-sample system (cf. Fig. 6.4 on page 115) indicates that this is not the case. A measurement of  $V_{th}$  was carried out by measuring the voltage on the tunnel current wire with respect to ground when the tip was indented  $\approx 200 \text{ \AA}$  into the sample. This measurement, which was carried out at RT, resulted in a value of  $11.5 \pm 1.0 \text{ \mu V}$ . However, since such measurements most probably destroys the tip, they are not recommended. Instead, the sign on  $V_b^i$  can be changed regularly throughout the indentation experiments. This will give rise to two conductance histograms which are phase shifted in opposite directions, as the sign on  $V_{th}$  only depends on temperature. Consequently,  $V_{th}$  can be determined by correcting on  $V_b^i$  off-line until the histograms have been phase shifted back together. Here it is implicitly assumed that the two histograms are equal, apart from the phase shift. In case of Au, this is not a matter of concern as the polarity specific histograms indeed are equal. However, the procedure would be more questionable for the Cu histograms shown in Fig. 6.4, although they also indicate the presence of  $V_{th}$ .

A more difficult problem is the internal resistances in the electrodes

connecting the ballistic system to the macroscopic world. In the macroscopic part of the electrodes the resistance is negligible, however, because of the small dimensions close to the ballistic system under investigation, the total resistance  $R_{tip}$  can be of importance. This serial resistance depends strongly the geometry and structure of the electrodes, and in STM experiments it can readily attain any value from less than one ohm to several hundreds of ohms depending on the specific shape of the tip apex. How to evaluate this quantity is not obvious. However, an alternative point of view can be adopted: With the assumption of quantization,  $R_{tip}$  can be found by fitting the histogram peak at  $1 G_0$  to exactly one quantum unit. If the resulting value of  $R_{tip}$  is plausible and the peaks at two, three, and four times  $G_0$  are shifted towards their respective integer values, then the procedure seems to be reasonable. This approach always gives a resistance value lying in the range 150–250  $\Omega$ . It should be noted that the peak positions are not very sensitive to the exact value of  $R_{tip}$ , which is also reflected in the uncertainties stated in Table 6.1. These are a result of the uncertainty on  $R_{tip}$ , which is estimated to be 50  $\Omega$ .

The above described procedure has been used for the Au histograms in chapter 6. Since the value of  $R_{tip}$  always is found to lie close to 200  $\Omega$ , the histograms for Ni, Cu, and Pt have been corrected accordingly.

## B.2 Conductance Calibration

The conductance measurement is calibrated for each experiment carried out. It is important to note that this takes place immediately before a set of measurements is initiated. This allows the electronics to stabilize during the tip-preparation treatment<sup>1</sup> ( $\approx 1$  hour). Calibration resistances of 1–8  $G_0$  are connected to the preamplifiers as virtual junctions. For each resistance the conductance is measured in eight “indentations” for each polarity. An example of the resulting mean values is shown in Fig. B.1. It has become standard to double-check the calibration by performing yet another calibration at the end of each experiment. This will reveal any possible drift during the experiment. Data from such a final calibration are also plotted in Fig. B.1 and the data sets, which were measured at a time interval of two hours, are seen to lie on top of each other to a good accuracy. The corresponding calibration curve is very close to being linear:  $G(\text{real}) = 1.042 G(\text{measured})$ . A conversion factor of 1.041–1.042 is nearly

---

<sup>1</sup>Just after turning on the electronics, a noticeable drift in the measurements is observed.

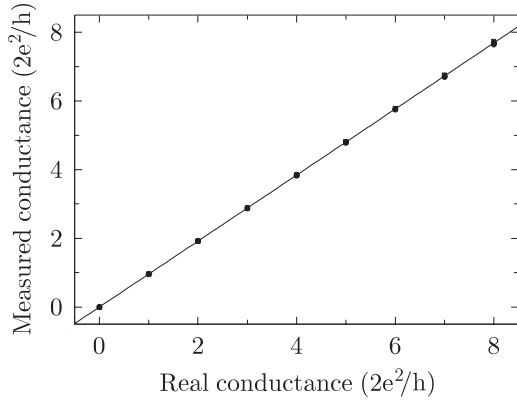


Figure B.1: Calibration data from before *and* after a series of measurements ( $\sim 2$  hours). Both polarities are included. See test for further details!

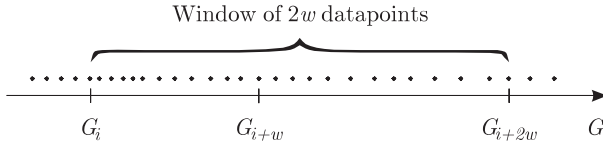


Figure B.2: The histogram value at a conductance  $G_{i+w}$  is calculated from the density of data points in a window of  $2w$  data points.

always found.

### B.3 Continuous Histograms

A conductance histogram is made in the following way: First, all the measured values of  $G$  are sorted in increasing order (see Fig. B.2). Then the histogram value at a certain measured  $G_{i+w}$  is calculated as

$$H(G_{i+w}) = \frac{\rho_{i+w}}{N}, \text{ where } \rho_{i+w} = \frac{2w}{G_{i+2w} - G_i} \quad (\text{B.1})$$

is the density in a window of  $2w$  data points, and  $N$  is the total number of data points in the histogram. The normalization factor of  $1/N$  ensures that the integrated histogram is  $\approx 1$ .